

Northumbria Research Link

Citation: Dai, Bo, Ma, Yong, Dong, Feng, Yu, Jia, Ma, Mingliang, Thabet, Hamdy Khamees, El-Bahy, Salah M., Ibrahim, Mohamed M., Huang, Mina, Seok, Ilwoo, Roymahapatra, Gourisankar, Naik, Nithesh, Xu, Bin, Ding, Jianxu and Li, Tingxi (2022) Overview of MXene and conducting polymer matrix composites for electromagnetic wave absorption. *Advanced Composites and Hybrid Materials*, 704 (754). pp. 5-2. ISSN 2522-0128

Published by: Springer

URL: <https://doi.org/10.1007/s42114-022-00510-6> <<https://doi.org/10.1007/s42114-022-00510-6>>

This version was downloaded from Northumbria Research Link: <https://nrl.northumbria.ac.uk/id/eprint/49468/>

Northumbria University has developed Northumbria Research Link (NRL) to enable users to access the University's research output. Copyright © and moral rights for items on NRL are retained by the individual author(s) and/or other copyright owners. Single copies of full items can be reproduced, displayed or performed, and given to third parties in any format or medium for personal research or study, educational, or not-for-profit purposes without prior permission or charge, provided the authors, title and full bibliographic details are given, as well as a hyperlink and/or URL to the original metadata page. The content must not be changed in any way. Full items must not be sold commercially in any format or medium without formal permission of the copyright holder. The full policy is available online: <http://nrl.northumbria.ac.uk/policies.html>

This document may differ from the final, published version of the research and has been made available online in accordance with publisher policies. To read and/or cite from the published version of the research, please visit the publisher's website (a subscription may be required.)

Overview of MXene and conducting polymer matrix composites for electromagnetic wave absorption

Bo Dai¹, Yong Ma^{1,*}, Hamdy Khamees Thabet^{2,*}, Feng Dong¹, Salah M. El-Bahy³, Jia Yu¹, Mohamed M. Ibrahim⁴, Mingliang Ma⁵, Mina Huang⁶, Ilwoo Seok⁷, Gourisankar Roymahapatra⁸, Nithesh Naik^{9,*}, Ben Bin Xu¹⁰, Jianxu Ding¹, Tingxi Li^{1,*}

¹ School of Material Science and Engineering, Shandong University of Science and Technology, Qingdao 266590, P. R. China

²Department of Chemistry, Faculty of Arts and Science, Northern Border University, Rafha, 91911, PO 840, Saudi Arabia (hamdy.salem@nbu.edu.sa)

³Department of Chemistry, Turabah University College, Taif University, P.O.Box 11099, Taif 21944, Saudi Arabia (s.elbahy@tu.edu.sa)

⁴Department of Chemistry, College of Science, Taif University, P.O. Box 11099, Taif 21944, Saudi Arabia. (Ibrahim@tu.edu.sa)

⁵ School of Civil Engineering, Qingdao University of Technology, Qingdao, 266033, PR China

⁶ College of Materials Science and Engineering, Taiyuan University of Science and Technology, Taiyuan, 030024, China

⁷ Mechanical Engineering, Arkansas State University, Jonesboro, Arkansas, 72401, USA

⁸ School of Applied Science and Humanities, Haldia Institute of Technology, Haldia 721657, India

⁹ Department of Mechanical and Industrial Engineering, Manipal Institute of Technology, Manipal Academy of Higher Education, Manipal-576104, Karnataka, India

¹⁰ Department of Mechanical and Construction Engineering, Faculty of Engineering and Environment, Northumbria University, Newcastle upon Tyne, NE1 8ST, UK

*Correspondence author: mayong@sdust.edu.cn (Y. Ma); nithesh.naik@manipal.edu (N. Naik);

hamdy.salem@nbu.edu.sa (H.K. Thabet); litx@sdust.edu.cn (T. Li)

Abstract

With the rapidly developing wireless communication technology, electromagnetic pollution problems have become more prominent. Electromagnetic pollution has caused great harm to wireless equipment, precision instruments, military safety, etc., which urgently requires the development of lightweight, high-efficiency, broadband electromagnetic waves (EMW) absorbing materials. MXene is an emerging two-dimensional (2D) material with the advantages of lamellar structure, excellent conductivity, and abundant surface groups. At the same time, conducting polymers (CPs) have excellent performance in terms of conductivity, surface activity, quality, and electromagnetic loss, making them have excellent potential in EMW absorbing direction. This article examines the preparation, structure, and performance of MXene and CPs-based radar absorbing materials (RAM). A comprehensive summary and objective analysis of the nowadays study progress on the EMW absorbing performances of MXene and CPs, and a comprehension of the absorbing mechanism are reviewed. Finally, the research direction of absorbing materials has been prospected.

Keywords: Electromagnetic wave; MXene; Conducting polymer; Composite; Absorption.

1. Introduction

The rapid blossom of technology and science has brought significant changes to our way of life in modern life [1, 2]. The use of electromagnetic waves (EMW) can be said to be the foundation of the information revolution. In particular, detection and communication technologies enable widely applications of industrial equipment and electronic devices [3, 4]. Mobile 4G, 5G communications, home wifi routers, computers, etc., are all transmitting data using EMW as the carrier. While improving the quality of life, they can also bring many problems [5-7]. There are many electronic devices and the intricate processes of information generation, transmission, and reception, which make us go to have to exist in a complex electromagnetic radiation environment all the time [8]. Electromagnetic radiation will interfere with adjacent circuits or sophisticated electronic equipment. Numerous works of literature, publications, etc., all suggest that electromagnetic radiation may cause health problems such as cancer, headache, depression, fatigue, etc. [9, 10]. Whether it is a developer who earns technological dividends or an individual who makes use of technological convenience while lamenting technological development, they deliberately or unintentionally ignore this chronic health problem [9]. On the other hand, in order to avoid radar detection and increase the chance of survival on the battlefield in the military field, there is imperative to develop stealth materials [11, 12]. The development and application of absorbing materials are essential measures to realize the stealth of weapon systems, which are the key to stealth technology [13].

It is well known that EMW can be eliminated via eliminating the energy of electric or

magnetic fields. The earliest electromagnetic protection is to use metals with high conductivity, such as Fe, Co [14], Ni [15], Fe₃O₄ [16, 17], and others [18-21]. They are used to reflect EMW to make electromagnetic shielding materials [22-25]. However, due to their large size, inflexible operation, lack of corrosion resistance, and the fact that the EMW they reflect can be captured by radar. Therefore, metallic materials are not suitable for use in areas such as the military with these inherent these limitations.

Non-metallic conductive materials, such as C [26-28], CNTs [22, 29], graphene [30-32] and others [33], have achieved excellent absorption performance in the field of EMW absorption compared to metallic materials due to their light mass and high electric loss. However, the new conductive materials MXene show greater absorption advantages. They have abundant surface functional groups and more stable spatial structures, in addition to having a large specific surface area, high conductivity, and light weight similar to graphene [34]. The efficient capture capability of MXene for incident EMW is mainly due to the high specific surface area, efficient dielectric loss from multiple polarization mechanism, and enhanced interfacial loss from unique two-dimensional (2D) nanostructures. MXene is an burgeoning 2D material with a graphene-like structure [35]. MXenes is a family of 2D transition metal carbides/nitrides/carbonitrides [36]. In 2011, Naguib et al. [37] first synthesized Ti₃C₂T_x MXene. They normally possess a formula M_{n+1}AX_n, in which M denotes as a transition metal (such as Ti, V, Mo, etc.), A is on behalf of IIIA or IVA element (such as Al, Si, etc.), and X stands for N or C (n=1, 2, or 3). The A layer is etched away by technical means to obtain M_{n+1}X_nT_x with ultra-high specific surface area, as well as T_x is

surface terminations (-F, -O, or -OH, etc.) [38-40]. In order to intuitively express the source of the material and the graphene-like sheet structure, it is named MXene. Up to now, there are currently a variety of MXene materials, such as $Ti_3C_2T_x$ [41], Ti_2CT_x [42], $Ti_4N_3T_x$ [43], Nb_2CT_x [44], etc. as shown in Fig. 1a as the MXene family. MXene have hydrophilicity and conductivity from the structural point of view, and part of MXene also has a certain degree of magnetism, relying on different "M" [35]. This unique combination of properties can be further adjusted by controlling their composition and surface groups. So that theoretical and experimental research on its properties and potential applications is increasing [45, 46]. MXene has good electromagnetic absorbing performance, mainly due to its good interlayer electronic coupling and excellent conductivity. This means that MXene, as a new 2D material, can replace graphene for more effective electromagnetic protection [47, 48].

At as well, carbon materials are not as well processed and modified as conducting polymers (CPs), specifically in terms of conductivity regulation and defect control. CPs, as the most special class of polymer materials, exhibit excellent potential for electromagnetic wave absorption (EMA), including polyaniline (PANI) [49, 50], polypyrrole (PPy) [51, 52], polythiophene (PTh) etc.. The π -conjugated chains of CPs endow a delocalized electronic structure resulting in extraordinary electronic performances, for instance, low ionization potential and energy optical transitions, good conductivity, as well as high electron affinity [53-55]. The CPs' conductivity can be improved by doping. Therefore, many works have used CPs as electromagnetic interference (EMI) shielding materials. Nonetheless, it has also been found that most of their shielding effect comes from EMW

absorption, not just reflection [56]. Therefore, CPs are potential in the direction of EMW absorption, through the modulation of structure and conductivity. In addition, CPs have unique advantages such as corrosion resistance, adjustable structure, low density, and easy preparation [57, 58]. This effective absorption performance and other advantages have stimulated research of CPs and their composites.

MXene and CPs have excellent conductivity as EMA conditions. Since MXene has abundant surface functional groups, such as -F, -O, -OH, etc., it is very easy to form dipoles with -N, -H of CPs [59]. The composites of the two materials form richer dipoles and multi-interfaces and more complex conducting network. Polarization relaxation is more meaningful for the absorption of EMW in the radar band, compared to the conductivity loss. The research and development of lightweight, stable, efficient, and broadband absorbing materials is the current research hotspot. MXene and CPs suffer from single loss, narrow effective absorption bandwidth (EAB), and thick matching thickness like conventional conductive materials. Compounding with magnetic materials is an effective approach, by introducing magnetic losses and increasing impedance matching [60]. Fig. 1c summarizes the amount of EMA literature on MXene, PPy, PANI and their composites in the last decade. It can be observed from the figure that more and more CPs and MXene are being used for EMA studies. Fig. 1b summarizes the percentage of MXene, CPs and MXene/CPs based RAM in the last 10 years. Although the number of literature reports of composite materials of MXene and CPs applied in the direction of EMA is relatively small, there is still a future research initiative [61]. So far, no summary review based on the combination of these two materials has

been found. This article mainly summarizes the principles of EMW dielectric loss, magnetic loss, and EMW absorption and introduces in detail the synthesis and compounding methods of MXene and CPs and their research progress in radar absorption in recent years. In addition, this article also looks forward to their shortcomings, challenges, and prospects.

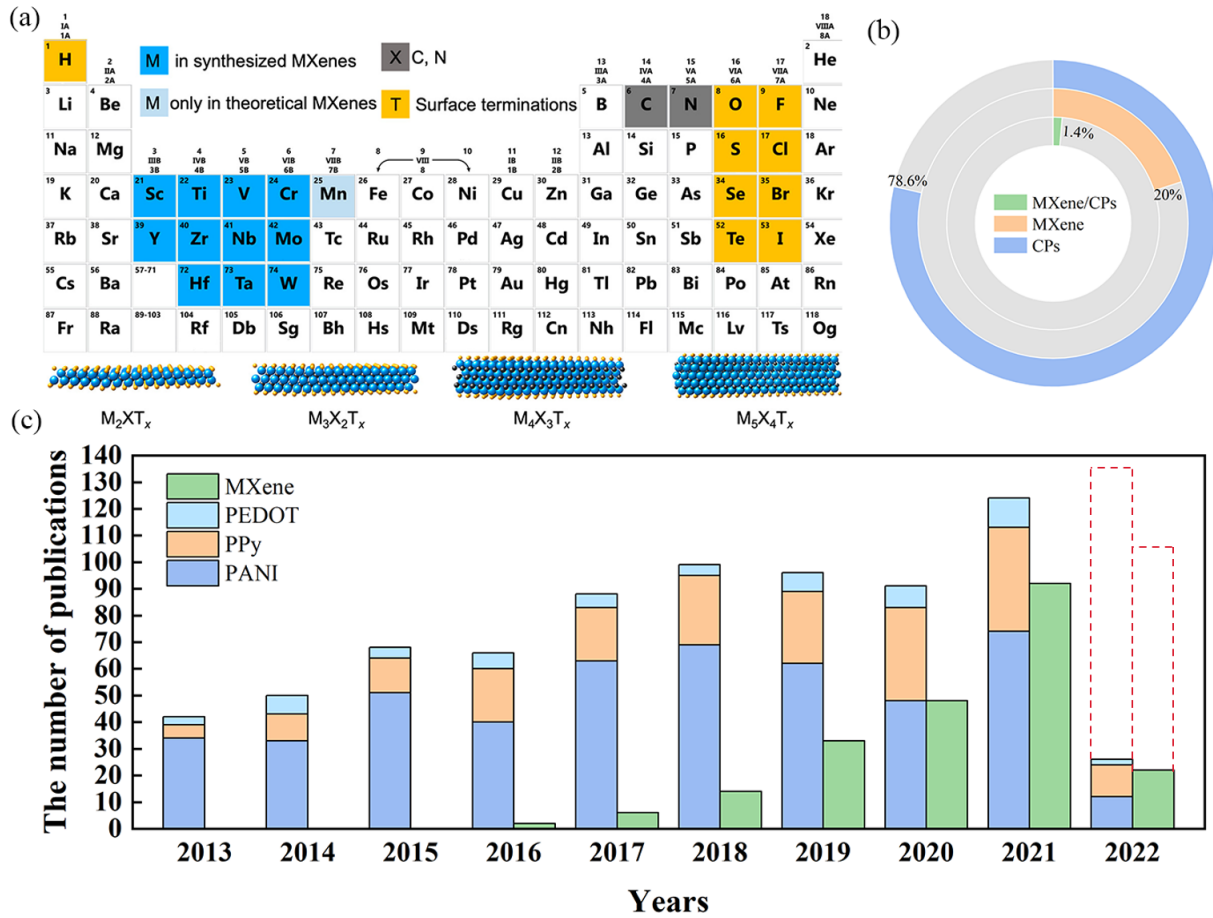


Fig. 1 (a) Periodic table displaying MXenes compositions. MXenes consisting of color-coded elements. Classic MXenes structures presented at the bottom [62]. Copyright 2021, American Chemical Society. (b) The percentage of CPs, MXene, and MXene/CPs absorbing materials in the last decade (the total number of the three is 910). (c) The number of EMW absorbing publications about MXene, PPy, PANI and PTh and their composites in the last decade.

2. Electromagnetic loss and absorbing mechanism

EMA materials are generally classified into EMI shielding materials with low reflectivity and radar absorbing materials (RAM) with high reflection loss (RL) value. EMI shielding materials enhance the effectiveness through conductivity enhancement, however, this results in electromagnetic pollution through secondary reflection [63]. The principle of an absorption-oriented EMI shielding material derived on this basis is shown in Fig. 2a. EMW are absorbed in the material as much as possible, allowing a certain amount of reflection to exist. The principle of RAM and EMI shielding materials is different. EMW can only be used as RAM if they are completely absorbed in the absorbing layer. RAM is applied in the form of coating to the outer layer of aviation, aerospace and other equipment. The absorbing principle is shown in Fig. 2b, where a metal substrate is placed behind the absorbing material to reflect the transmitted EMW. The reflection loss is defined as the difference between the initial incident wave and the final reflected wave, which is used to indicate the ability of the RAM to attenuate EMW [53]. Here, the absorption and the electromagnetic loss mechanism of RAM are introduced in detail.

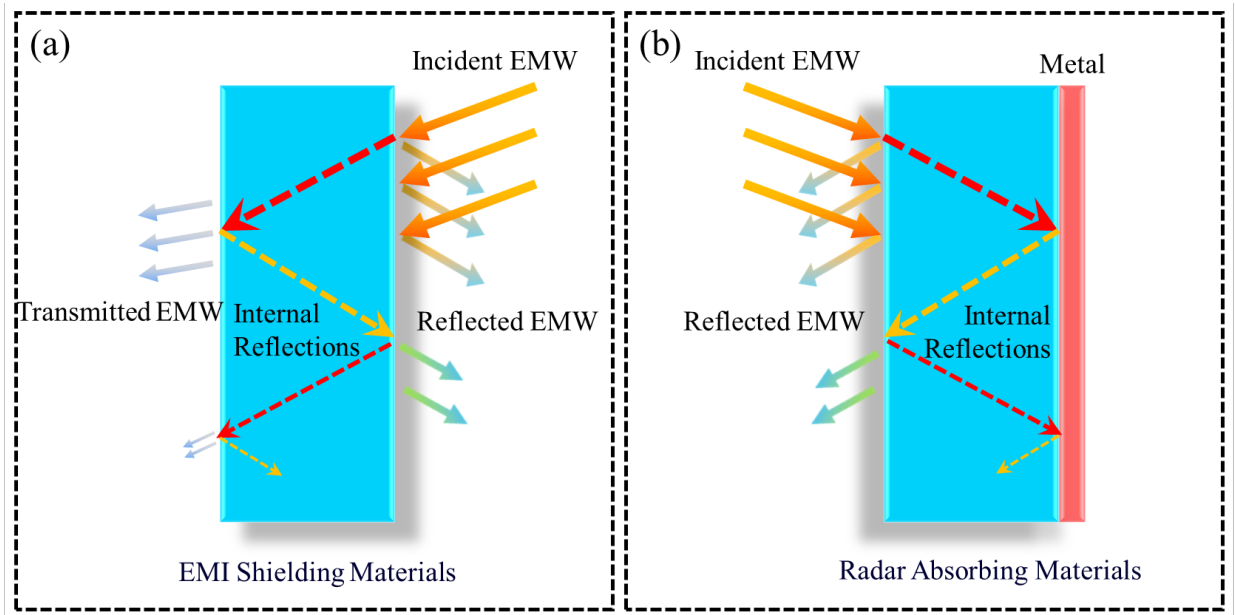


Fig. 2 The evaluation models of (a) EMI shielding materials and (b) radar absorbing materials.

2.1 Electromagnetic loss mechanism

2.1.1 Conduction loss

The most common conductive absorbing materials are metal materials with high conductivity. Other conductive materials such as carbon, MXene, carbon fiber, PANI, and other CPs have a conductive absorbing mechanism. When EMW are incident on the absorbing material, a reasonable structure and conductivity can bring about a multi-reflection effect as illustrated in Fig. 3a, c. This allows the EMW to be fully lost in the absorbing layer. Therefore, the reflection and secondary reflection of EMW or the penetration of electromagnetic energy due to too high or too low conductivity should be avoided as much as possible [64]. Under the radiation of EMW, the absorbing principle of conductive absorbing material is based primarily on the attenuation of EMW energy by the migration and transition of electrons in the material itself. Fig. 3b, d exhibit the

diagram of the conduction loss. Electron migration is due to the generation of induced electromotive force under the influence of EMW. In the presence of induced electromotive force, the directional movement of electrons occurs so that the EMW generates ohmic loss and converts energy into heat. The electronic transition is a function of temperature. Electrons are activated under high temperatures and jump over the barrier, giving rise to increased conduction losses. Metal materials form a current through the movement of free electrons, and a part of the energy is converted into heat and lost in the presence of resistance.

To maximize the electromagnetic attenuation, the material should have sufficient conductivity and the movement of carriers. Nevertheless, high conductivity is not the only criterion that requires high electromagnetic attenuation because connectivity is the main prerequisite for achieving overall high conductivity in the conduction path [65]. Therefore, a particular conductive network should be formed [66, 67]. CPs usually have a conjugated system, doped by chemical or electrochemical methods to introduce electrons or holes. The π system on the doped CPs chain easily releases free electrons, thereby improving its conductivity. A conductive network is formed to accomplish the aim of absorbing EMW [68].

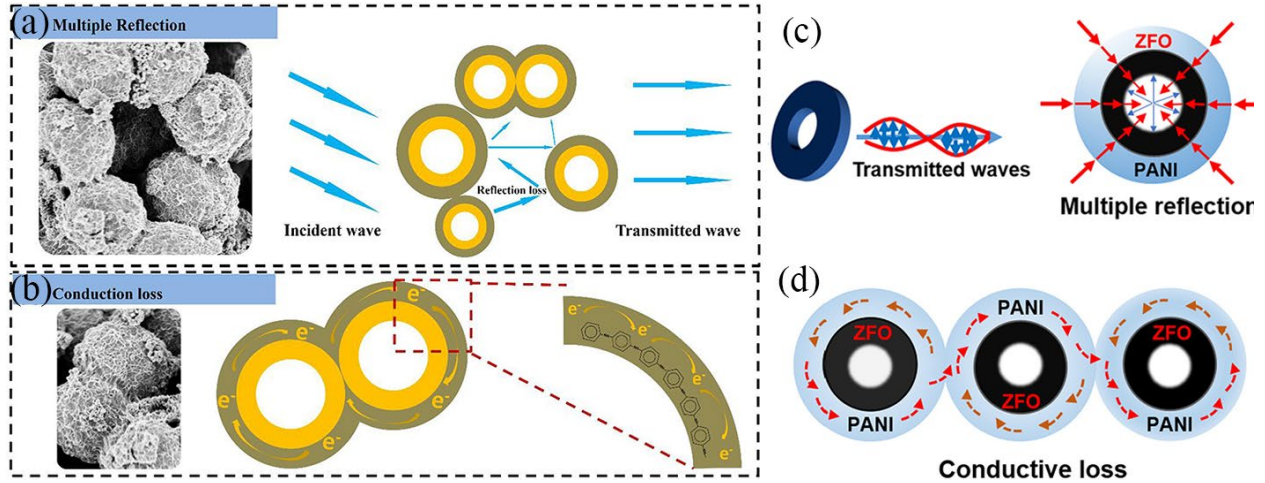


Fig. 3 Illustration of electromagnetic losses of H-MnO₂@PANI: (a) Multiple Reflection, (b) Conduction loss [69]. Copyright 2020. Elsevier. (c, d) Schematic diagram of possible MA mechanisms for hollow ZFO@PANI composites [70]. Copyright 2020. Elsevier.

2.1.2 Dielectric loss

The main reason for the research from conductive absorbing materials to dielectric absorbing materials is the various losses involved when EMW interact with substances in the GHz frequency range. Losses in this frequency range are not only attributable to ohm, conduction, but also to polarization losses [71, 72]. Dielectric performances usually refer to the answer of the bound charges, which merely move within the linear range of the molecule to the electric field [73]. Several parameters characterize it, and the first is the dielectric constant ($\epsilon_r = \epsilon' - j\epsilon''$), which exists in the form of a complex number. Where real part ϵ' of the complex permittivity represents the ability to reserve EMW, and the ϵ'' is the imaginary part denoting as the ability to dissipate EMW. Based on the free-electron theory, $\epsilon'' = \frac{\sigma}{2\pi\epsilon_0 f}$, increase in conductivity σ will improve imaginary parts ϵ'' , therefore, conduction loss can also be understood as a kind of dielectric loss

[74]. The second is the dielectric loss tangent ($\tan \delta_\epsilon = \epsilon''/\epsilon'$), which reveals the ability of a substance absorbing electromagnetic energy, followed by the conversion it into heat at a specific power and temperature. The higher the $\tan \delta_\epsilon$ is, the much more EMW energy can be absorbed [75].

The dielectric polarization can generally be divided into dipole polarization, interface polarization, electronic polarization, and ion polarization. Among them, electronic polarization and ion polarization correspond to the THz and PHz frequency bands, respectively, and have little effect on the research of RAM. Electric dipole and interface polarization correspond to the GHz band, which is the focus we should pay attention to. A dipole is commonly a pair of quite close together charges or "magnetic charges" having opposite signs. The positive and negative charges of the dipole do not overlap that can be observed graphically from the Fig. 4b. However, at the macroscopic interface composed of a large number of anisotropic dipoles, the resultant dipole moment is zero, showing electrical neutrality [76]. The dipole and interface polarization can be represented by the schematic diagram Fig. 4a. Under the interference of electric or magnetic fields, the dipoles are oriented due to different charges, resulting in dipole polarization. Furthermore, the dipoles are constantly pulled to produce torque, coupled with their irregular thermal motion, which will cause them to go on collide and resulting in energy loss [77]. Since the two materials with different dielectric constants, in the alternating electric field effect at the junction of the two phases, the charge rearrangement, forming positive and negative charges, are distributed across the interface to form an interface polarization. When in an alternating electric field, the directions of

the dipole polarization and the interface polarization are constantly changing, and when the speed of the polarization cannot catch up with the speed of the alternating electric field, dielectric relaxation and energy loss will occur. This means the establishment or change of the polarization state takes a period of time to reach another equilibrium state from one equilibrium state, and dielectric relaxation and energy loss will occur. The dielectric relaxation can be described by the Debye equation as following:

$$\varepsilon' = \varepsilon_{\infty} + \frac{(\varepsilon_s - \varepsilon_{\infty})}{1 + \omega^2 t^2} \quad (1)$$

$$\varepsilon'' = \varepsilon_{\infty} + \frac{(\varepsilon_s - \varepsilon_{\infty})\omega t}{1 + \omega^2 t^2} \quad (2)$$

$$\tan \delta_{\varepsilon} = \varepsilon_{\infty} + \frac{(\varepsilon_s - \varepsilon_{\infty})\omega t}{\varepsilon_s + \varepsilon_{\infty}\omega^2 t^2} \quad (3)$$

where ε_s , ε_{∞} , ω and t are static, optical dielectric constants, angular frequency, and relaxation time, respectively. According to formula (1) (2), they were eliminating ωt to get a semicircular equation called Cole-Cole circle [78, 79].

$$\left(\varepsilon' - \frac{\varepsilon_s + \varepsilon_{\infty}}{2}\right) + (\varepsilon'')^2 = \left(\frac{\varepsilon_s - \varepsilon_{\infty}}{2}\right)^2 \quad (4)$$

A mathematical transforming semi-circle Cole-Cole equation can obtain the simplified Cole-Cole equation:

$$\varepsilon' = \varepsilon_{\infty} + \frac{1}{t} \left(\frac{\varepsilon''}{\omega}\right) \quad (5)$$

When the dielectric performances are in accordance with Debye equation, the ε' and ε'' values come into being a semicircular arc, indicating that there is dielectric loss. As shown in Fig. 4c-e, in the front part of the Cole-Cole curve where the semicircle represents the dielectric loss mechanism, one semicircle represents a loss. The smooth part at the back end of the Cole-Cole

curve represents the conductive loss mechanism. the more semicircular arcs, the more loss mechanisms there are.

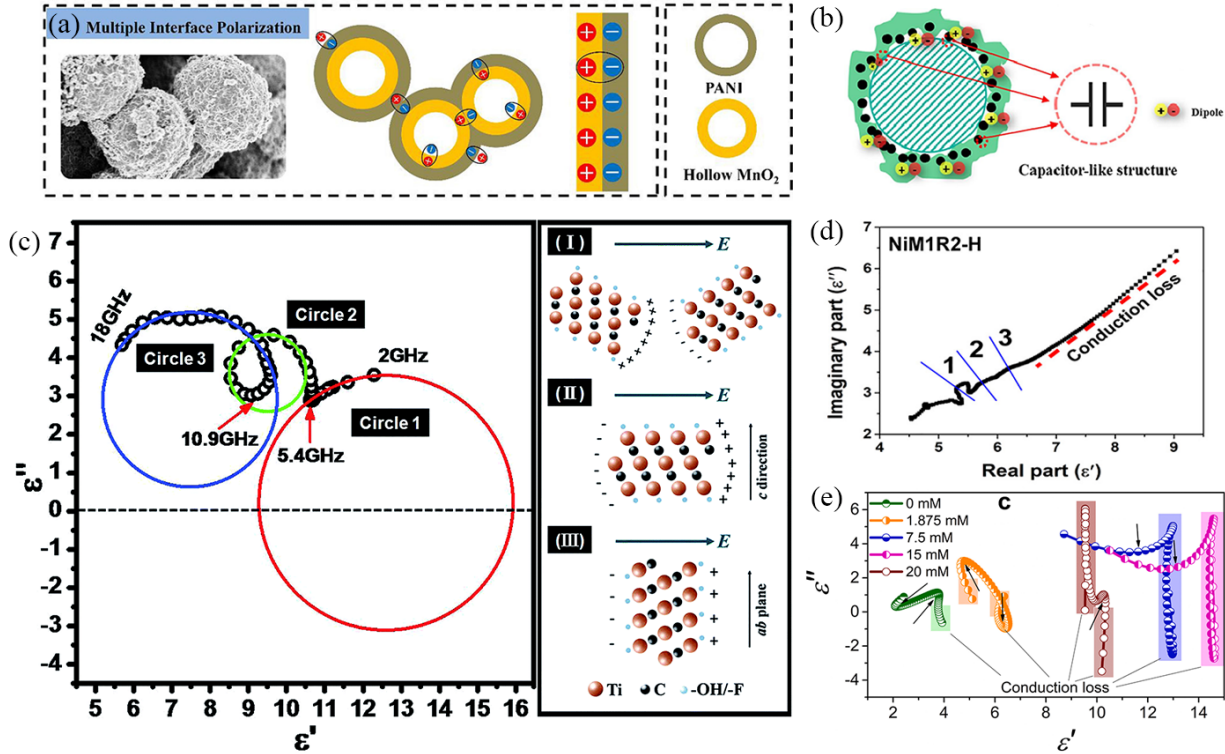


Fig. 4 (a) Illustration of multiple interface polarization of H-MnO₂@PANI [69]. Copyright 2020. Elsevier. (b) Interfacial polarization, dipole polarization, and capacitance-like structure [80]. Copyright 2021. Elsevier. (c) Cole-Cole image at 2-18 GHz and the corresponding electric polarization in Ti₃C₂ composites. [81]. Copyright 2018. RSC. (d) and (e) Corresponding loss of Cole–Cole diagram [82, 83]. Copyright 2021, American Chemical Society. Copyright 2021. Elsevier.

2.1.3 Magnetic loss

During magnetization and demagnetization processes, analogous to dielectric loss, part of the energy in the magnetic material is irreversibly converted into heat. This loss in energy is defined as magnetic loss [84]. The primary physical quantity is permeability. Permeability is not just the

potential gradient across a distance, but in the magnetic medium the ratio of the magnetic induction intensity B to the magnetic field intensity H ($\mu=B/H$). What we usually use is the relative permeability of magnetic media, which is defined as the ratio of permeability μ to vacuum permeability μ_0 ($\mu_r = \frac{\mu}{\mu_0} = \mu' - j\mu''$). The permeability of a material can also be understood as the measure of a material's capacity to simply sustain a magnetic field within its medium [85, 86]. Permeability is similar to relative permittivity. The real part μ' of relative permeability is the lossless interaction of EMW, representing the conversion of energy, and the imaginary part μ'' represents the attenuated part of the energy. The magnetic loss tangent ($\tan \delta_\mu = \mu''/\mu'$) denotes the ability absorbing electromagnetic energy to convert it into heat. Still, the larger the $\tan \delta_\mu$ is, the more energy of the EMW is effectively absorbed.

According to the strength of magnetism, magnetic materials are divided into two categories: strong magnetism and weak magnetism. Strong magnetism is manifested in the absence of an external magnetic field. In particular, ferromagnetic materials such as Fe, Co, Ni, and their oxides have high magnetic permeability, which are very potential magnetic absorbing materials. In the alternating environment, a ferromagnetic substance will also cause magnetic loss when magnetized, that is, the aforementioned imaginary part μ'' . Magnetic loss is generally separated into hysteresis loss, domain wall and eddy current effects, and exchange and natural resonances [87-89]. The hysteresis loss is the energy consumed to overcome the coercive force during the magnetization process. As shown in Fig. 5a, when the magnetic field applied to the right reaches the saturation magnetic field H_s , the material magnetizes along the dotted line to reach the saturation magnetic

induction B_s . When the intensity of the magnetic field H is reduced to 0, the magnetic induction intensity of the material does not drop to 0, which is called the residual magnetic induction B_r . Continue to implement the reverse magnetic field so that the magnetic induction intensity becomes 0. At this time, the magnetic field intensity is known as the coercive force H_c , and the hysteresis loss is the energy required to overcome H_c . In the alternating electromagnetic field, the greater the coercivity of the material has, the greater the hysteresis loss has [90, 91].

The domain wall effect corresponds to the loss in the MHz band, which is of minor significance to the absorption of GHz. The eddy current effect is based on the principle of electromagnetic induction. An induced current is formed in an alternating magnetic field, and a reverse induced magnetic field is further generated to achieve magnetic loss. The power loss resulted from by these currents is called eddy current loss. When the same resonance effect is an exactly incident EMW and the electron resonance frequency, resonance occurs will absorb some energy. Natural resonance takes place in the low GHz band, typically located 2-10 GHz. Resonance exchange generally occurs in a high frequency greater than 10 GHz [92]. Since the magnetic flux lines from magnetic materials formed, when the two magnetic substances close interaction of the magnetic flux lines in distorted form, a solid magnetic coupling effect, the electromagnetic loss is further increased. The electromagnetic loss of a magnetic material is not limited to the material itself. It can be seen from the simulation Fig. 5b that magnetic induction lines are distributed in space. This will be more favorable to the loss of EMW in space.

The magnetic loss mechanism can be described by the following formula [82].

$$C_0 = \mu''(\mu')^{-2}f^{-1} = 2\pi\mu_0\sigma d^2/3 \quad (6)$$

It can be recognized that in Fig. 5c natural and exchange resonances are shown as the ups and downs of the curve. The contribution of the resonance effect on the magnetic loss is relatively small compared to the eddy current effect. Almost the magnetic loss is only a result of eddy current loss, so C_0 is considered constant. Under this condition, the influence of eddy current on magnetic loss can be estimated.

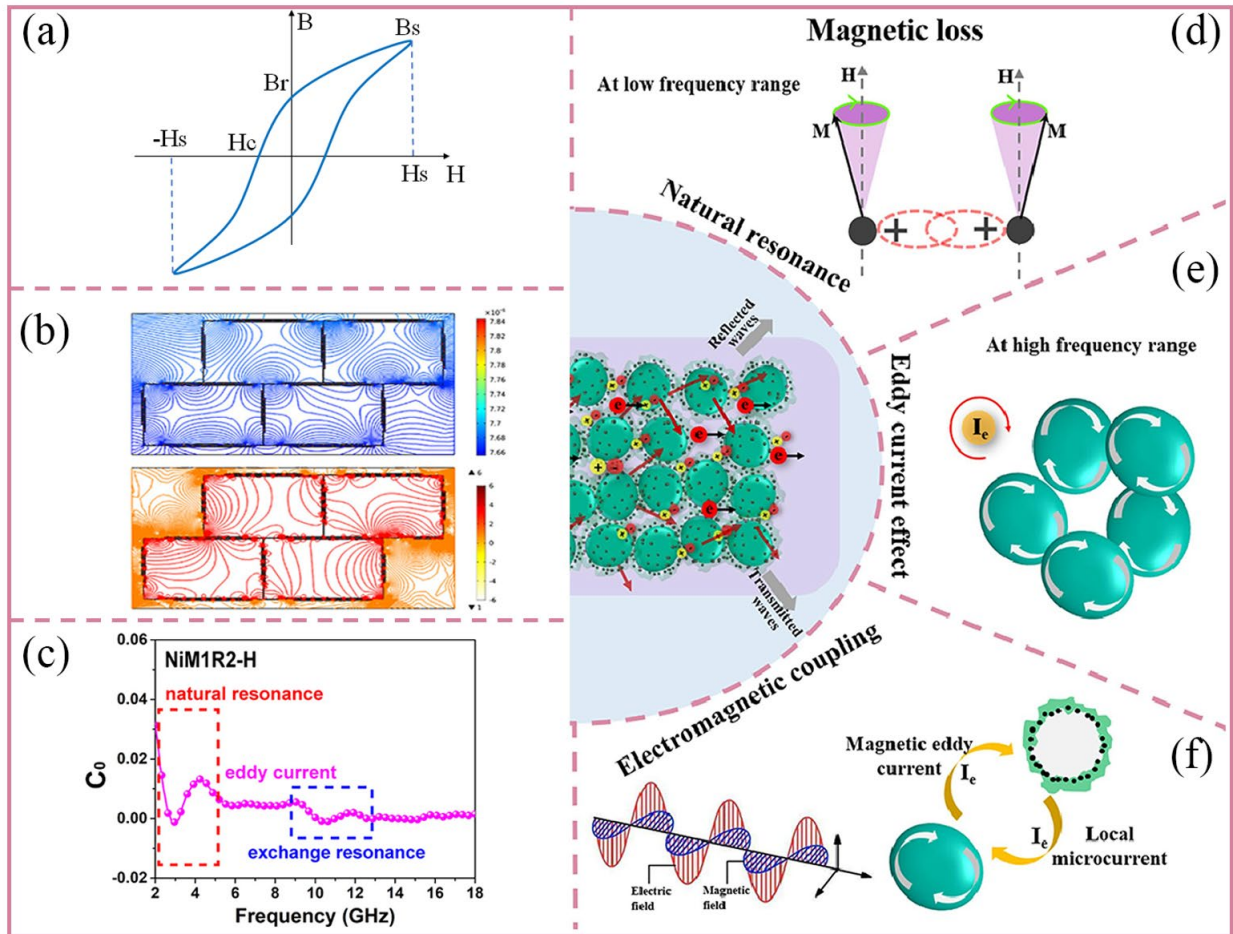


Fig. 5 (a) Schematic diagram of the hysteresis loop. (b) Finite element simulation for the schematic of electrical and magnetic coupling results and (c) the image of C_0 - f curve [82]. Copyright 2021, American Chemical Society.

The magnetic loss schematics include (d) natural resonance, (e) eddy current effect, and (f) electromagnetic

coupling effect, respectively [80]. Copyright 2021. Elsevier.

2.1.4 Loss and absorption of composite materials

A composite of two attenuation may better achieve the principle of dielectric and magnetic losses of the above. The combination of $\tan \delta_\epsilon$ and $\tan \delta_\mu$ can be used to describe the entire EMW dissipation capability. This dissipation can also be expressed by the attenuation constant α [93]:

$$\alpha = \frac{\sqrt{2}\pi f}{c} \times \sqrt{(\mu''\epsilon'' - \mu'\epsilon') + \sqrt{(\mu''\epsilon'' - \mu'\epsilon')^2 + (\mu'\epsilon'' - \mu''\epsilon')^2}} \quad (7)$$

Where c and f are the speed of light and frequency of the EMW, respectively. In addition to the attenuation ability of EMW, to have a good absorption performance in the end, it is also necessary to calculate the effective absorption of them. The reflection loss (R_L) of EMW can be utilized to express the effective absorption of EMW on the basis of transmission line theory [94-97].

$$R_L(dB) = 20 \log \left| \frac{Z_{in} - Z_0}{Z_{in} + Z_0} \right| \quad (8)$$

$$Z_{in} = Z_0 \sqrt{\frac{\mu_r}{\epsilon_r}} \tanh \left(j \frac{2\pi f d \sqrt{\mu_r \epsilon_r}}{c} \right) \quad (9)$$

Here Z_{in} , Z_0 , and d represent the impedances of the material and free space, and the thickness of the material, respectively. The absorbing material R_L has a critical value, $R_L < -10$ dB, meaning that 90% of EMW are effectively absorbed [46, 98]. The formula shows that R_L is a function of d and f , and the R_L can be plotted as a function of thickness d and frequency f to visually observe the absorbing performance. Fig. 6a is a 3D R_L plot fitted according to Eq. to show macroscopically the excellent condition of the material for EMW absorption performance. Fig. 6b, e are the

corresponding 2D plots, which allow the best EMA data to be clearly indicated due to the simplification of the experimental data. In addition, the absorption frequency width below -10 dB, which is called the effective absorption bandwidth (EAB), can be observed in the figure. The wider EAB means that the material has a wider field of action, which means better absorption performance. Depending on the formula (7), when $Z_{in}=Z_0$, $R_L=0$. That means the impedance matching is perfect, which is the ideal state of zero reflection in the design of the absorber [99, 100]. As it is shown in Fig. 6c, d the increase in the attenuation constant and the impedance $Z_{in}/Z_0 = 1$ are consistent with the best absorption trend [101]. It is an idea to study RAM by adjusting the ratio of composite materials to realize the most optimal impedance matching in the required frequency band.

Apart from the Z_{in}/Z_0 described above, impedance matching can also be described by the following notation [102, 103].

$$|\Delta| = |\sinh^2(Kfd) - M| \quad (10)$$

$$K = \frac{4\pi\sqrt{\varepsilon'_r\mu'_r} * \sin\left(\frac{\delta_e + \delta_m}{2}\right)}{c * \cos\delta_e \cos\delta_m} \quad (11)$$

$$M = \frac{4\mu' \cos\delta_e \varepsilon' \cos\delta_m}{(\mu' \cos\delta_e - \varepsilon' \cos\delta_m)^2 + \left[\tan\frac{\delta_m - \delta_e}{2}\right]^2 * (\mu' \cos\delta_e + \varepsilon' \cos\delta_m)^2} \quad (12)$$

It can be seen from the above formula (10-12) that the smaller the $|\Delta|$ value is, the better the impedance matching is. Fig. 6f intuitively shows that the impedance matching area is specifically distributed in different frequencies and thicknesses. This can also reflect the absorbing range and effective absorption of the absorbing material from the side. This $|\Delta|$ will be used together with

Z_{in}/Z_0 to describe impedance matching.

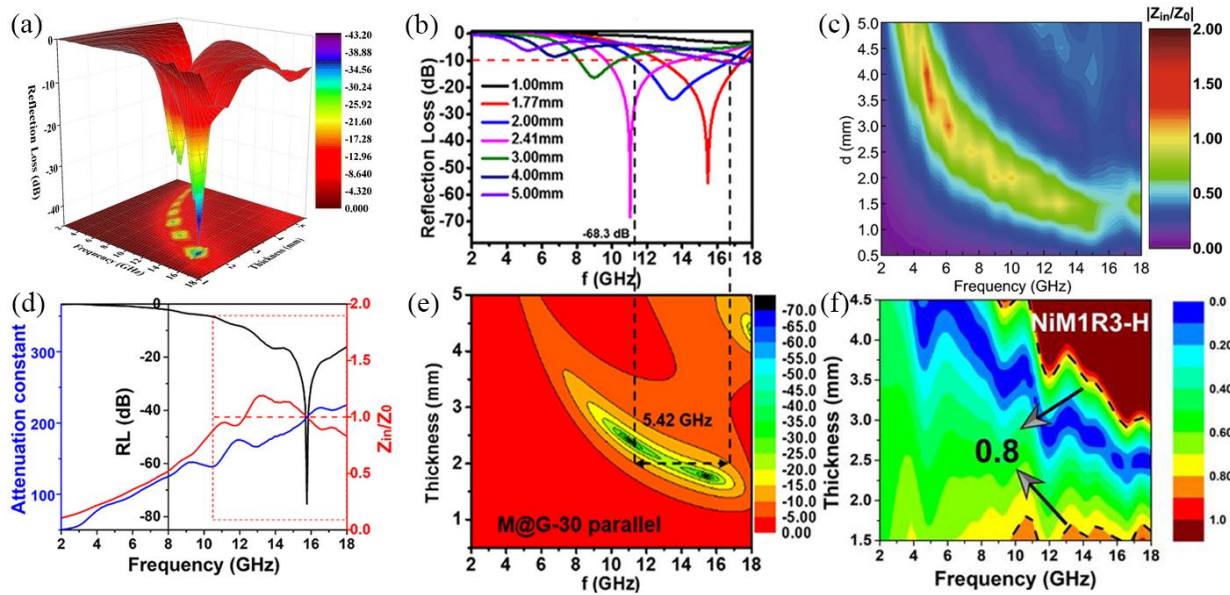


Fig. 6 (a) 3D R_L plots corresponding to different thicknesses and frequencies [104]. Copyright 2017. Springer Science Business Media. (b, e) 2D plots corresponding to 3D R_L plots, and 3D top views [105]. Copyright 2020. American Chemical Society. The images of (c) impedance matching ($|Z_{in}/Z_0|$) [106], Copyright 2020. The Author(s). and (d) $\alpha/R_L/Z$ - f curve (f) impedance matching ($|\Delta|$) [82]. Copyright 2021. American Chemical Society.

A material with a strong electromagnetic loss capability and a poor impedance match will result in EMW not entering the material and being reflected directly out, as shown in Fig. 7c. However, it can be found from Fig. 7a that the EMW will be reflected on the metal substrate when the material has a good impedance match but not enough attenuation capability. In both cases, the reflected EMW are detected by radar. Fig. 7b showing the ideal state of impedance matching and attenuation capability. All EMW are directly absorbed and converted into heat to dissipate. The

depth of penetration of the EMW shown in Fig. 7c is called the skinning depth, which is calculated by the following equation.

$$D_p = \frac{\lambda_0 \sqrt{\mu'}}{2\pi \varepsilon''} \quad (13)$$

In which λ_0 ($\lambda_0=12.2$ cm) denotes as the free space EMW length for 2.45 GHz. As ε'' increases, the skin depth will inevitably decrease. At the same time, the formula $\varepsilon'' = \frac{\sigma}{2\pi \varepsilon_0 f}$ is mentioned in 2.1.2 Dielectric loss. High conductivity can increase the value of ε'' and at the same time bring about the consumption of intense EMW. However, the impedance mismatch caused by high conductivity will bring more reflections.

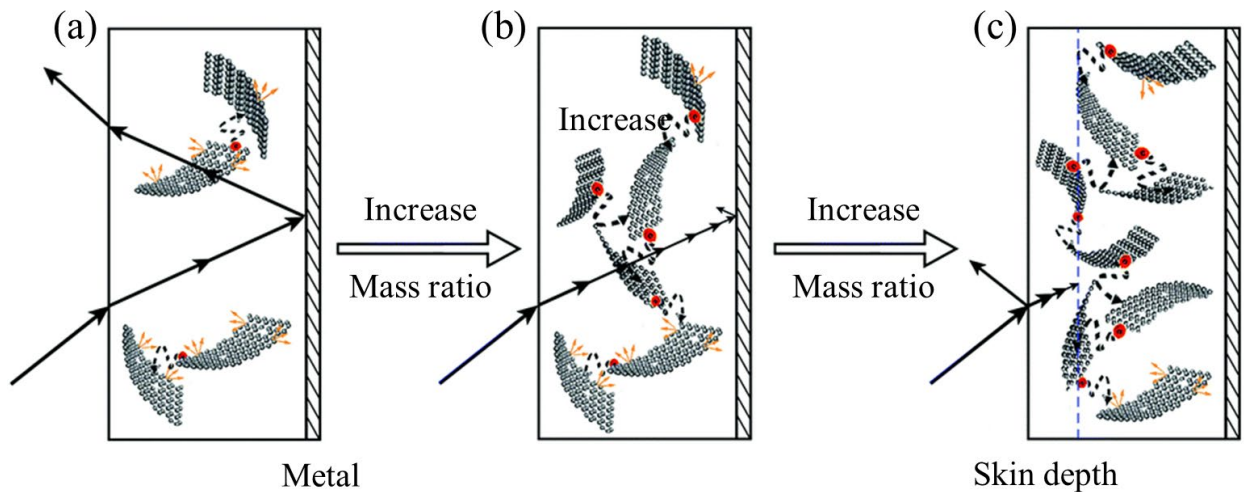


Fig. 7 The situations of the EMW absorber responsive to the EMW: (a) good impedance matching with weak attenuation, (b) good impedance matching with strong attenuation, and (c) poor impedance matching with strong attenuation [107]. Copyright 2018. Royal Society of Chemistry.

At the macroscopic level electromagnetic attenuation follows the quarter-wave impedance theory with the following equation [108].

$$d_m = \frac{nc}{4f\sqrt{|\mu_r||\varepsilon_r|}} (n = 1,3,5 \dots) \quad (14)$$

When the above formula (14) is satisfied, the EMW passes through the internal boundary of the absorbing layer and comes to the outer boundary of the absorbing layer again after reflection. At this time, the phase difference is exactly 180° between the incident wave and reflected wave. Through the principle of wave interference, it is known that the EMW in this state is theoretically possible to achieve complete dissipation. This mutual cancellation at the absorbing layer interface can be used to explain why, under the same conditions, the absorption effect of a thicker absorbing layer is worse than that of a thinner one.

2.2 Absorbing mechanism of materials

2.2.1 Absorbing mechanism of MXene

The main reason why MXene is invoked as a EMW absorbing material is its good conductivity, high specific surface area, plentiful surface functional groups, and good processing and compounding properties. The first is the influence of conductivity on EMW absorption. Lipatov et al. [109] tested the resistivity of individual and multilayer Ti₃C₂T_x flakes. The single-layer Ti₃C₂T_x flakes displays a small resistivity of 2.31 ± 0.57 μΩ m (corresponding conductivity of 4600 ± 1100 S cm⁻¹). However, the multilayer Ti₃C₂T_x film has a resistivity of 15.8 ± 1.3 μΩ m, which is just an order of higher than that of the single-layer Ti₃C₂T_x.

The primary conductive loss mechanism of MXene can be shown in Fig. 8a-c. Each layer of MXene can be understood as a conductive element in a regional area, and multiple layers are superimposed to form a relatively more complex conductive network. Electrons can absorb

electromagnetic energy and move to the interlayer channels and the surface, and whereafter these migrated electrons dissipate energy through the collision with the crystal lattice [110]. When migrated electrons dissipate energy through the collision with the crystal lattice [110]. When defects appear in the conductive sheet of MXene, the migration of electrons will be blocked. At this time, part of the electrons are stimulated by electromagnetic radiation to gain enough energy to cross the barrier of the defect and realize the transition of the electron in the defect of MXene. In the same way, when the distance between two layers is relatively close, a similar electron movement will also occur, jumping from one layer to another. Therefore, the relatively high conductivity is an essential factor for MXene to absorb EMW.

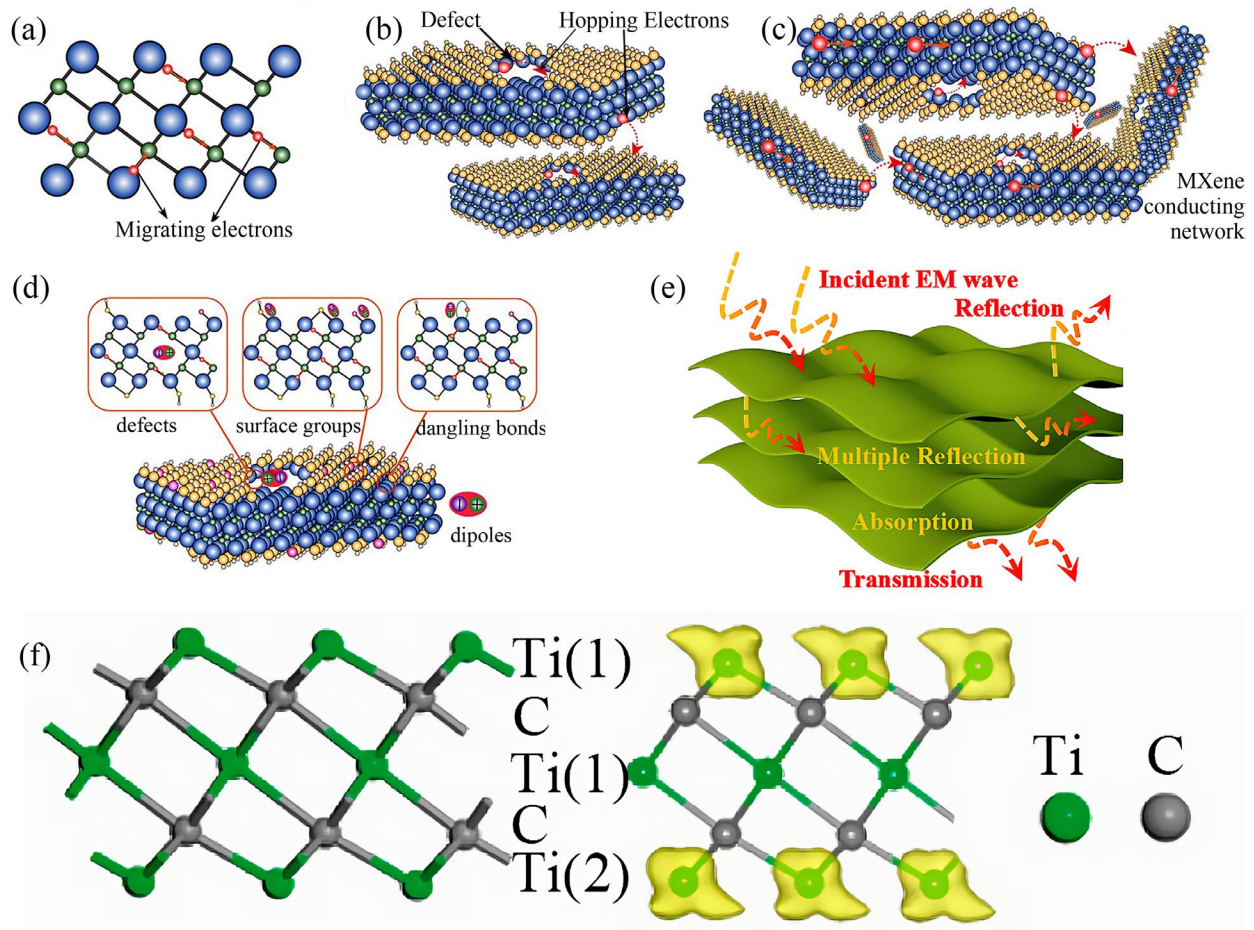


Fig. 8 (a) Migrating electrons and (b) hopping electron transport across defects and (d) dipolar polarizations in

(c) MXene conductive network [76]. Copyright 2018. Elsevier. (e) Multi-reflection diagram of MXene [111]. Copyright 2018. Elsevier. (f) Side view of the bare Ti_3C_2 monolayer consisting of a quintuple layer with Ti(1)-C-Ti(2)-C-Ti(1) stacking modes and the computed spin density distribution [112]. Copyright 2012. American Chemical Society.

The most crucial reason for MXene as an absorbing material is its dielectric loss. Whether it is because of its etching method or its own stability, MXene will inevitably introduce surface-active functional groups after etching. The etching methods include HF, HCl + LiF in-situ, fluorine-free, molten salt etchings, etc. These methods will introduce a large number of surface functional groups for example -OH, -O. Apart from fluorine-free etching, other methods will also introduce -F. MXene, which has no end groups, does not currently exist. As shown in Fig. 8d, MXene is precise because of -O, -F, -OH, and other surface terminations or defects, leading to asymmetric charges for distribution. That contributes to the construction of dipoles. These dipoles can convert electromagnetic energy into thermal energy due to relaxation losses in the presence of an electromagnetic field. Of course, when MXene is compounded with other materials, the interface will be polarized owing to the difference in electrical conductivity of the interface. For example, $\text{Ti}_3\text{C}_2\text{T}_x$ MXene chemically reacts with CO_2 and O_2 in the air, and part of Ti will be oxidized to TiO_2 . Capacitive structures can be formed in the interface between MXene and TiO_2 nanoparticles or the contact of MXenes sheets. Thus, charges may assemble on these sites, results in the interface polarization, and enhance EMW absorption ability. Of course, in order to get better loss, the EMW needs to stay longer in the absorbing layer. As shown in Fig. 8e, the layer structure

of MXene can bring multiple reflections to achieve the intended purpose.

However, as the content of surface terminals such as -O, -F, -OH increases, the conductivity decreases. Although the conductivity drops, these surface end groups bring more defects to the conductive network and correspondingly increase the energy loss caused by the electronic transition in MXene. However, in terms of magnetic loss, MXene has a larger gap compared with dielectric loss. Taking the most common $Ti_3C_2T_x$ MXene as an example, the $Ti_3C_2T_x$ layer possesses a magnetic ground state having a total magnetic moment per unit of about $1.93 \mu_B$, and surface functional groups such as $Ti_3C_2(OH)_2$ and $Ti_3C_2F_2$, which are ground state non-magnetic. It can be seen that the induced magnetism of Ti_3C_2 comes from the suspended 3D orbitals of Ti atoms on the surface from the spin density distribution (Fig. 8f) [112]. The magnetic loss of MXene is relatively poor because it loses its magnetism after adding surface functional groups.

2.2.2 Absorbing mechanism of CPs

CPs are distinct from other polymers as absorbing materials in that they are conductive first. The electromagnetic energy is first and foremost attenuated by CP's resistance and dielectric polarization relaxation loss. Effective conductivity helps increase conduction loss and promote the consumption of EMW [113, 114]. CPs are polymer materials whose conductivity can extend from insulation state to conducting state after doping. In all CPs conjugated molecules, the sigma bond is a localized bond and constitutes the molecular skeleton. The p orbitals perpendicular to the molecular plane combine to form delocalized π bonds, and all π electrons move within the entire molecular skeleton [115]. The appearance of delocalized π bonds improves the range of π electron

activity, reduces the energy level of the system, reduces the energy level interval, and increases the conductivity of the material. Alternating single bond and double bond conjugated structure is the common feature of CPs materials.

The intrinsic state of the conjugated polymer is in an insulating or semiconductor state and can be transformed into a conductive state after or n-type (electron) doping or p-type (hole) doping [116]. Doping can obviously increase its conductivity, which is on the brink of the electrical conductivity of metals. The conductivity of CPs is affected by the conjugation length, polaron length, total chain length, and charge transfer to adjacent molecules [117]. After being doped, CPs show electric charges and combine with ions of opposite electric properties to form polaron, bipolaron, and Soliton. Under the interference of the electric field part of the EMW, the existence and transition of these polaron and soliton will cause the consumption of EMW energy. The specific macroscopic manifestation is the case that the conductivity of the material is not zero. An induced current is created in the material to generate Joule heat so that the EMW energy is dissipated. In addition to these Soliton inter-jumping and intra-chain hopping of bipolarons theories. Conduction can also be explained by theoretical models such as lattice vibration-assisted transition between localized states, 3D variable range transition, and tunneling with limited charge energy between electrical domains [118].

The second is the dielectric properties of CPs. The absorbing properties of CPs are related to the dielectric constant. The dielectric constant is linked to the electrical conductivity, and when the semiconductor is a CPs doped state, i.e., an electric conductivity of $0.1 \sim 100 \text{ S}\cdot\text{cm}^{-1}$, it has a high

dielectric loss. The pendant functional groups in the long chain of the CPs are extremely easy to form dipoles and interface polarization between the two interfaces. In an alternating electric field, the polarization speed cannot keep up with the frequency of the electromagnetic field, and the loss of EMW is caused by dielectric relaxation.

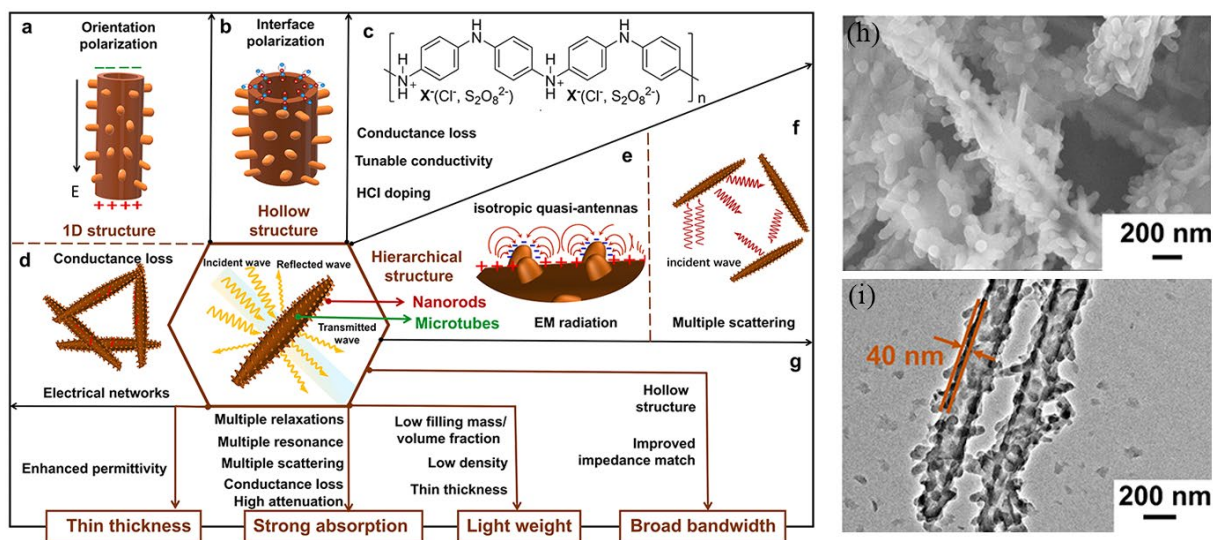


Fig. 9 (a-g) The EMW absorption mechanism and the (h) SEM and (i) TEM images of PANI hierarchical nanotubes doped with HCl [83]. Copyright 2021. Elsevier.

Yang et al. [83] used PANI nanorods as an example to clarify the electromagnetic loss mechanism of CPs. The structure of PANI hollow nanorods is shown in SEM image Fig. 9h and TEM image Fig. 9i respectively. Fig. 9a shows the orientation polarization caused by anisotropic one-dimensional (1D) nanostructures. Fig. 9b shows the large specific surface brought by the hollow structure, which is conducive to the relaxation of the medium and the polarization of the interface. Fig. 9c is the abridged general view of the increase in conductivity by doping different counter ions. Fig. 9d shows the existence of EMW, which induces dissipation current in the

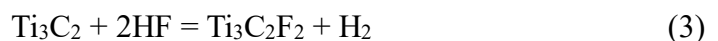
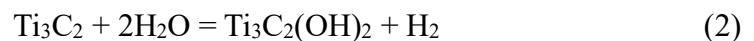
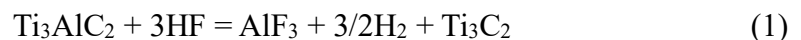
nanorod structure, which leads to conduction loss. According to the principle of electromagnetic induction, a certain diamagnetic field will be formed. Fig. 9e shows the electric energy radiated from the induced electric field of PANI and converted into magnetic energy. With the addition of isotropic multi-scattering effect, the CPs have excellent electromagnetic loss ability.

3. Synthesis methods of MXene and CPs

3.1 Etching methods of MXene

3.1.1 HF etching

In the MAX phase, M-A is a metal bond. Because of the strong interlayer chemical bond between M and A, mechanical peeling of the MAX phase is virtually impossible [119, 120]. M-X is a covalent bond, and the connection of the metal bond is relatively low in the strength of the covalent bond. This provides a theoretical basis for selectively etching the A layer to form the MX 2D nanolayer. Fig. 10a shows the HF etching MAX phase to manufacture MXene. Fig. 10c-f are the SEM image of different MAX phases etched by HF. In the order they are SEM micrographs for Ti_3AlC_2 particle before treatment, and Ti_3AlC_2 , Ti_2AlC , and Ta_4AlC_3 after HF treatment respectively. Naguib et al. [37] used HF to etch the Al atoms of Ti_3AlC_2 for the first time at room temperature and ultrasonically dispersed the $Ti_3C_2T_x$ 2D nanoflake layer, first to open the way to obtain MXene by etching. The equations involved in Ti_3AlC_2 etching are as following:



It can be found that it is inevitable to introduce -OH, -F, and other surface terminals through HF etching from the above equations (2) and (3), which makes the surface negatively charged. Fan et al. [34] used a laser beam to irradiate the HF-etched $\text{Ti}_3\text{C}_2\text{T}_x$ solution, and the noticeable Tyndall effect appeared, indicating that the $\text{Ti}_3\text{C}_2\text{T}_x$ was dispersed and gelled. In a low-content HF solution, even if the etching time is increased, Al cannot be completely etched. Increasing the HF content will increase the etching speed. However, it will also bring about etching defects [121], and an increase in the content of -O, -F, and -OH surface terminations and a decrease in electrical conductivity.

Multi-layer MXene has strong interlayer interaction. It is difficult to obtain large-scale delamination MXene flakes through superficial mechanical peeling, and it is necessary to add the intercalating agent to achieve delamination. Commonly used intercalants are dimethyl sulfoxide (DMSO), urea, amines, and so on. Thereinto, DMSO can be as one of the most successful intercalants, and $\text{Ti}_3\text{C}_2\text{T}_x$ would form a jarless dispersion in it with a longer duration [122]. Mashtalir et al. [123] used DMSO as an intercalant, inserted between HF-etched Ti_3C_2 nanosheets, and then treated them with ultrasonic EMW in the water to obtain a small amount or monolayer of MXene. Wu et al. [124] used a high energy mechanical grinding way to obtain few-layer MXene nanosheets with a higher yield, of which DMSO acts as a solvent and intercalation agent. Compared with the MXene electrode obtained without DMSO, it has an excellent reversible capacity, reaching 267 mA h g^{-1} at 100 mA g^{-1} , higher than that of the original MXene (less than 100 mA h g^{-1}). After 500 cycles, 196 mA h g^{-1} can still be reached. For other MXene members

such as Nb₂CT_x, Mashtalir et al. [125] used isopropyl amine instead of DMSO as an intercalant, and Nb₂CT_x was dispersed by HF etching and isopropyl amine intercalation. The intercalation mechanism is illustrated in the Fig. 10b. The mechanism of action of amines is that ammonium ions R-NH⁺ are formed, when it is blended with H₂O. The surface of Nb₂CT_x MXene is negatively charged. In addition, the small size of the terminal alkyl groups can effectively defeat the steric hindrance during insertion. At the same time, these alkyl groups can promote MXene layers apart and weaken the interaction between them. After isopropyl amine intercalation etching, the SEM and TEM images are shown in Fig. 10g, h, respectively. Therefore, it is inserted between the layers with the assistance of the electrostatic force to achieve delamination.

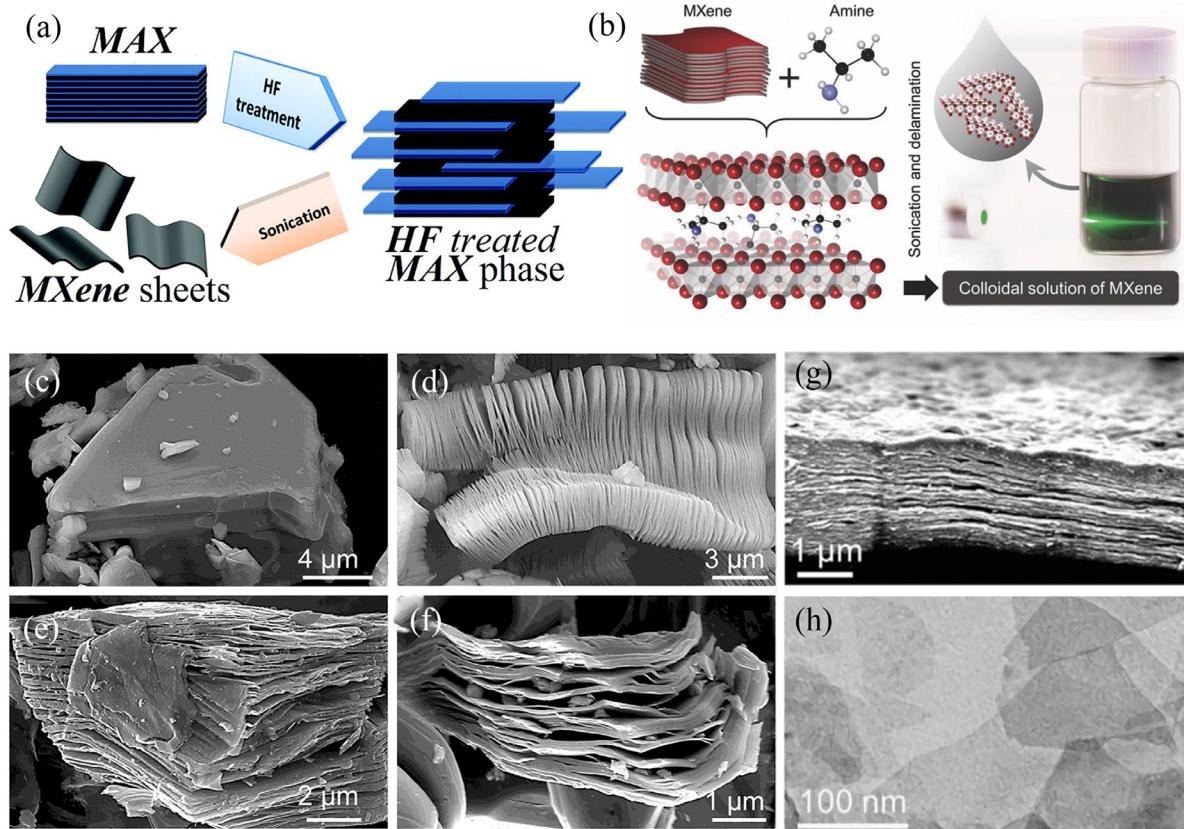


Fig. 10 (a) Schematic illustration of the formation of MXene. SEM image for (c) Ti₃AlC₂ particle before treatment, (d) Ti₃AlC₂, (e) Ti₂AlC, and (f) Ta₄AlC₃ after HF treatment [126]. Copyright 2012. American Chemical Society. (b) Schematic of Nb₂CT_x delamination process via isopropyl amine intercalation, (g) SEM and (h) TEM images of d-Nb₂CT_x flakes [125]. Copyright 2015. WILEY-VCH.

3.1.2 In situ HF etching

LiF-HCl serves as currently one of the most widely used etchants for the synthesis of high-quality MXenes. Ghidui et al. [127] initially etched Ti₃AlC₂ in situ by HCl and LiF to obtain clay-like and ultra-high conductivity MXene. Among them, Li⁺ acts as a pre-intercalation layer, weakening the interaction between the plates and making ultrasonic dispersion easier. The

schematic diagrams are shown in Fig. 11a, b, and the image compare the process of obtaining multilayer MXene ($M-Ti_3C_2T_x$) and ultrathin MXene ($U-Ti_3C_2T_x$) by etching MXene with HF and LiF+HCl. $M-Ti_3C_2T_x$ has more -F functional groups, while $U-Ti_3C_2T_x$ has more -O. As shown in Fig. 11e, f, when the distance between $M-Ti_3C_2T_x$ is too large, the electrons cannot jump between the two $M-Ti_3C_2T_x$ and cannot form a conducting network. However, $U-Ti_3C_2T_x$ can compensate this defect. In addition, as shown in Fig. 11g, h, EMW increase the chance of attenuation in the random multiple reflections of EMW from $U-Ti_3C_2T_x$ composites. The multi-sheet layer is more inclined to the application of EMI shielding, and the single sheet layer is more beneficial for EMW absorption.

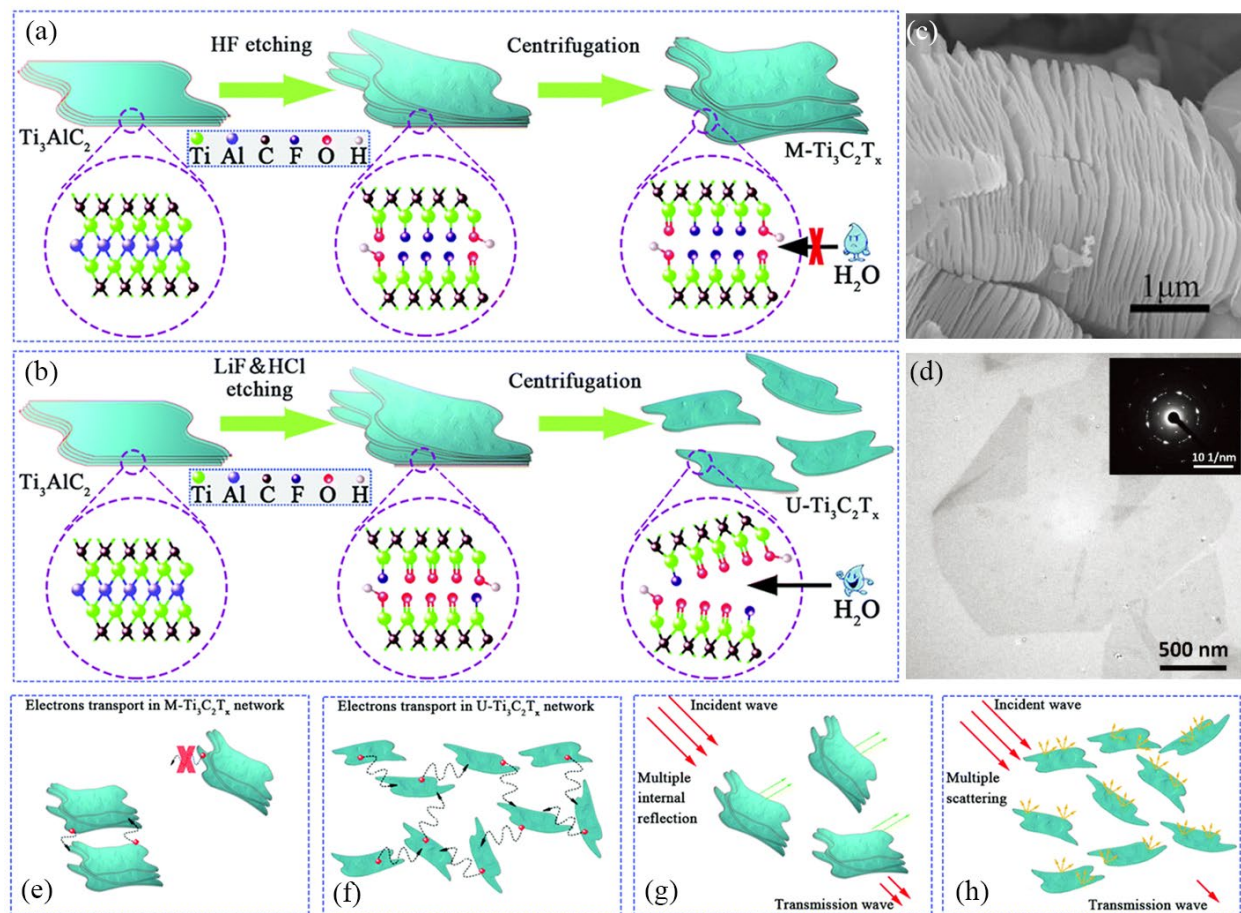


Fig. 11 Preparation of (a) $M\text{-Ti}_3\text{C}_2\text{T}_x$ and (b) $U\text{-Ti}_3\text{C}_2\text{T}_x$ MXenes, and their corresponding (e) and (f) local conductive network. Microwave propagation models of (g) $M\text{-Ti}_3\text{C}_2\text{T}_x$ and (h) $U\text{-Ti}_3\text{C}_2\text{T}_x$ composites [128]. Copyright 2017. RSC Pub. (c) SEM images of $\text{Ti}_3\text{C}_2\text{T}_x$ etched by HF [129]. Copyright 2016. American Chemical Society. (d) SEM image of $\text{Ti}_3\text{C}_2\text{T}_x$ etched by LiF+HCl [130]. Copyright 2019. WILEY.

Wu et al. [131] obtained MXene nanosheets with an average thickness of 3.7 nm as shown in Fig. 12b and conductivity of $3.3 \times 10^5 \text{ S m}^{-1}$ by in situ etching Ti_3AlC_2 and ultrasonic dispersion in an argon atmosphere. The surface of MXene has many exposed metal atoms, which are thermodynamically in a metastable structure, so having high surface energy. Even in the air environment, if it is not protected, it is easy to be oxidized. Ultrasonic dispersion treatment will

accelerate the oxidation of MXene [132]. Ultrasonic dispersion will reduce the size of the MXene sheet in order to obtain a larger sheet. Fan et al. [34] replaced the ultrasonic dispersion with a hand-cranked method to get a single-layer or a few-layer 2D MXene. By comparing the Fig. 12b-e, it can be observed that the MXene lamella obtained by hand shaking is significantly larger. The lightweight MXene-reduced graphene oxide foam was prepared via the combination of freeze-drying and reduction heat treatment. Compared to multi-layer MXene, monolayer MXene obtained by hand shaking method is more favorable for the increase of electrical conductivity. It has desirable electromagnetic properties. On this basis, the EMA properties can be improved by compounding or hybridization. MXene by in-situ etching has a very high potential for applications in the direction of EMA.

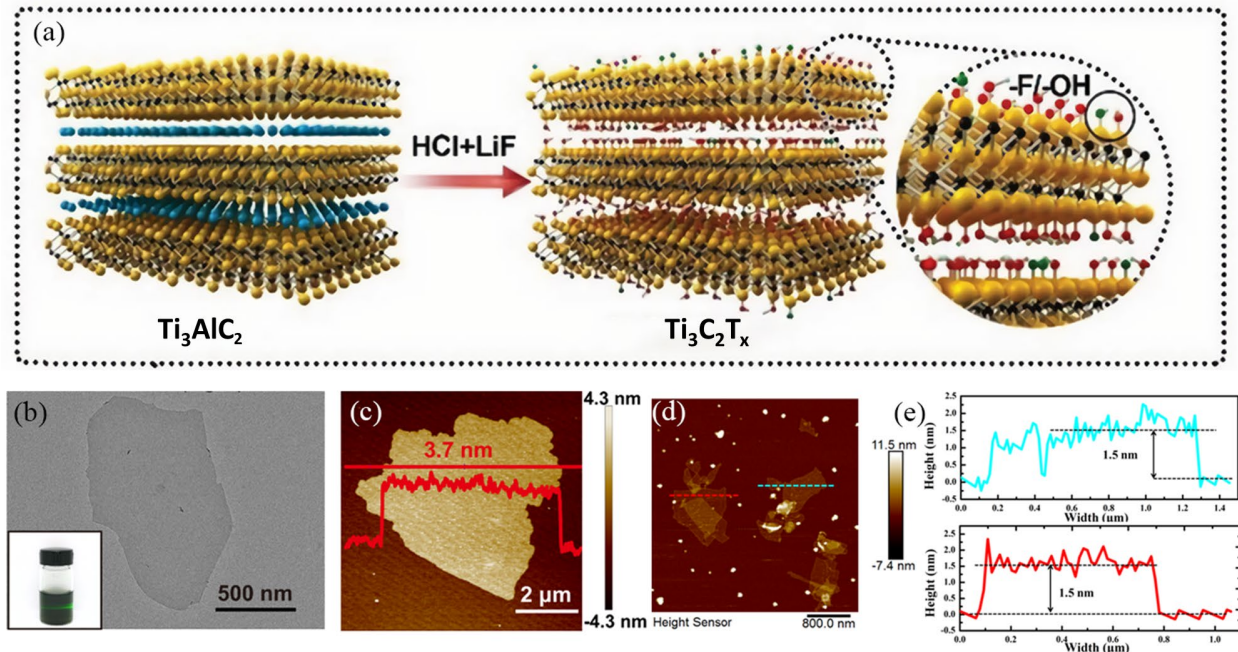


Fig. 12 (a) Schematic illustration of the preparation of $Ti_3C_2T_x$ MXene [130]. Copyright 2019. WILEY. The (b)

TEM of $Ti_3C_2T_x$ nanosheet and photograph of uniform MXene colloid suspension with a Tyndall effect. (c) AFM

image of $\text{Ti}_3\text{C}_2\text{T}_x$ nanosheet with ultrasonic treatment [131]. Copyright 2019. Elsevier. (d, e) AFM image of the $\text{Ti}_3\text{C}_2\text{T}_x$ MXene nanosheets by hand shaking [34]. Copyright 2019. Elsevier.

3.1.3 Fluoride-free etching

Using HF or LiF/HCl solution or molten fluoride salt as an etchant poses considerable safety and handling problems. HF can cause burns to human skin, invade bones, and severe tissue damage or even death [133]. At the same time, using HF and fluoride salt for etching, it is inevitable that F atoms will be introduced. Because F is inert, it will affect the specific capacitance of MXene [134]. In order to achieve fluorine-free etching, Zhang et al. [135] were inspired by the Bayer process, taking the lead in synthesizing fluorine-free high-purity $\text{Ti}_3\text{C}_2\text{T}_x$ MXene using hydrothermal alkaline etching technology. The purity of $\text{Ti}_3\text{C}_2\text{T}_x$ with -OH, -O surface end groups is as high as 92%. The mass specific capacitance of $\text{Ti}_3\text{C}_2\text{T}_x$ obtained by this method exceeds that of HF- $\text{Ti}_3\text{C}_2\text{T}_x$ by about 214%, and it is enhanced by about 28.2% compared to LiF+HCl $\text{Ti}_3\text{C}_2\text{T}_x$. Even if the etching conditions are very harsh, MXene has to be etched in NaOH at a concentration of 27.5 mol/L at 270 °C. However, this method can avoid the introduction of F-containing compounds during the synthesis process. This is a promising etching method.

At the same time, the application of electrochemical etching methods has improved the development prospects of fluorine-free etching. Generally speaking, all MAX phase etching methods belong to inherent electrochemical processes based on electron transfer in a classic chemical etching process. Almost every active sites of the surface will participate in the electron transfer reaction, serving as an anode or a cathode [136]. Therefore, electrochemical etching is a

trustworthy alternative way. Green et al. [137] successfully etched Ti_2AlC into Ti_2CT_x in a 2 mol/L HCl solution at 0.6 V for five days. This process doesn't involve any fluoride ions and only produces MXenes with -OH, O, and Cl end groups. While etching Al, a slightly higher voltage will cause part of Ti to be removed, forming a thin amorphous carbon layer which hinders the further etching behavior. So, the etching voltage must be balanced to generate MXenes and avoid excessive etching. Ti_2AlC is electrochemically etched into a three-layer structure. The SEM image of MXene through electrochemical etching and chemical etching is shown in Fig. 13b, c. It can be found that the electrochemically etched MXene has a more complete sheet structure. However, if the experimental parameters are not properly controlled, it is very easy to further etch away Ti. The structure is composed of carbide-derived carbon (CDC), MXene, as well as unetched MAX from the outside to the inside. With the aid of water bath ultrasound, MXenes are further separated from the three-layer structure. MXenes can be further separated from this three-layer structure by ultrasound. A core-shell model (Fig. 13a) is used to explain the electrochemical etching of Ti_2AlC on Ti_2CT_x and CDC.

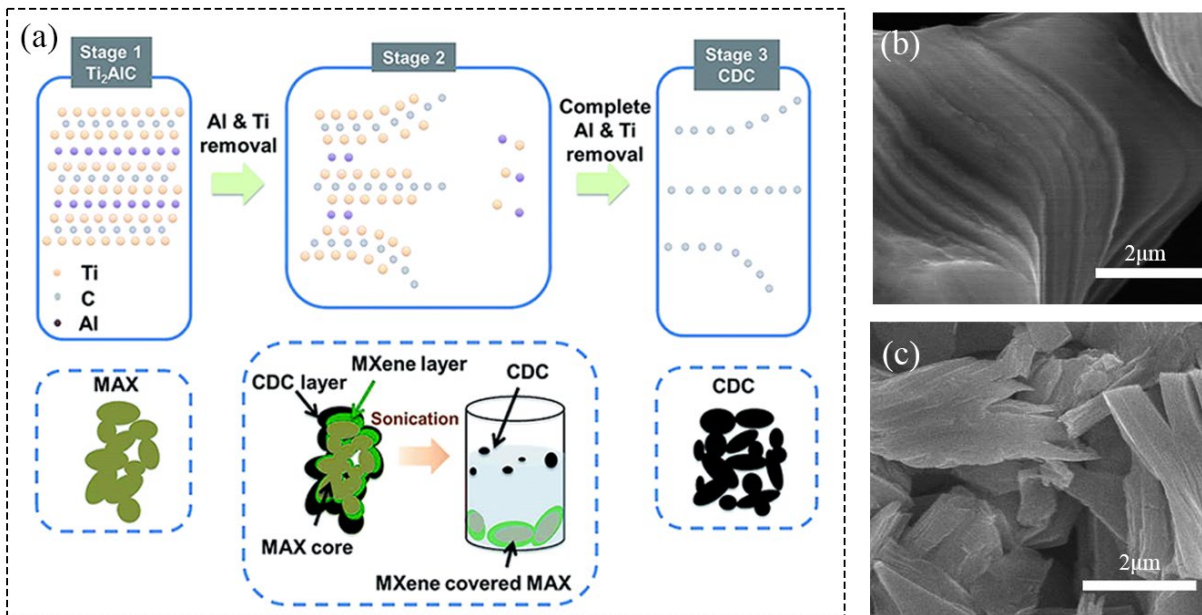


Fig. 13 (a) Schematic of electrochemical etching mechanism of Ti_2AlC in the presence of HCl solution. SEM images of MXenes obtained by different etching ways. (b) Sample 5 days-sediment obtained by electrochemical etching. (c) LiF + HCl etched MXene. [137]. Copyright 2017. Royal Society of Chemistry.

Electrochemical etching is more likely to occur on the surface of the material. In order to defeat the limitation of only etching on the surface, cations are easily inserted into the etched MXene, resulting in the expanded interlayer spacing and the following electrolyte ions diffusion. Feng et al. [138] used a composed of 0.2 mol tetramethylammonium hydroxide ($\text{TMA}\cdot\text{OH}$) ($\text{pH} > 9$) and 1 mol NH_4Cl as the electrolyte, and etched $\text{Ti}_3\text{C}_2\text{T}_x$ by a fluorine-free electrochemical method. The etching principle is illustrated in Fig. 14a. Furthermore, density-functional theory calculation was employed to investigate the etching mechanism. And electron localization function is illustrated in Fig. 14b. The contact of Cl^- begins from the exposed edge, and Cl^- makes the removal of Al rapid, when Ti_3AlC_2 is positively charged. The etching of Al atoms leads to the

formation of AlCl_3 and the exposure of Ti atoms at the edges. NH_4OH is inserted to open the MXene sheet. The opening is in favor of the further penetration of NH_4OH and Cl^- and promotes the efficiency of the etching reaction.

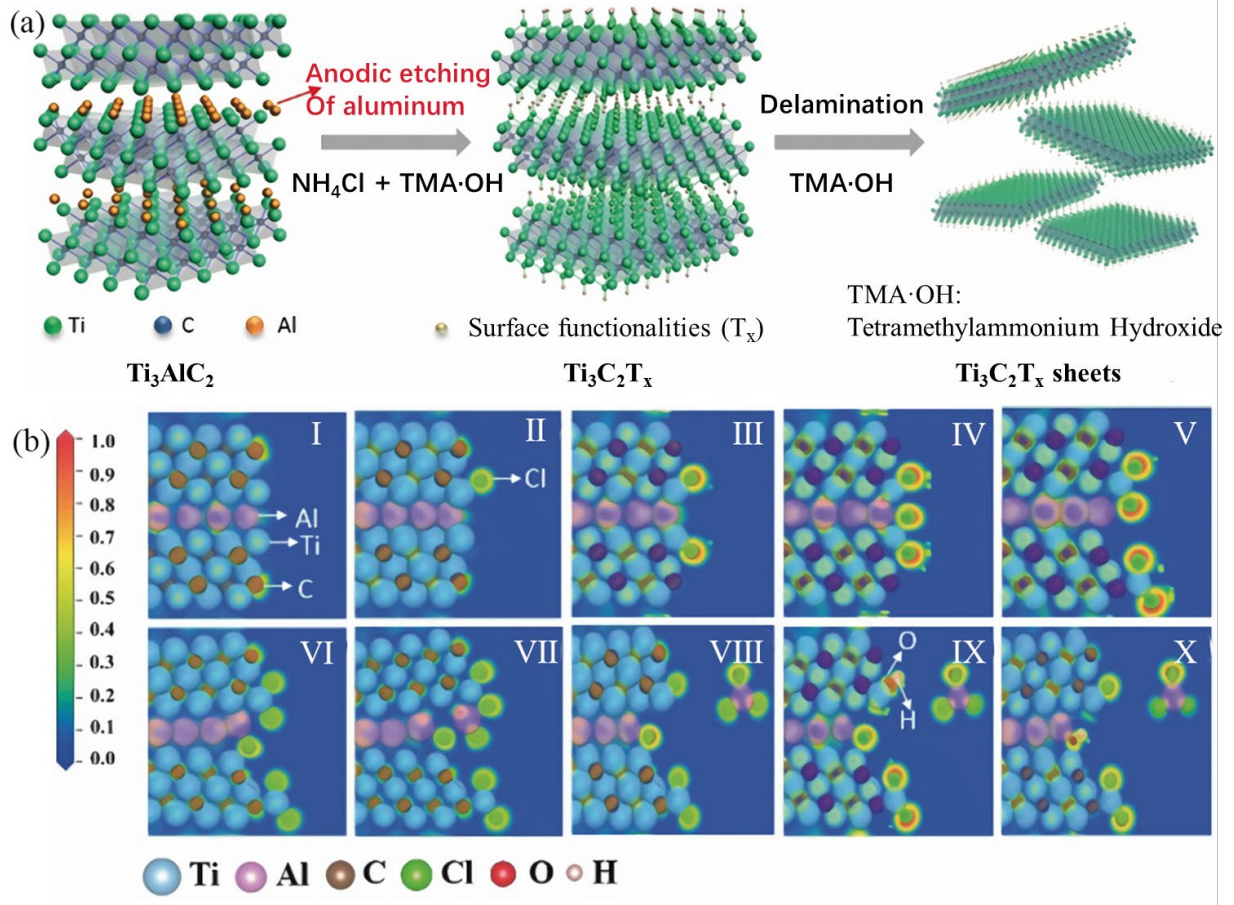
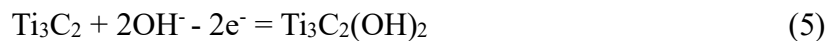
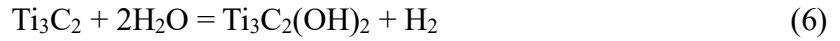


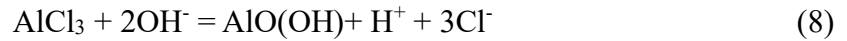
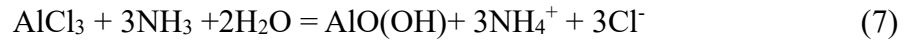
Fig. 14 (a) Schematic illustration for bulk Ti_3AlC_2 etching and delamination via using a binary aqueous electrolyte. (b) Electron localization function plots of (I) pristine and (II-X) etched Ti_3AlC_2 in the presence of 1-7 chloride anions, respectively [138]. Copyright 2018. Wiley-VCH.

At the same time, possible reaction equations are proposed:





Since the aluminum etching and the ammonium ions intercalation occur at the same time, the following reaction can be reasonably obtained.



3.1.4 Others

Some unique etching methods have been developed for different MAX phases, including the introduction of specific surface terminations after etching. For example, in the etching of Ti_4AlN_3 , due to the relatively high bonding strength of Al atoms and the poor stability of Ti_4N_3 , HF etching and in-situ etching cannot be used, because the etched Ti_4N_3 cannot exist stably. Gogotsi et al. [43] first used molten fluoride salt (59% KF, 29% LiF, 12% NaF) to etch in an argon atmosphere at 550 °C, and used tetrabutylammonium hydroxide (TBAOH) as an intercalant. After ultrasonic dispersion, $\text{Ti}_4\text{N}_3\text{T}_x$ was successfully etched (Fig. 15c).

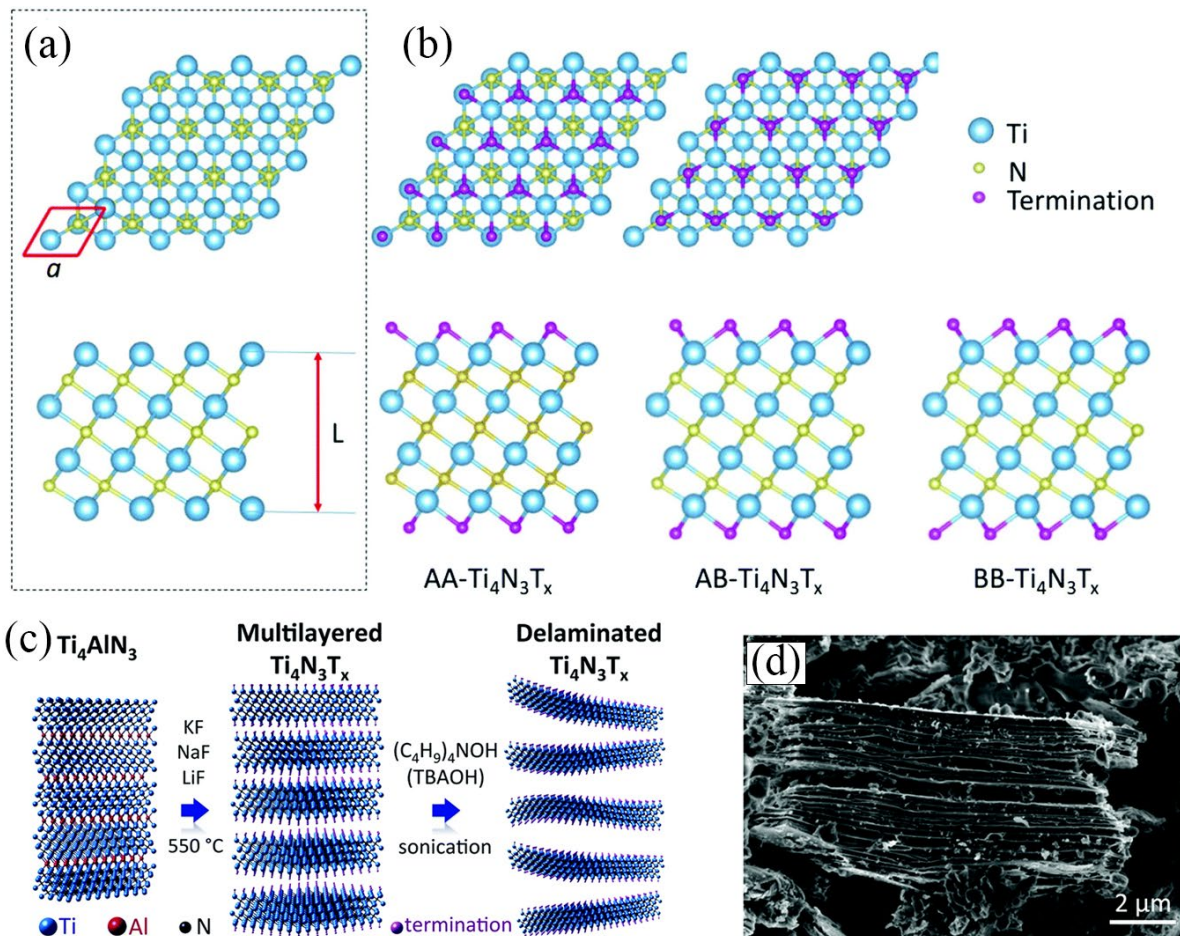


Fig. 15 (a) Top and side views of Ti_4N_3 monolayers crystal structure. (b) With respect to the single-sided terminations, hollow site of surface Ti and atop site of carbon separately denoted as A and B. As for double-sided terminations, the configurations denoted as AA, AB, and BB- $Ti_4N_3T_x$. (c) Schematic illustration and (d) SEM image of $Ti_4N_3T_x$ synthesis via molten salt treatment. [43] Copyright 2016. Royal Society of Chemistry.

Huang et al. [139] proposed a displacement reaction between phase A and the late transition-metal halides. At 550 °C in the presence of Ar gas, MXene with only Cl^- end groups were obtained by heat treatment. The principle is shown in Fig. 16a, where the weak bond Al atoms are effortlessly becoming into Al^{3+} through redox reaction and further combine with Cl^- to form $AlCl_3$. The formed $AlCl_3$ will evaporate rapidly at the reaction temperature. The Zn generated in situ

replaces the Al site to generate Ti_3ZnC_2 . Zn^{2+} cation can be as a very strong electron acceptor. The presence of excess molten ZnCl_2 would react with Zn to obtain low-valent zinc cations (Zn^+ , Zn_2^{2+}). Hence, the Zn atoms in Ti_3ZnC_2 are effortlessly extracted. Cl^- spontaneously inserts into a-site and combines with Ti_3C_2 at the specific site to form more stable chlorine-containing end groups MXenes (for instance $\text{Ti}_3\text{C}_2\text{Cl}_2$ and Ti_2CCl_2). Fig. 16e is the SEM image of the unetched Ti_3ZnC_2 and the Fig. 16d is atomic positions of the High-resolution (HR)-STEM image. Correspondingly, Fig. 16b, c are the SEM image after etching, and the atomic position of the SEM image. The -Cl end group MXene obtained by non-fluorine chemical methods is more stable than the -F end group MXene. It is a very potential method that may be used as a general method for other MXenes.

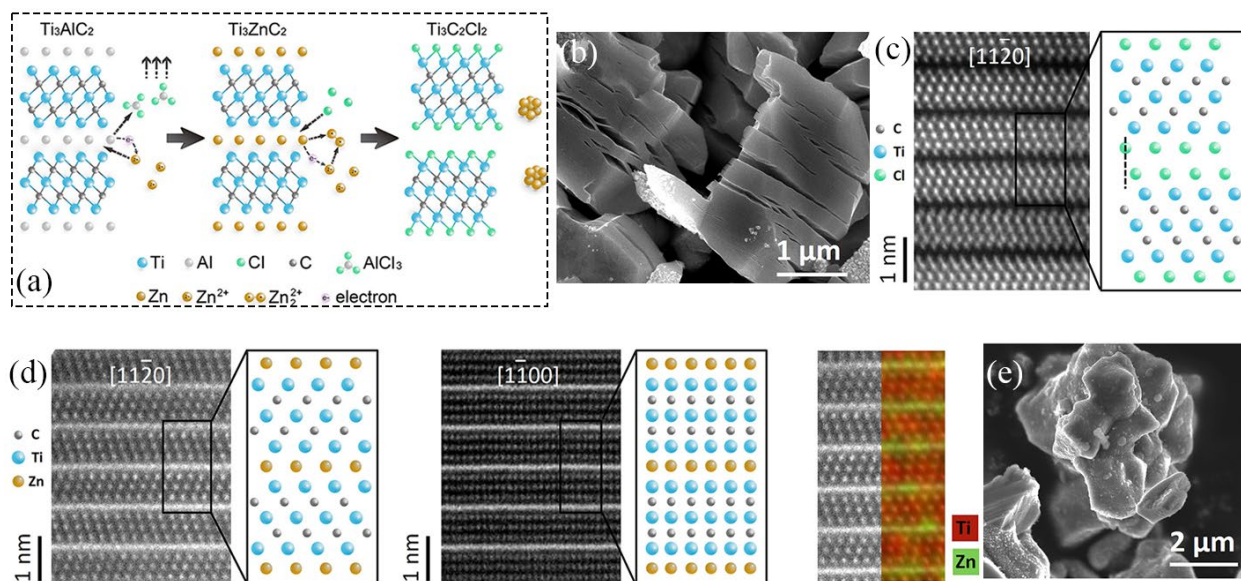


Fig. 16 (a) Schematic diagram of the $\text{Ti}_3\text{C}_2\text{Cl}_2$ preparation through molten salt ZnCl_2 treating Ti_3AlC_2 at 550 °C with Ar. (b) SEM image of as-reacted $\text{Ti}_3\text{C}_2\text{Cl}_2$. (c) HR-STEM image of $\text{Ti}_3\text{C}_2\text{Cl}_2$ atomic positions. (d) HR-STEM image of Ti_3ZnC_2 at from different orientations. (f) HR-STEM and the related EDS map and (e) SEM image of Ti_3ZnC_2 [139]. Copyright 2019. American Chemical Society.

3.2 Synthesis methods of CPs

3.2.1 Chemical method

Chemical oxidation is a method in which oxidants are used to cause monomers to lose electrons to undergo oxidative polymerization. Through experimental research, Hideki Shirakawa et al. [140] found that semi-CPs trans-polyacetylene film, exposed to chlorine, bromine, and iodine vapor, the polyacetylene film reacts with halogen, and the conductivity increases significantly. Even in the presence of iodine, the conductivity increases by more than seven orders of magnitude, some of which have very high conductivity at room temperature. High-conductivity film-like polyacetylene was synthesized for the first time, opening a new research direction on CPs in polymers.

Gospodinova et al. [141] first tried to use the electrochemical potential value of the system to express the polymerization reaction conditions and determine the basic steps of the polymerization process. Furthermore, it is proposed that aniline's oxidation polymerization belongs to a cationic radical polymerization mechanism. It is believed that the oxidation potential of aniline is much higher than that of dimers, and the oxidation of aniline monomers to form dimers is the control step of the polymerization reaction. After the dimer is formed, it is immediately oxidized to cationic radicals and further oxidative dehydrogenation aromatization to form a trimer. In this way, the electrophilic substitution-aromatization process can be repeated to continue the chain growth. This polymerization mechanism is currently the most accepted.

The most common synthesis method of PANI is to add a certain oxidant, such as ammonium

persulfate (APS), FeCl_3 , H_2O_2 , etc., in a high-concentration HCl solution under low-temperature water bath conditions. But Ma et al. [142] believed that the rapid polymerization in a strong acid environment (1.00 M HCl) may not supply sufficient solidification time for the formation of long-chain oligomers, making it challenging to generate multidimensional nanostructures with regular morphologies. It is proposed to use a low acidic environment (0.01 M HCl) to reduce the polymerization rate of aniline and prolong the reaction time. In order to achieve orderly self-assembly, a regular multi-dimensional PANI nanostructure was successfully prepared without stirring, including spherical, rose spherical, dendritic and so on. Among them, the spherical PANI is due to the hydrophilicity of the polyvinylpyrrolidone (PVP) molecule and the affinity for the aniline monomer. This reduces the surface tension between the solvent and the micelles, so that the PVP spherical micelles can exist stably. Hydrophobic aniline molecules can self-assemble uniformly in spherical micelles. The rosette-like PANI forms flake-like micelles due to the alternation of hydrophilic and hydrophobic parts. Because the PEG molecule contains abundant oxygen atoms, the sheet-like PANI is connected to each other through the form of hydrogen bonds. The formation of dendritic PANI may be explained by the lack of steric hindrance and hydrogen bond reduction in the sodium dodecyl sulfonate (SDS) molecule. The low steric hindrance effect increases the chance of contact, and the reduction of hydrogen bonds caused by -O deficiency reduces the possibility of PANI accumulation. The control of the shape is of great help for various applications in the later period, including the application of the direction of EMA.

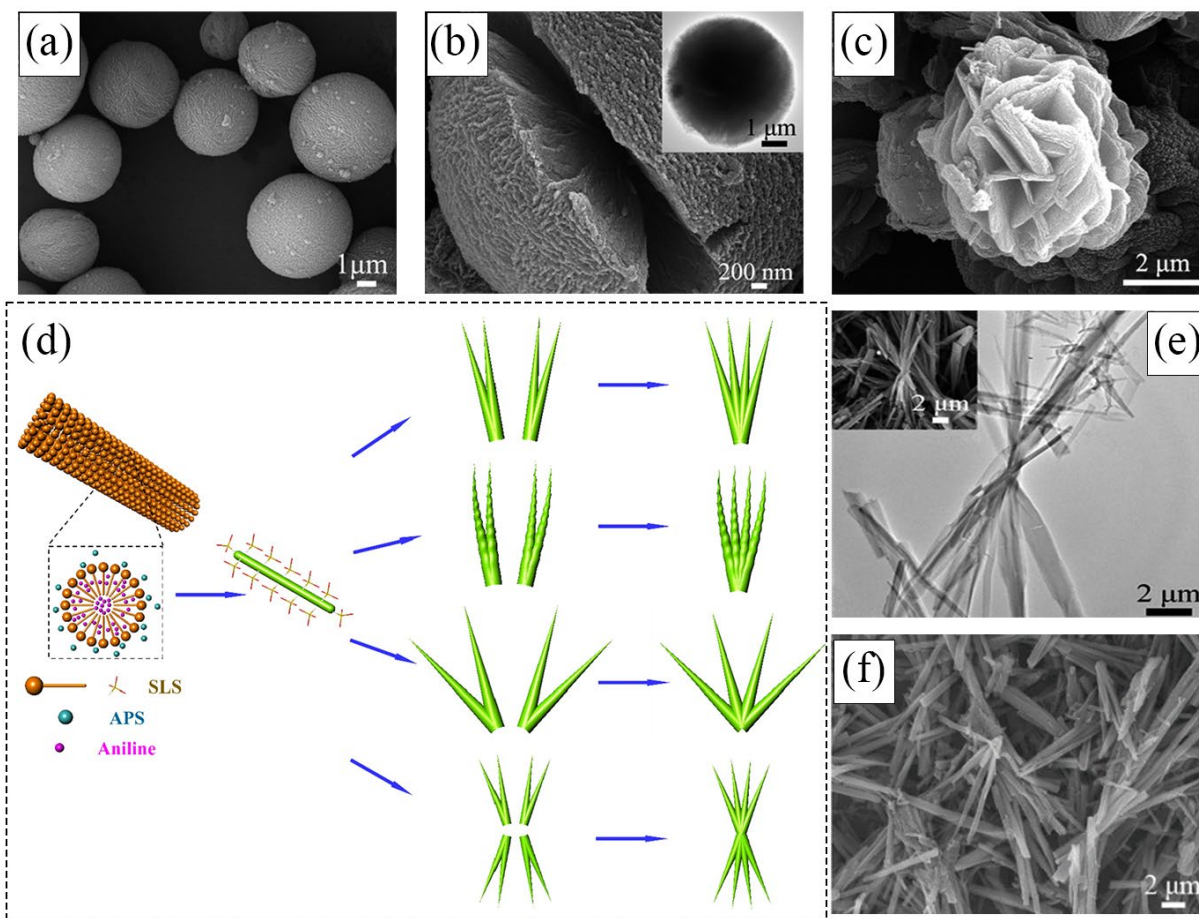


Fig. 17 SEM and TEM images of PANI (a and b) spheres, (c) roses and (e) dendrites [142]. Copyright 2017 Royal Society of Chemistry. (d) Formation mechanism of PANI dendrites with adding SLS micelles and (f) SEM image of branches of PANI dendrites [143]. Copyright 2019. Elsevier.

Ma et al. [143] synthesized dendritic PANI through a chemical method in HCl solution, using APS as an oxidant and sodium dodecyl sulfonate (SLS) as a soft template. Through this method, the biggest advantage is that the surfactant SLS molecules aggregate into micelles that can guide PANI nucleation and growth process. The aniline monomer is first nucleated and self-assembled with the help of SLS micelles. By studying the influence of different SLS concentration and HCl concentration on the morphology of the PANI dendrites produced, it is found that the induction

speed of aniline molecules is slow in a low HCl environment, and there is enough time to arrange the newly prepared PANI dendrites. However, under high concentration of HCl, excess H^+ leads to the formation of the curly PANI molecules, destroying the orderly arrangement. By controlling H^+ , solid PANI dendrites having high aspect ratio branches are synthesized. At the same time, in the presence of a high concentration of SLS, countless small and long micelles make the synthesized PANI have a chiral spiral structure [144]. PANI with this structure can form a reverse magnetic field through the Faraday effect, eddy current effect, etc. in the presence of alternating EMW. Through this kind of antenna structure and chiral PANI may have better performance in the absorbing direction in the future [145].

Generally, the structure of the CPs determines the conductivity of the polymer to a certain extent. The copolymerization of aniline monomer with other monomers can realize the preparation of the molecular structure of the polymer. Therefore, the conductivity can be effectively controlled by this synthesis method. Choi et al. [146] used SDS and aniline as monomers to generate surfactant aniline dodecyl sulfate (ADS). The water-in-oil emulsion system can be easily obtained under ultrasonic treatment with a mixture of Diphenylamine (DPA) and deionized water above its melting point. In the emulsion system, APS was used as an initiator to drop into the emulsion, and relatively monodispersed PDPA/PANI core/shell nanospheres were synthesized via oxidative polymerization. The reaction not only occurs on the surface of DPA droplets, but also proceeds at the interface between the dispersed phase and the continuous phase in the emulsification system. This conductivity adjustment method can be utilized in the design of the absorber. Adjustable

conductivity can be used to control the impedance matching of the absorber.

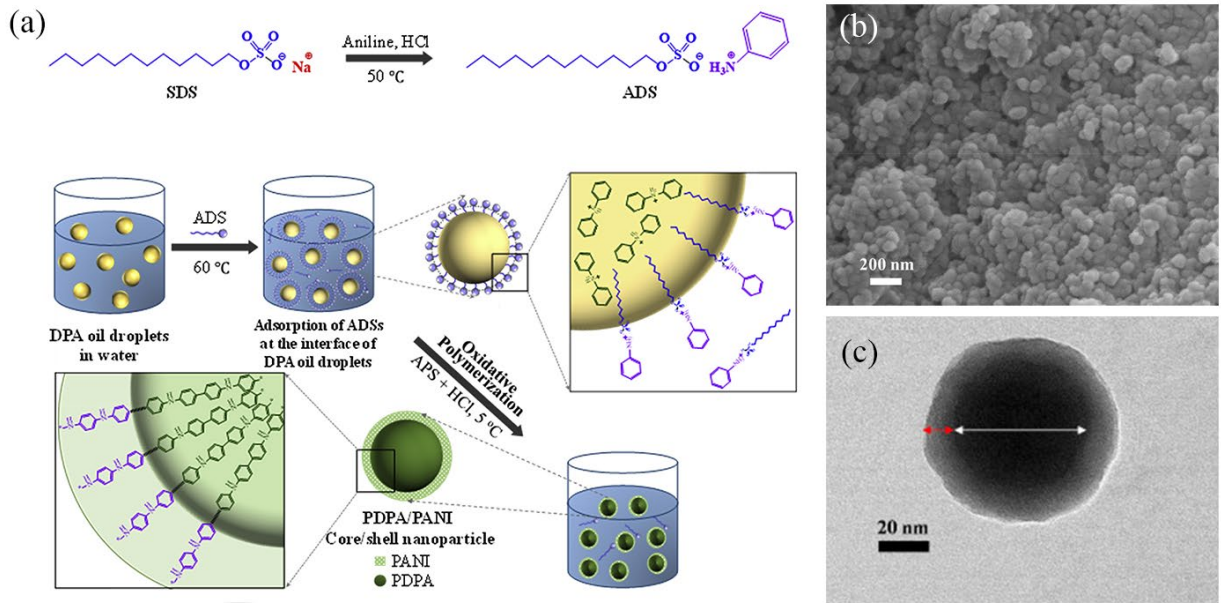


Fig. 18 Schematic illustration of the preparation of (a) ADS reactive surfactant and PDPA/PANI core/shell structure, (b) SEM and (c) TEM images of PDPA/PANI structure [146]. Copyright 2020. Elsevier.

Interfacial polymerization also belongs to the category of chemical oxidation. When the oxidizer solution is in addition to the monomer solution, polymerization can occur instantaneously in the interface phase of the two incompatible liquids. Zeng et al. [147] synthesized PANI by interfacial polymerization, in which aniline molecules were dispersed in carbon tetrachloride (CCl_4) as the organic phase, and the oxidant dopant was dissolved in an acidic aqueous solution as the water phase. With APS, APS/ FeCl_3 and APS/ $\text{K}_2\text{Cr}_2\text{O}_7$ as oxidants, respectively, three types of PANI nanostructures were prepared. And the prepared PANI structures could be easily controlled via adjusting the content of oxidant. The SEM figures of Fig. 19c-e are the PANI with three different oxidants. Based on the preparation mechanism, uniform nucleation conditions are

conducive to the formation of nanofibers, and heterogeneous nucleation conditions tend to form regular morphologies. Including regular nanofibers formed by APS/FeCl₃ as an oxidizing agent, and regular flower spheres formed by APS/K₂Cr₂O₇. By simply changing the type of the second oxidant, polymers with different microscopic morphologies can be easily obtained.

Hamlaoui et al. [148] used aniline as the monomer to be dispersed in the organic phase chloroform, APS as the oxidant, as well as malic acid (MA) as the dopant, and dissolved in distilled water in the water phase. Interfacial polymerization is achieved in the two-phase organic and aqueous phases. Fig. 19b reveals the potential doping sites between the protonated chains of PANI and MA, and the reaction process. Fig. 19a is a schematic diagram of interface aggregation.

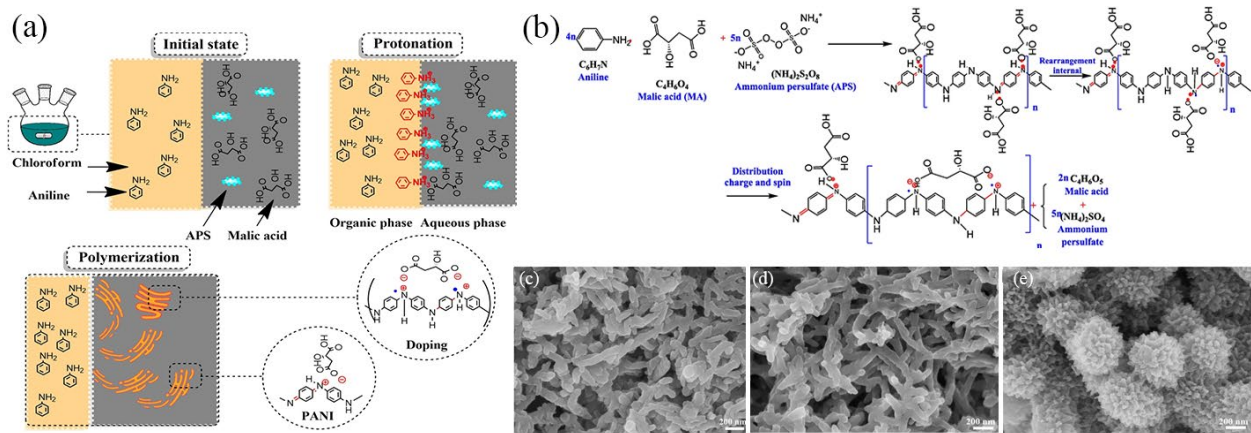


Fig. 19 (a) Diagram illustrating interfacial polymerization, (b) Diagram of the doping mechanism of PANI by malic acid [148]. Copyright © 2020, Springer-Verlag GmbH Germany. The SEM images of (c) APS, (d) APS/FeCl₃ and (e) APS/K₂Cr₂O₇ [147]. Copyright 2015 Chinese Materials Research Society.

Photochemical polymerization is a polymerization method initiated by light in the presence of a photosensitizer. According to the different modes of light action, it can be divided into

photocatalytic polymerization and self-polymerization of monomer molecules caused by photoexcitation. Azevedo et al. [149] found through research that there is no need for the presence of oxidants and the induction of Au electrodes with voltage [150]. In a silver nitrate solution containing nitric acid, photons in the UV or visible light region are sufficient to cause the polymerization of aniline. The morphology of the synthesized PANI is closely related to the excitation wavelength. The morphology of the polymer synthesized by ultraviolet light is spherical (Fig. 20b), and the morphology of the polymer synthesized by visible light is fibrous (Fig. 20c). The reaction mechanism can be explained by the equation (Fig. 20a).

The photopolymerization of PPy is only observed in chlorinated solvents for example chloroform or dichloromethane. But with regard to other solvents, such as and tetrahydrofuran, toluene, and ethyl acetate, photo-initiated polymerization will not occur. Besides, pyrrole will not polymerize when exposed to visible light. It needs ultraviolet light to polymerize. The currently generally accepted synthesis mechanism is as following:



There are some green polymerizations of CPs, among which polymerizations combine light-induced and chemical oxidizing agents. Green oxidant H_2O_2 is employed to initiate polymerization of pyrrole, which can effectively avoid metal oxidants remaining in the resulting polymer. However, the reaction efficiency is poor, and the corresponding preparation mechanism is not precise. To overcome the low reaction efficiency, Shao et al. [151] successfully prepared uniform

PPy nanoparticles in the presence of PVP under ultraviolet light irradiation. Furthermore, it is proved that ultraviolet radiation promotes H_2O_2 decomposition into hydroxyl radicals, which directly induce the polymerization occurrence. And the whole process of $h\nu$ -initiated polymerization is given by the following Fig. 20 d.

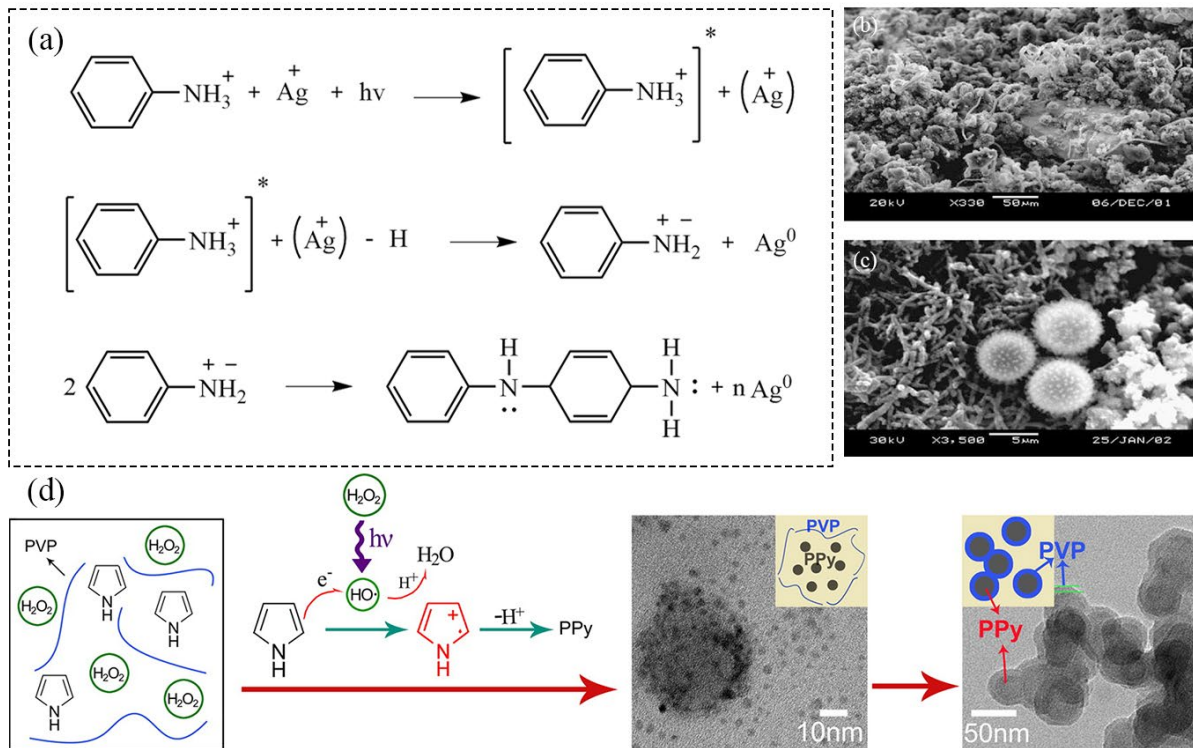


Fig. 20 (a) Photoinitiated polymerization of PANI in the presence of Ag^+ , SEM of PANI composite by (b) UV synthesis, (c) visible light synthesis [149]. Copyright 2003, Elsevier. (d) H_2O_2 -induced synthesis of PPy nanoparticles in the presence of UV irradiation with adding PVP [151]. Copyright 2015, American Chemical Society.

Chemical vapor deposition refers to a method in which chemical gas or steam reacts on the surface of a substrate to synthesize coatings or nanomaterial. It is a chemical oxidation method

used to produce solid materials with high purity and good performance. During the chemical deposition process, the base material is covered by the oxidant and placed in a heating chamber with monomer. When the temperature is higher than the melting point of the monomer, the polymerization reaction occurs on the surface of the matrix material [152]. It can be recognized that through chemical vapor deposition (CVD), a thin CPs coating can be co-deposited on almost any substrate through a stepwise polymerization process of monomers. The thickness, uniformity and morphology of the polymer film deposited by CVD rely on the kinds of doping or oxidant, the surface nature of the base materials, the monomer concentration, and the temperature of the sample.

Hu et al. [153] used a CVD method to coat a PPy film on the surface of MnO₂ nanowires on 1D CF loaded with MnO₂. Among them, ethanol is used as solvent, FeCl₃ is used as oxidant, and it is dried at 80 °C in a vacuum chamber. When the pressure of the vacuum chamber drops to 0.1 atm, the pyrrole monomer is converted into gas. The PPy shell is uniformly formed outside the MnO₂. The change from Fig. 21c-g shows that the PPy is successfully loaded on the substrate by the CVD method. At the same time, in another work, the CVD method was also used to deposit PPy nano-film on the surface of mesoporous MnO₂ uniformly to fabricate a hierarchical structure [154].

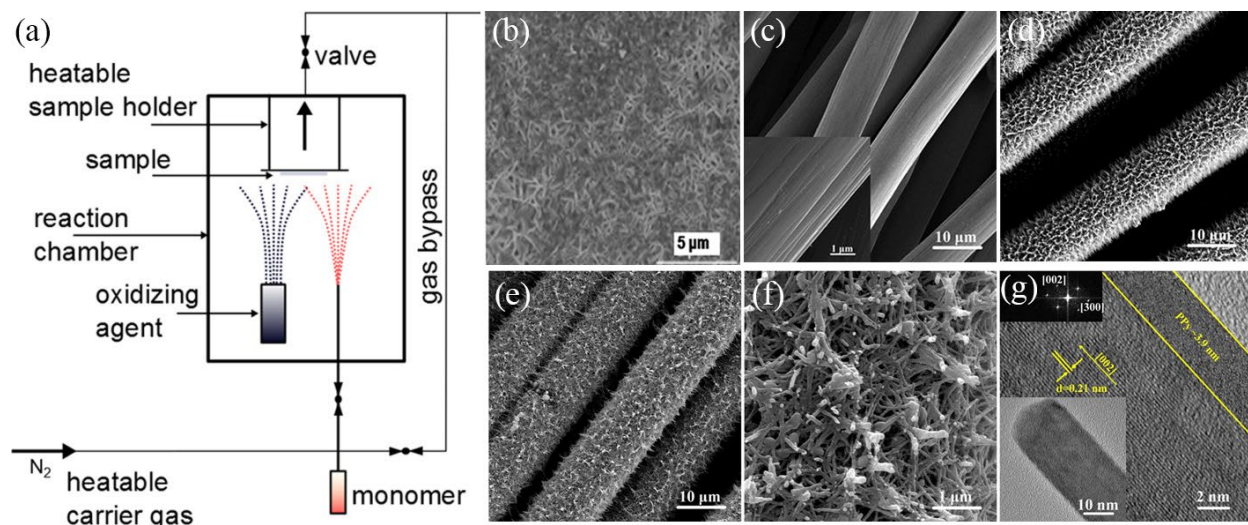


Fig. 21 Schematic CVD diagram. (b) SEM image of a pc-ZnO surface coated with PPy [155]. Copyright 2016 Wiley Periodicals. SEM images of (c) pure CF, (d) MnO₂@CF, and (e, f) PPy@MnO₂@CF, (g) HRTEM image and SAED patterns of PPy@MnO₂@CF [153]. Copyright 2019. Elsevier.

Castro-Carranza et al. [155] used an oxidative chemical vapor deposition method to deposit p-type PPy film on glass as well as n-type polycrystalline ZnO using different amounts of FeCl₃ as the oxidant to form a hybrid heterojunction. Fig. 21a shows a schematic diagram of chemical vapor deposition. This process is carried out at 250 °C, which is the best temperature for the sublimation (29.2%) of oxidant. Fig. 21b is the SEM image of PPy after vapor deposition corresponding to different FeCl₃ of 0.3g showing the PPy layer with more fibrous. Trujillo et al. [156] successfully deposited a PEDOT film on the template by using FeCl₃ as the oxidant on the basis of a 2D colloidal template. This colloidal template is formed by self-assembly of PS balls on vinyl-treated silicon wafers. The oxidizing agent converts these surface vinyl groups into free radical cations and combines with EDOT to covalently fix the PEDOT film on the silicon wafer.

In the presence of tetrahydrofuran (THF), sonicate sufficiently to completely remove this colloidal template. This method can effectively synthesize a CPs film.

3.2.2 Electrochemical polymerization

The electrochemical polymerization method to synthesize CPs is a new synthesis method that has developed rapidly in the past ten years. Electrochemical polymerization is widely used in the process of CPs polymerization because of its simple device, easy control of conditions, uniform polymer film thickness, and synchronization of polymerization and doping processes. Commonly used electrolysis methods include constant potential electrolysis, cyclic voltammetry scanning, and constant current electrolysis [157]. Electrochemical polymerization is an accurate and high-quality product because the deposition polymerization process is carried out in accordance with the electrostatic principle. The sample is deposited on the anode electrode by attracting opposite charges. This method can also prevent the expansion and contraction of chemicals when the charge diffuses from the electrode-electrolyte-electrode during the cycle.

Elkais et al. [158] electrochemically synthesized PANI in a dilute HCl solution containing aniline monomer on a graphite electrode. The electrochemical synthesis mechanism diagram is shown in Fig. 22 a. Liu et al. [159] prepared multilayer PANI-coated NiCo₂S₄ nanowires by electrochemical deposition on the basis of carbon fiber (NiCo₂S₄@CF) by hydrothermal method. Among them, an aqueous solution of sodium p-toluenesulfonate is used as the electrolyte. Fig. 22c-f are SEM images of CF, NiCo₂S₄/CF and NiCo₂S₄@PANI/CF, respectively. It can be observed in the figure that the electrochemically deposited PANI shell is uniformly loaded on the

substrate without changing its original morphology.

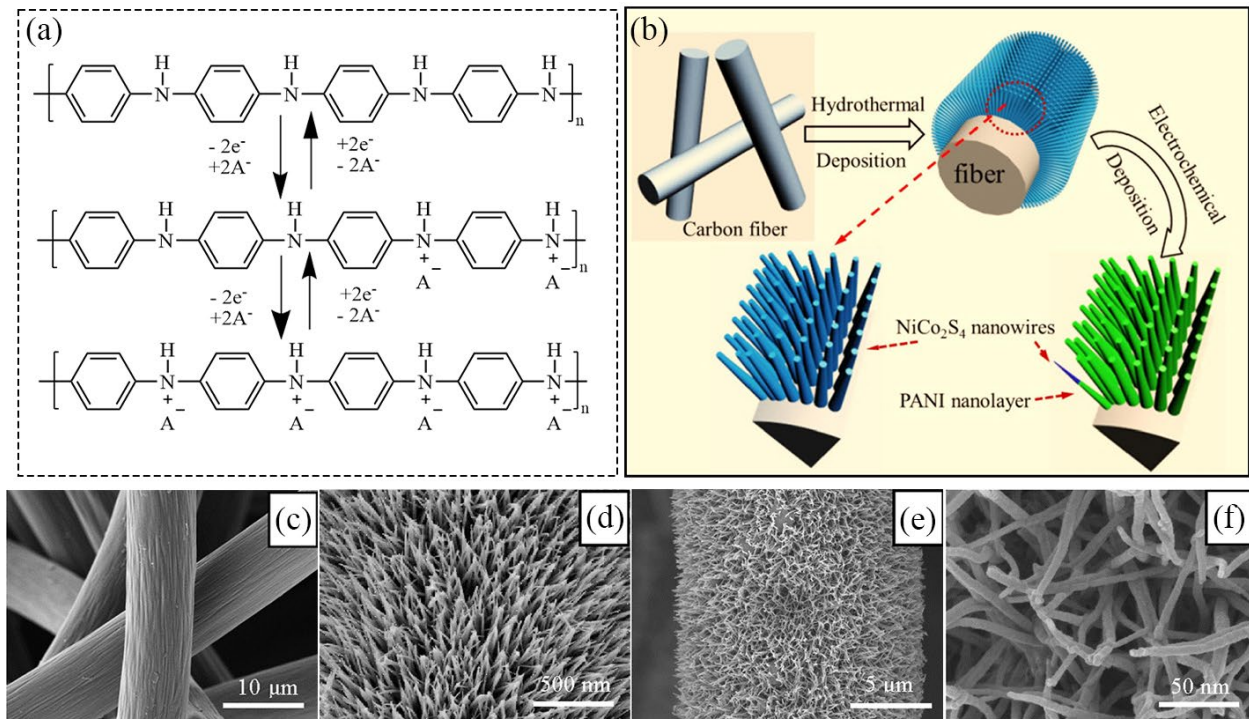


Fig. 22 Generalized scheme of the electrochemical reactions for the fundamental PANI oxidation forms [158]. Copyright 2010. Elsevier. FE-SEM image of (c) bare CF, (d) NiCo₂S₄/CF composites; (e, f) NiCo₂S₄@PANI/CF composites [159]. Copyright 2017. Elsevier.

Wang et al. [160] successfully introduced PANI on the carbon cloth loaded with MOF through the method of electrochemical deposition. The electrochemical deposition conditions are mild, and only need to cycle 75 cycles at room temperature and the voltage range of -0.2 to 1V. As shown in Fig. 23a, electrochemistry interweaves MOF crystals and CP PANI to increase the conductivity of MOF. This method can successfully introduce CPs on the organometallic framework and provides a feasible idea for compounding CPs in magnetic materials.

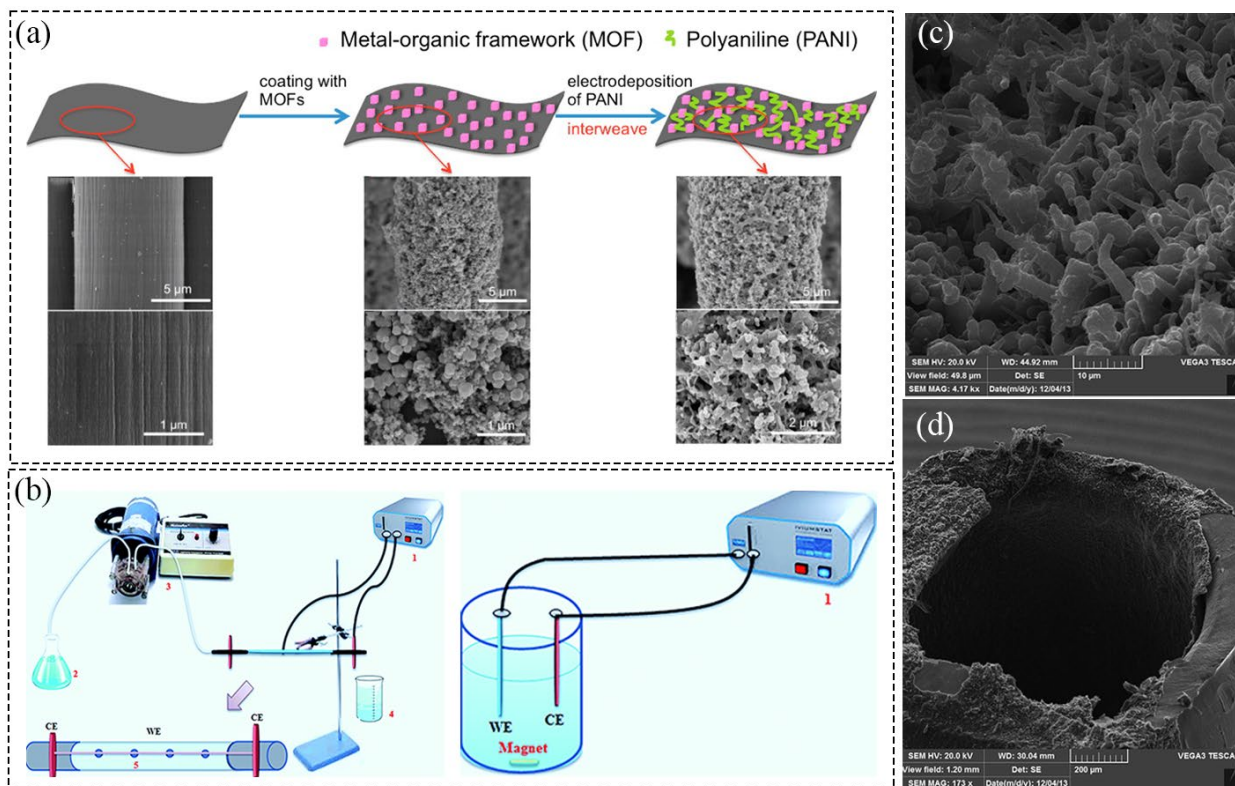


Fig. 23 (a) Schematic diagram showing the electrochemical deposition of PANI [160]. Copyright 2015, American Chemical Society. (b) Schematic diagram for PPy electropolymerization; SEM images of PPy-coated (c) tube and (d) wire [161]. Copyright 2014. RSC Publishing.

Chandler et al. [162] observed the release of protons during the oxidation of pyrrole and proposed the principle of electrochemical polymerization of PPy. Similar to the chemical oxidation method, a free radical cation is generated due to deprotonation, and the free radical attacks the neutral monomer unit. After re-oxidation of dimer radicals and loss of protons, this leads to chain growth. Ahmadi et al. [161] electrochemically polymerized PPy on the inner periphery of stainless-steel tubes and wires in the presence of perchlorate ion solution. In the oxidation process of PPy, PPy monomer is preferentially oxidized with a positive charge, so that the pyrrole monomer is

combined with the solution anion. Secondly, the PPy becomes neutralized and anions are being released. According to the relative position of the counter electrode and the geometry of substrates, various topographies are obtained. The SEM images are shown in Fig. 23 c, d, which represent PPy loaded on the substrate. During the process of synthesizing CPs, the control of different morphologies has great application potential for the direction of EMA.

Debiemme-Chouvy et al. [163] demonstrated that additional electrosynthesis in a classic pyrrole solution could change the diameter and length of oriented PPy nanowires. Furthermore, through excessive electro polymerization, it was found that the conductive PPy nanowire base was surrounded by a layer of peroxidized PPy (non-CPs), indicating that the PPy can undergo a second electrosynthesis. Fig. 24b shows the entire electropolymerization process with time. It can be observed that PPy forms compact layers after being over-oxidized (Fig. 24d). On this basis, PPy can further undergo a secondary electropolymerization to form a fibrous structure (Fig. 24c). Fig. 24a is a schematic diagram of PPy growth, where region a represents broadening and bc represents extension and broadening. With the control of the electropolymerization time, PPy with different aspect ratios can be obtained. According to the corresponding principles, dielectric materials can also be loaded to increase the ability of EMW absorption.

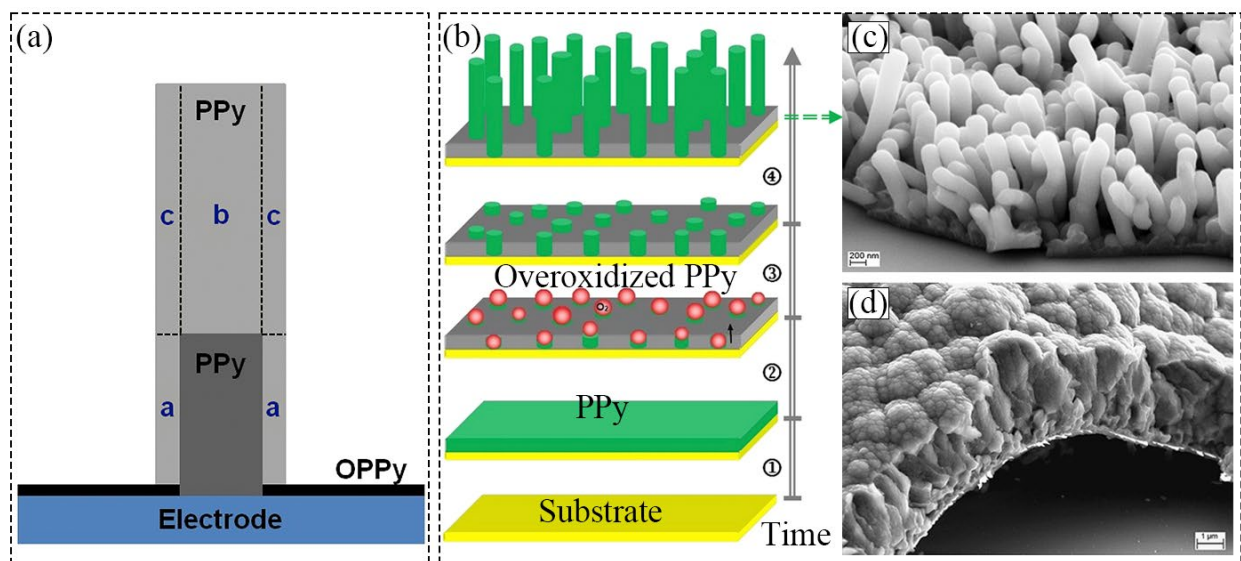


Fig. 24 (a) Schematic diagram of PPy in band growth; (b) the evolution of polymer deposition with anodic polarization time, the SEM images of (c) secondary electropolymerized and (d) over-oxidized PPy, respectively.

[163] Copyright © 2018 Elsevier.

3.3 Synthesis methods of MXene and CPs composites

3.3.1 Self-assembly method

As a thermodynamic metastable phase, the layered $Ti_3C_2T_x$ nanosheets are easily oxidized and decomposed by oxygen in the air or oxidizing solvents. At the same time, they have high cohesive energy and have a tendency to cluster. Hou et al. [164] simply mixed a $Ti_3C_2T_x$ colloidal solution and a PANI nanofibers suspension. And the electrostatic interaction can be formed between the former with negative charges and the latter with positive charges. By self-assembly, 1D/2D PANI/ $Ti_3C_2T_x$ nanocomposites are obtained. The PANI nanofibers are self-assembled and fixed to the layered $Ti_3C_2T_x$ nanosheets, making MXene stable and effectively relieving the oxidation and cluster accumulation of MXene [165].

Layer-by-layer (L-b-L) assembly is the alternate assembly of multiple systems to achieve a multilayer structure. Zhang et al. [166] alternately coated MXene nanosheets and silver nanowires on textiles treated with oxygen plasma and polyethyleneimine (PEI) to construct a highly conductive network. Inspired by this, Yu et al. [167, 168] used L-b-L self-assembly technology to alternately deposit PANI and MXene on activated carbon fiber cloth with positive charges. As shown in Fig. 25a, during the preparation process, PANI with +18.9 mV zeta potential is the prerequisite for obtaining good bonding strength. Besides, carbon fiber cloth treated with HNO₃ are full of positive charge, which helps improve the adhesion between it and MXene while removing surface impurities. Through the SEM image Fig. 25(c-f), it can be found that after 0, 1, 3, 5 L-b-L cycles, CF fabric are wrapped by the MXene and PANI layers. The overall structures of the fabric are still well maintained, and the spaces between the fibers are not filled, which allows a good conductive network environment to be retained. Through the element analysis Fig. 25b, it is also proved that MXene and PANI are uniformly generated on the CF. This shows that L-b-L is an effective compound method.

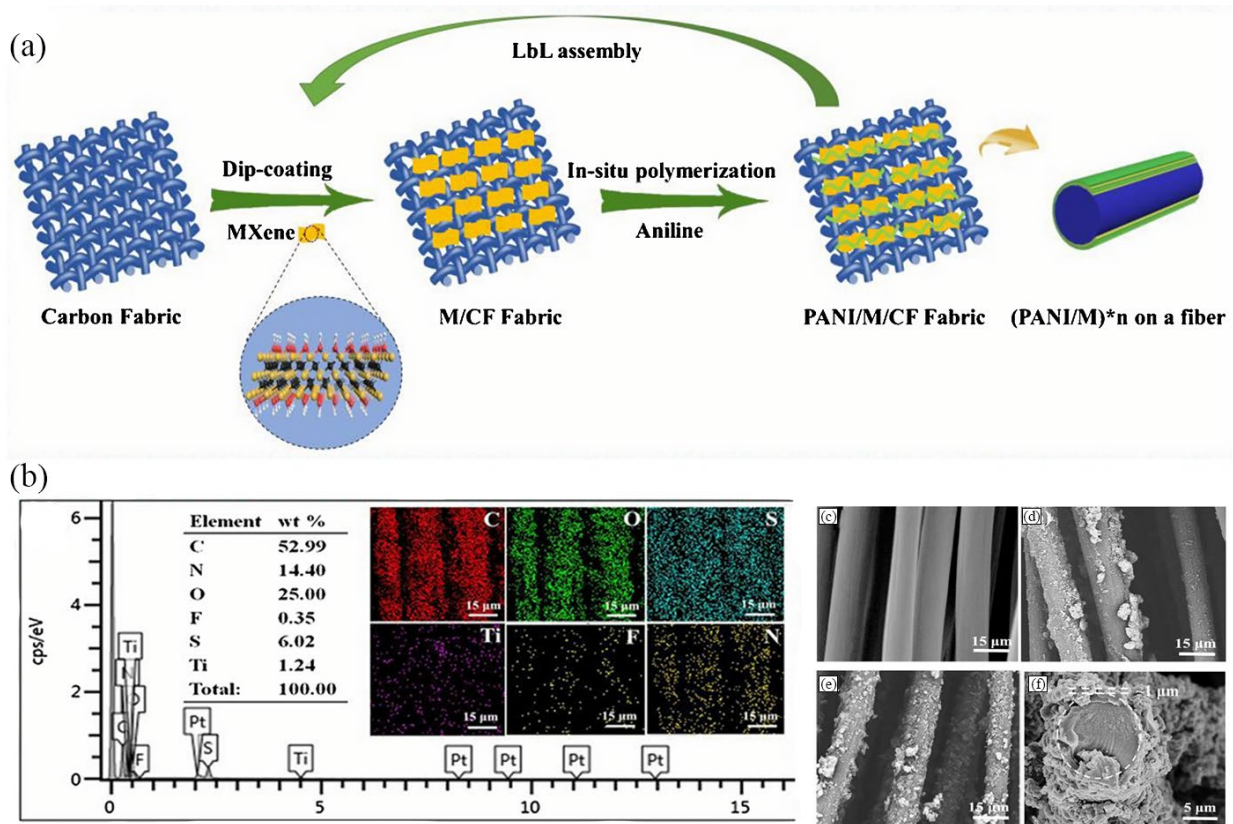


Fig. 25 (a) Schematic illustration for the manufacturing process of PANI/MXene/CF fabric. SEM images of (c) pristine CF fabric. (b) EDS spectra information of 5 time coated. (d) 1, (e) 3, (f) 5 time of PANI/MXene was coated on CF respectively [167]. Copyright 2020. Elsevier.

3.3.2 In-situ polymerization method

In-situ polymerization is a method in which reactive monomers and oxidants are added to the dispersed or continuous phase. Since the polymer monomer is soluble in the solvent containing the MXene sheet layer, the monomer is nucleated and grew on the periphery of the MXene. Finally, the composite structure is obtained. Lin et al. [169] used APS as the oxidant to chemically oxidatively polymerize the aniline monomer on the $Ti_3C_2T_x$ MXene layer under acidic conditions to prepare MXene/PANI composites. There are abundant functional groups (such as -OH, -O, etc.)

on the MXene sheet, used as nucleation sites for aniline monomers.

Wu et al. [170] proposed the in-situ polymerization of aniline on the ultra-thin periphery of MXene in malic acid or tartaric acid to construct hierarchical Ti_3C_2 nanosheet/PANI nanotube composites. The aniline monomer generates free radical aniline cations under the action of malic acid or tartaric acid and APS. Then the electrostatic interaction between the positive charge of the aniline cation and the negative charge of the Ti_3C_2 sheet. And through the residual oxygen-containing functional groups or van der Waals forces interacting with hydrogen bonds, PANI chains are inserted and fixed between the Ti_3C_2 nanosheets, and then in-situ growth occurs. Due to the interaction between Ti_3C_2 and PANI, the spontaneous accumulation of Ti_3C_2 is reduced, and the excessive self-growth of PANI is also restricted.

CPs usually undergo an oxidative polymerization process during chemical deposition, in which oxidants such as APS, $FeCl_3$, $K_2Cr_2O_7$, and $KMnO_4$ are used to initiate the polymerization process [171]. Gogotsi et al. [172] found that the $Ti_3C_2T_x$ layer serves as a reaction base for the orderly synthesis of PPy with the addition of an oxidant. The formation of hydrogen bonding may play a vital role in the orientation process. During the polymerization process, pyrrole oligomers tend to aggregate in disorder. But if there are hydrogen bonds formed between the substrate surfaces and PPy molecules, they will be arranged in an orderly manner. When using iodine, bromine, and chlorine to polymerize PPy, these halogens can play a dual role including oxidation and chemical polymerization simultaneously. Ratcliffe et al. [173] found that in the presence of strong acid, pyrrole is protonated at the C-3 position, and the protonated pyrrole monomer can be

polymerized with other pyrrole monomers. In an acidic environment, $\text{Ti}_3\text{C}_2\text{T}_x$ interacts with pyrrole to form a protonated molecule, reacting with unprotonated pyrrole to obtain a dimer and next form a polymer.

Afterwards, Gogotsi et al. [174] continued to realize the in-situ polymerization of 3,4-ethylenedioxythiophene (EDOT) on the periphery of 2D $\text{Ti}_3\text{C}_2\text{T}_x$ MXene in the absence of oxidants (Fig. 26b). Compared with PEDOT polymerized by conventional oxidants, d- $\text{Ti}_3\text{C}_2\text{T}_x$ has a lower degree of oxidation to EDOT, but it is sufficient to initiate polymer doping polymerization. For studying the polymerization mechanism, the density-functional theory calculation results on the polymerization of EDOT between MXene layers are shown in Fig. 26c. The binding energy of EDOT in three parallel directions is much lower than the binding energy in two perpendicular directions, indicating that EDOT is in the parallel adsorption on the $\text{Ti}_3\text{C}_2\text{O}_2$ surface is more favorable. The lowest energy is the PI type, and the lowest binding energy is -1.02 eV. Through Bader analysis shown in Fig. 26d, it is found that EDOT has -4.31 eV, which has a higher Fermi level than Ti_3C_2 -6.24 eV. Part of the p electrons of the former are transferred to the surface of the latter, and the rest is transferred to O-2p or C-2p orbitals. EDOT polymerization may be a result of the charge transfer. The mechanism without adding oxidant is still unclear.

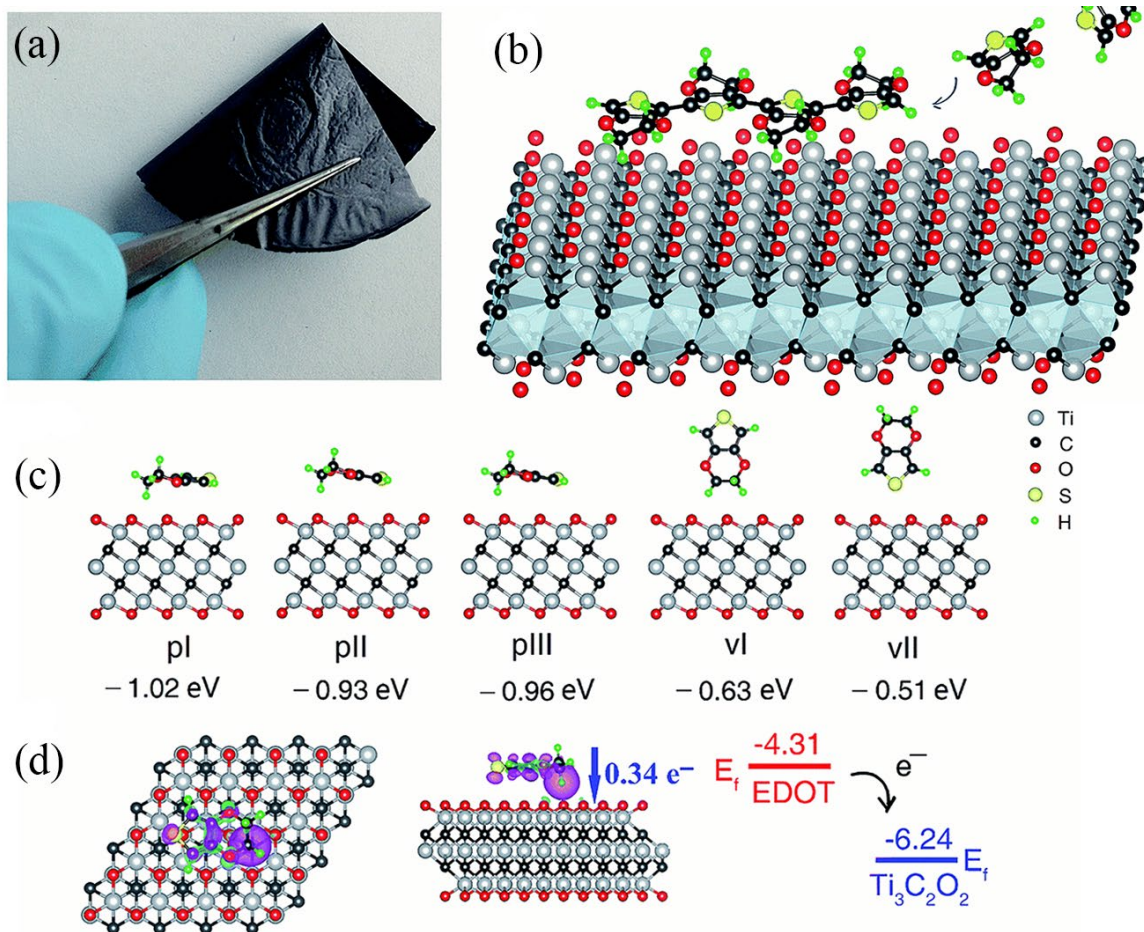


Fig. 26 (a) Freestanding and flexible film of MXene/PEDOT composite. (b) Schematic diagram of preparation of MXene/PEDOT composite. (c) Various adsorption orientations and binding energies of EDOT on the surface of $\text{Ti}_3\text{C}_2\text{O}_2$. (d) The difference in charge density and charge transfer for the most stable adsorption configuration (pI) and the violet and turquoise regions indicate depletion and accumulation of electrons, respectively [174].

Copyright 2017. Royal Society of Chemistry.

3.3.3 Electrospinning

In addition to the chemical as mentioned above synthesis, the composite product of CPs and MXene can also be obtained by the electrochemical method. Wu et al. [175] separately used Pt and FTO glass as the counter electrode and the working electrode shown in Fig. 27b. First, Ti_3C_2

was electrochemically deposited at 15 V for 2.0 min. PANI was electrochemically polymerized at 1.0 V. N-Ti₃C₂ and PANI were successively formed on the surface of FTO glass substrate through a two-step electrochemical reaction. In TEM image of Fig. 27c, one can see that PANI is deposited on MXene very uniformly. N-Ti₃C₂ can be explained as the introduction of amino tube energy groups on the Ti₃C₂ chip. As shown in Fig. 27a, first with the addition of organic base P-phenylenediamine and isoamyl nitrite, the latter can decompose to produce nitrite, providing nitroso cations, thereby launching an electrophilic attack on amino nitrogen. Then the active hydrogen, fluorine, and hydroxyl on Ti₃C₂ are replaced with nitrogen atoms to carry out amino functionalization. The amino group of N-Ti₃C₂ is used as an active site to bind to the amine nitrogen on the PANI chain. It can be used as an active site to bind to the amine nitrogen in the PANI chain to facilitate the aniline growth between the Ti₃C₂ layers and the periphery of the layer.

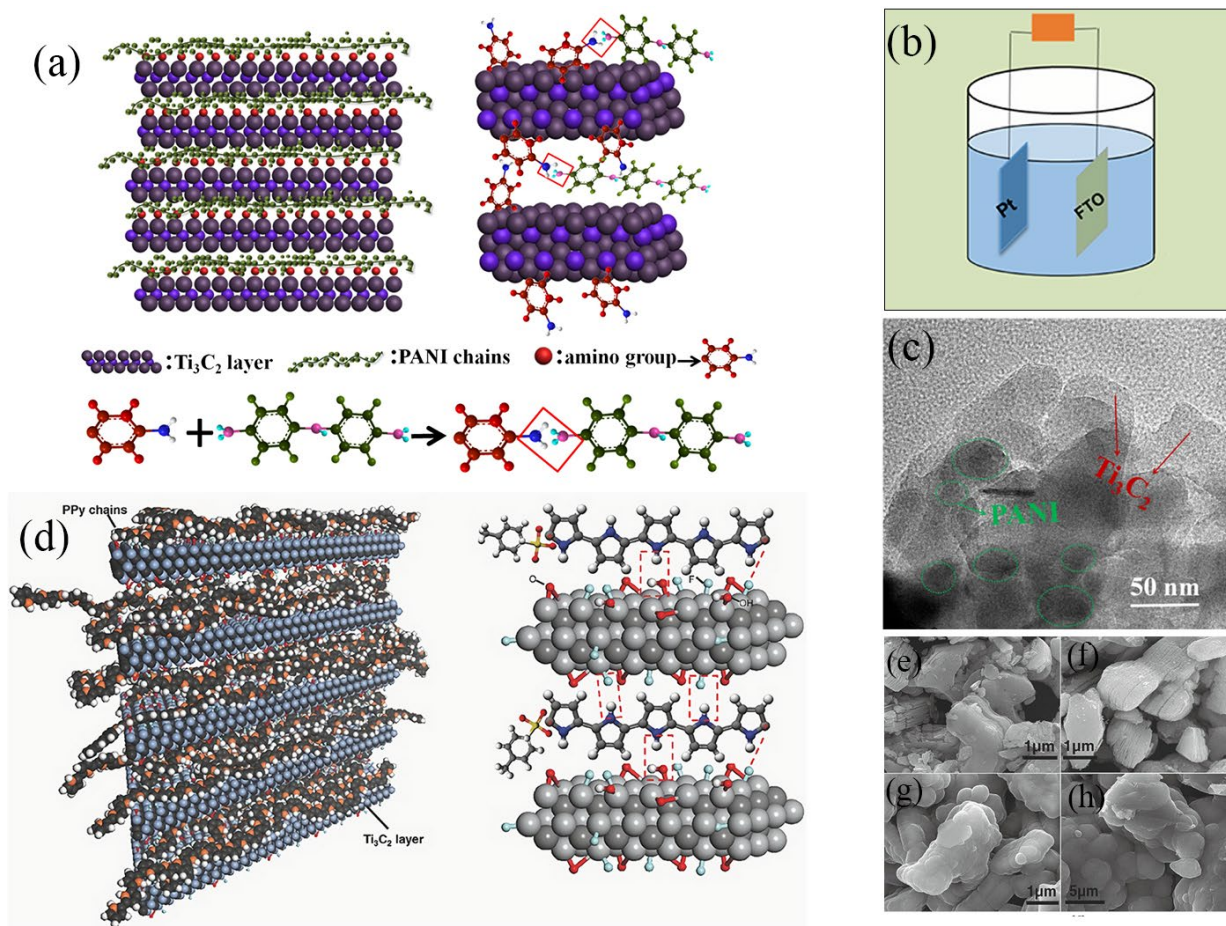


Fig. 27 (a) Schematic of intercalated PANI in the interlayers of N-Ti₃C₂. (b) Schematic diagram of electrochemical polymerization. (c) TEM images of N-Ti₃C₂/PANI [175]. Copyright 2019. Elsevier. (d) Schematic of intercalated PPy in the interlayers of l-Ti₃C₂. (e) SEM image of l-Ti₃C₂ particles on FTO by using electrophoretic deposition; SEM image of PPy for (f) 60, (g) 300, and (h) 600 s by using electrochemically polymerizing [176]. Copyright 2016. Wiley-VCH

Zhi et al. [176] firstly used the electrophoretic deposition method to prepare a uniform Ti₃C₂ film in the presence of 50 mL acetone and 15 mg iodine. And the schematic diagram is shown in Fig. 27d. Acetone and iodine are served as the stabilizer and the charge, respectively. Due to the weak interaction of PPy in the polymerization process, PPy was successfully inserted into the Ti₃C₂

sheet through electrochemical polymerization. It can be observed from Fig. 27e-h that PPy first fills the gaps in the MXene sheet, and then deposits and coats the MXene surface until it is completely wrapped.

Jian et al. [177] proposed preparing MXene/PPy composite membranes for the first time by co-electrodeposition. During the process, there are -F, -OH, or -O on the periphery of the 2D MXene nanosheets, which play a core role in polymerization. The ITO-coated glass is worked as a working electrode at 0.8 vs. (Ag/AgCl)/V, and the deposition time is from 300 s to 1800 s. The pyrrole monomer free radical cations ($\text{Py}^{\cdot+}$) will polymerize on the periphery of the 2D MXene nanosheets gradually to form a 3D carambola-like MXene/PPy composites.

4 Research progress of wave absorption performance

4.1 Electromagnetic absorption of MXene

Qing et al. [178] first used HF-etched Ti_3C_2 nanometers to test its absorbing properties. The structure of MXene is shown in the Fig. 28e. By measuring the complex permittivity, the inverse loss is calculated, and the result are shown in Fig. 28a, b. The study found that the ϵ' and ϵ'' values of Ti_3C_2 nanosheets are much higher than those of $\text{Ti}_3\text{Al}_2\text{C}_2$ at the same filling amount of 50 wt%. At the same time, it also shows the absorbing performance. Obviously shown in Fig. 28c, d, the $R_{L\min}$ of Ti_3C_2 nanosheets is lower than $\text{Ti}_3\text{Al}_2\text{C}_2$. At 1.4 mm, the $R_{L\min}$ value of the Ti_3C_2 nanosheet-filled composite material in the entire Ku-band is less than 11 dB, which means that Ti_3C_2 MXene can be used as absorbing increasing the absorbing bandwidth and reducing the thickness of the material.

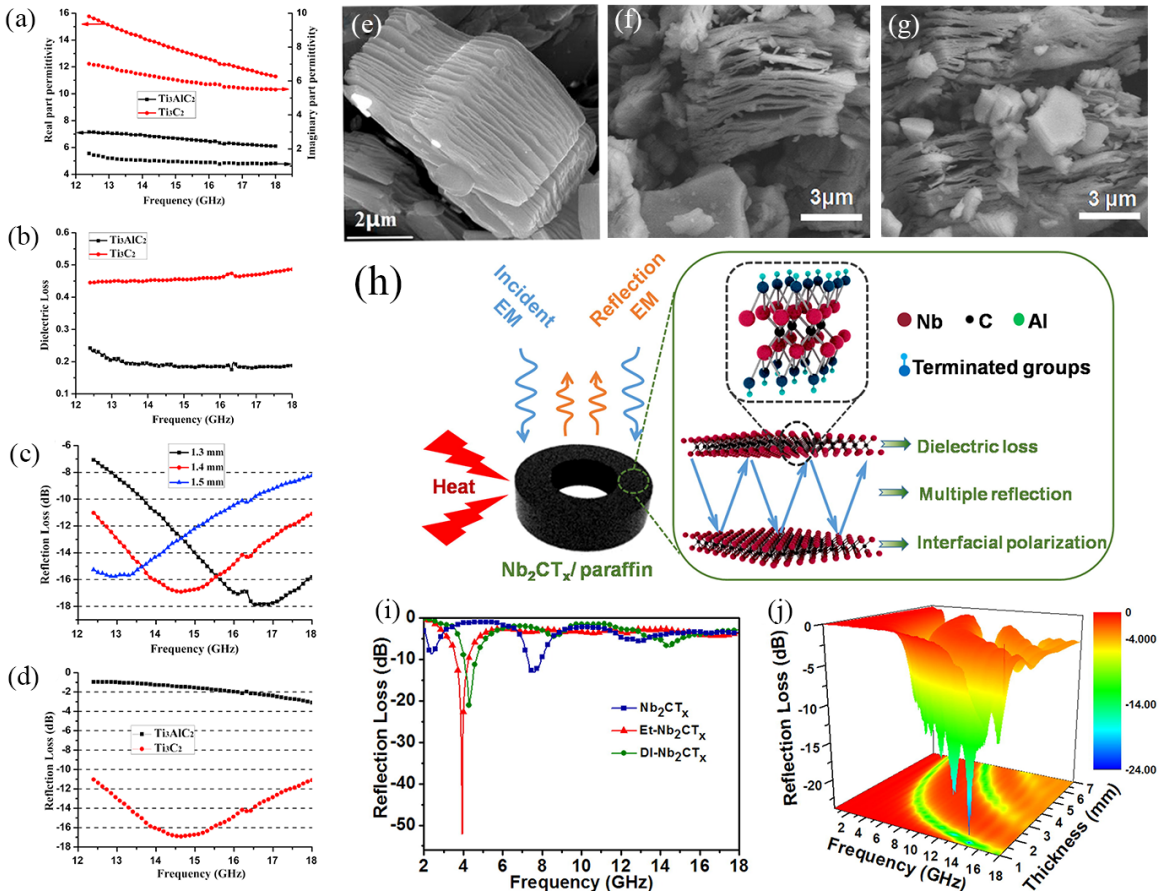


Fig. 28 (a) Complex permittivity and (b) dielectric loss of the 50 wt% Ti_3AlC_2 powders and Ti_3C_2 nanosheets filled epoxy composites. (c) Thickness dependence of the reflection loss in the Ku-band. (d) Comparison of the reflection loss at 1.4 mm thickness. (e) SEM image of the structure by HF etching [178]. Copyright 2016, Elsevier. SEM images of (f) Et- Nb_2CT_x and (g) DI- Nb_2CT_x . (h) Scheme of the mechanism for EMW absorption performance of Nb_2CT_x nanosheets. (i) The frequency dependence of the reflection loss of Et- Nb_2CT_x /paraffin, DI- Nb_2CT_x /paraffin and Nb_2CT_x /paraffin with the thickness of 2.9 mm in 2.0-18.0 GHz. (j) 3D image of the reflection loss of Et- Nb_2CT_x /paraffin in 2.0-18.0 GHz. Copyright 2018, Elsevier.

Xu et al. [44] first tried to perform an EMW absorption test on Nb_2CT_x MXene etched by HF.

The EMW absorbing properties of Et- Nb_2CT_x (Fig. 28f) were treated with ethanol at 100 °C, DI-

Nb_2CT_x (Fig. 28g) treated with deionized water, and untreated Nb_2CT_x nanosheets. By the Fig. 28i, j, it is found that Et- Nb_2CT_x has the best absorbing performance and can reach -52.2 dB reflection loss at 93 GHz at a thickness of 2.90 mm. The main reason is that the intercalation effect of ethanol increases the interlayer spacing and brings more defects (such as oxygen-containing functional groups, etc.) on the initially defective MXene sheet. This makes the increase of Nb_2CT_x while bringing more polarization effects and opportunities for multiple reflections. However, the minimum R_L of Et- Nb_2CT_x and DI- Nb_2CT_x are concentrated in the 2.0-4.0 GHz, making it difficult for pure Nb_2CT_x MXene to be used as a broadband absorbing material.

Although these works have fully proved that Ti_3C_2 nanosheets have substantial potential in the preparation of thin layers and broadband EMW absorbing materials. However, the EMW absorbing material of pure $\text{Ti}_3\text{C}_2\text{T}_x$ MXene, due to its non-magnetism, only has the dielectric loss mechanism of EMW absorption without magnetic loss. At the same time, due to the higher dielectric constant, the impedance is not matched so that more EMW are reflected, which limits the further improvement of EMW absorption performance.

Li et al. [111] employed $\text{LiF} + \text{HCl}$ to obtain a conductive 2D Ti_2CT_x MXene with a natural sandwich structure through a simple chemical etching process and reported for the first time that MXene has EMI shielding performances in the X-band. The prepared MXene material exhibits an excellent performance of more than 70 dB in the case of only 0.8 mm. The dielectric constant of pure MXene $\text{Ti}_3\text{C}_2\text{T}_x$ is too high, which is not ideal for absorbing performance. It is more suitable as an EMI shielding material than an electromagnetic absorbing material [179]. However, it is

possible to reduce the dielectric constant and increase the magnetic permeability through composite magnetic materials to adjust the impedance to match. It is more likely to be used as a RAM.

There are many literatures reported about MXene composite zero-dimensional magnetic materials. Yue et al. [180] developed a simple hydrothermal method to prepare $\text{TiO}_2/\text{Ti}_3\text{C}_2\text{T}_x/\text{Fe}_3\text{O}_4$ nanocomposites. TiO_2 and Fe_3O_4 densely cover MXene nanosheets with an average particle size of about 4.9nm. Among them, $\text{Ti}_3\text{C}_2\text{T}_x$ thermal oxidation obtains a TiO_2 -based composite material, which provides dielectric loss of $\text{TiO}_2/\text{Ti}_3\text{C}_2\text{T}_x$, and then combines with magnetic Fe_3O_4 that contributes to the magnetic loss. Among these composite materials, 2D $\text{Ti}_3\text{C}_2\text{T}_x$ flakes not only serve as carriers for Fe_3O_4 and TiO_2 , but also provide lots of interfaces to promote carrier transfer, thereby promoting interface polarization. This makes it have good EMW absorption performance. As the mass ratio of $\text{Ti}_3\text{C}_2\text{T}_x/\text{Fe}_3\text{O}_4$ is 5:1, the composite displays 2.0 GHz absorbing frequency bandwidth below -10 dB in the situation of 1.9 mm thickness, and the maximum R_L value of -57.3 dB at 10.1 GHz.

Magnetic metals including Ni, Co, etc. of the absorption mechanism are shown in the Fig. 29a. Due to their high magnetic permeability and saturation, high temperature resistance, strong corrosion resistance as well as magnetic loss, have great application potential in the direction of EMA. Liu et al. [181] reported for the first time that $\text{Ti}_3\text{C}_2\text{T}_x$ MXene modified with Ni magnetic metal nanoparticles has excellent EMW absorption performance. Through SEM of MXene (Fig. 29e) and $\text{Ni}@\text{Ti}_3\text{C}_2\text{T}_x$ (Fig. 29f) and elemental analysis (Fig. 29g), the uniform composite of

MXene and metal particles is proved. As the thickness is 3 mm, the R_L of PVDF-based composites with 10 wt% Ni@Ti₃C₂T_x 8:1 can reach a minimum of -52.6 dB (Fig. 29d), and EAB can reach 3.7 GHz as shown in Fig. 29b, c, which means that 71% of the X-band can be covered. At the same time, the adjustment of the sample thickness can achieve the absorption of the entire X-band, and the best EAB can be as high as 6.1 GHz. And through the electronic holography technology Fig. 29h-i to verify the unevenness of the charge distribution, this unevenness helps to strengthen the loss mechanism such as polarization. This moderate and straightforward co-solvothermal method prepares a composite consisting of Ti₃C₂T_x nanosheets and Ni nanoparticles. In addition, this method can be used to prepare the composite with other magnetic metal nanoparticles to achieve efficient EMW absorption, such as Co and NiCo nanoparticles, etc.

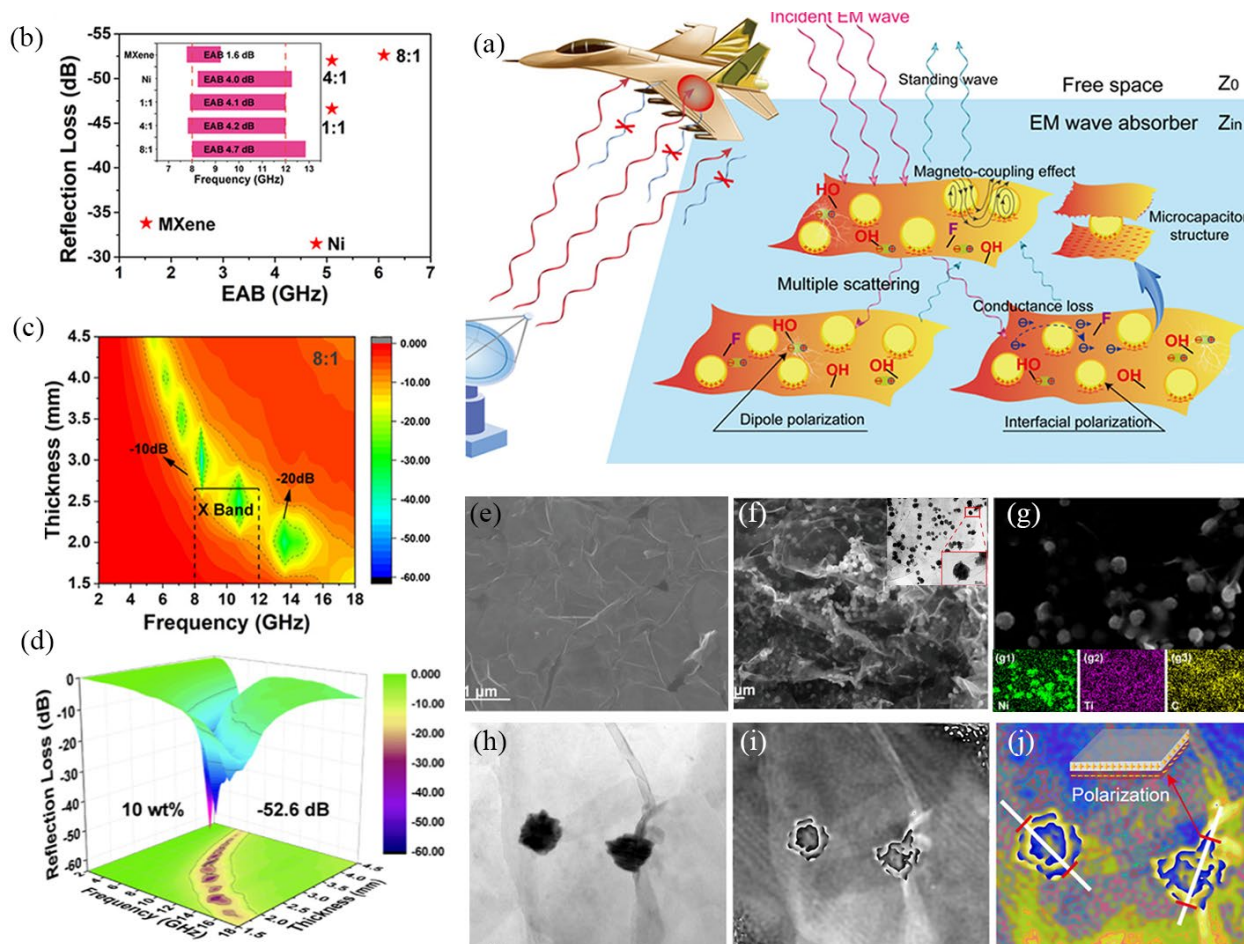


Fig. 29 (a) Schematic diagram of EMA of MXene and metal particle composite materials. (b) Statistical image of R_{Lmin} , optimal EAB and (inset) the EAB on X-band of all samples. (c) 2D plots of the EAB and (d) 3D plot of R_{Lmin} . SEM images of (e) $Ti_3C_2T_x$ nanosheets, (f) Ni@MXene 8:1. (g) SEM image and the related elemental mappings of Ni, Ti and C. (h) TEM images and (i, j) the off-axis electron holograms of Ni@MXene hybrid [181].

Copyright 2020. American Chemical Society.

Che et al. [182] designed a new type of positively charged $Ni(OH)_2$ and negatively charged accordion-like MXene composite material and fabricated a multilayer MXene/Ni material with adjustable electromagnetic performances via electrostatic self-assembly method. The minimum R_L reaches -50.5 dB at 5.5 GHz. Through the adjustment of the mass ratio of two components, the

maximum EAB is 5.28 GHz. The composite material is etched into an accordion shape due to MXene, and Ni nanoparticles are decorated in the multi-layer gap, effectively preventing MXene sheets' re-stacking. Magnetized MXene has more absorption mechanisms, such as conductive network (Fig. 30i), capacitor-like structure (Fig. 30j), magnetic loss (Fig. 30k) and polarization loss (Fig. 30l). Off-axis electron holograms can directly prove the magnetic loss. (Fig. 30a-f).

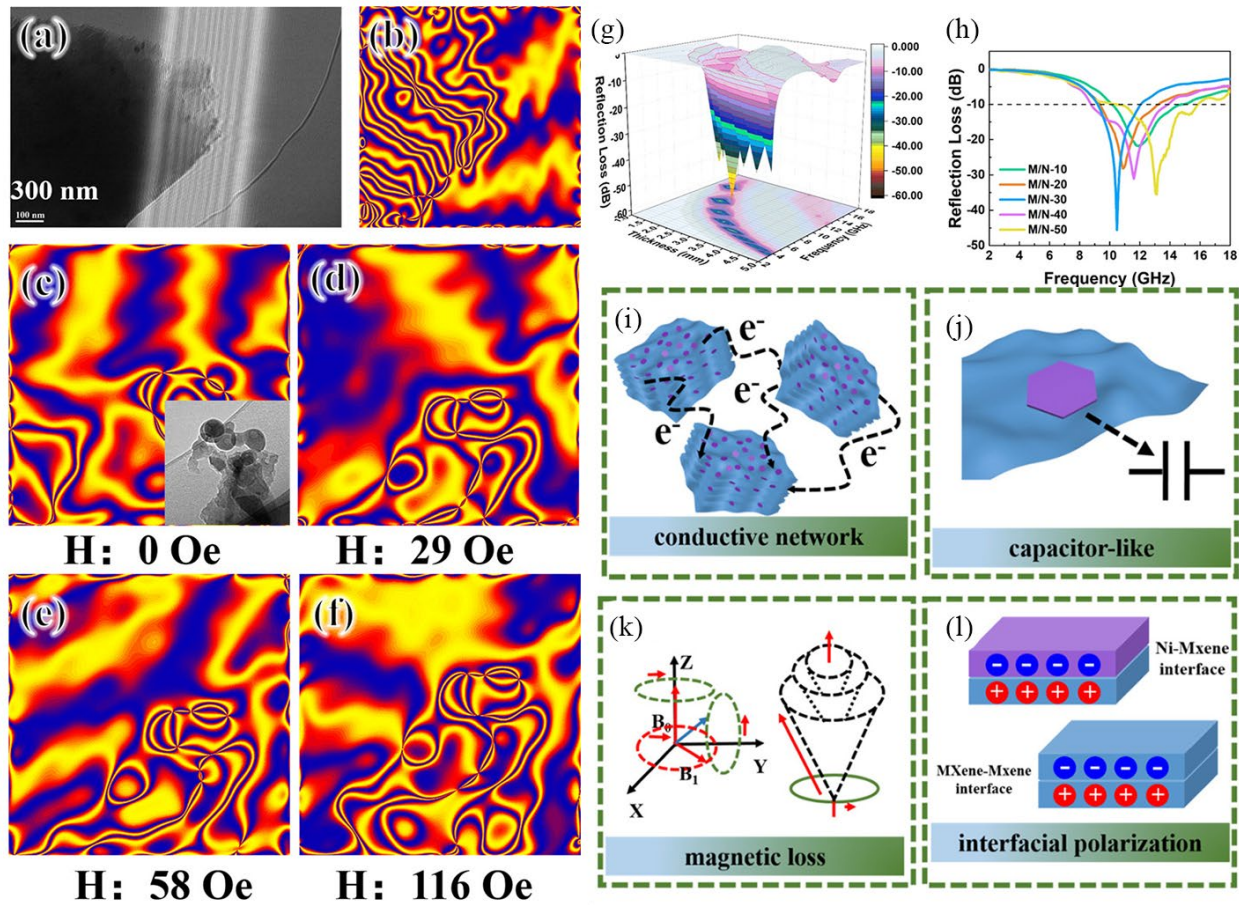


Fig. 30 Off-axis electron holograms of cutting sections (a), off-axis electron holograms at zero field, and the phase amplification of the holograms are 5 of M/N-30 composites (b); the evolution of the magnetic flux lines of M/N-30 composites at different magnetic fields and the phase amplification of the holograms are 10 (c-f)

[182]. Copyright 2019. American Chemical Society.

Through the magnetic induction line change, it can be explained that the magnetized MXene has an excellent dynamic magnetic response to the incident EMW. It changes dynamically under the action of a relatively low magnetic field of 0~29 Oe. This change is more evident under a relatively high electromagnetic field of 58 Oe and 100 Oe. Due to the existence of this magnetic induction line, the magnetic loss can also be brought about in non-material areas. The cooperation effect of magnetic and dielectric losses increases EM loss, thereby realizing a wide EAB.

Related studies have shown that the coercivity value (H_c) of zero-dimensional magnetic materials is lower than that of 1D magnetic materials (1D MM). H_c is related to a specific heterostructure [183]. The magnetic domains in the magnetic chain move faster than zero-dimensional nanoparticles. The synthesis of 1D magnetic nanochains is generally induced by a parallel magnetic field, triggered by the tendency of the system energy to tend to the minimum energy spontaneously. This magnetic field-induced self-assembly process is a competitive process resulting from different interactions of the nanoparticles. The possible interactions of these forces include space and electrostatic repulsion caused by surface coating, magnetic dipole attraction and Brownian motion.

Lu et al. [184] synthesized a multi-layer sandwich $Ti_3C_2T_x$ MXene composite in situ modified by 1D Co nanochains. By adjusting the content of magnetic nanochains, good impedance matching and wave absorbing effects can be achieved. In the case of 1.02 mm thickness, there is an optimal absorption of -46.48 dB, as shown in Fig. 31b. The absorbing schematic diagram of MXene and 1D Co nanochains can be shown in the following Fig. 31a. In addition to the most common

conduction losses that cause dielectric losses, dipole polarization, and interface polarization, and eddy current effects and resonance losses that cause losses, there is also the interlacing magnetic flux field effect (IMFFE). It mainly refers to magnetic nanochains, whose domain motion and coercivity are different from those of nanoparticles, forming a circulating magnetic flux field. Many magnetic fields are interlaced with each other to form a complex magnetic field network. Due to electromagnetic interactions, the dielectric properties of the material react and cause magnetic loss.

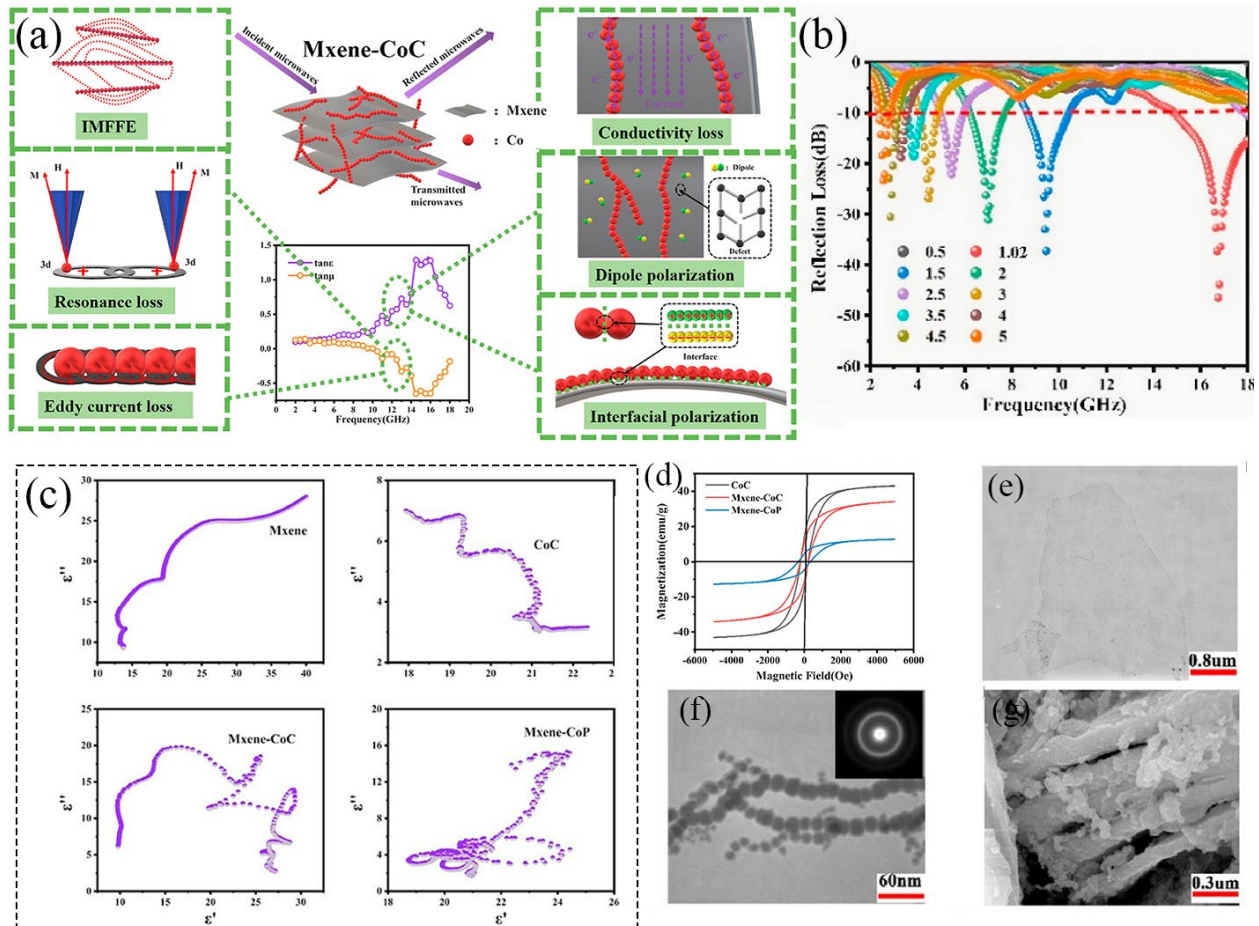


Fig. 31 (a) Schematic diagram of EMA of MXene and Co chains composite materials. (b) Reflection loss of MXene-CoC with different thicknesses from 2.0 to 18.0 GHz (c) Cole-Cole curves of samples. (d) Hysteresis

loops of CoC, MXene-CoC and MXene-CoP measured at room temperature. TEM images of (e) MXene, (f) CoC, and SEM image of (g) MXene-CoC [184]. Copyright 2020, Elsevier.

Liu et al. [13] studied the growth of 1D magnetic Ni nano-chains on 2D MXene sheets through experiments. SEM images of Fig. 32f-h correspond to a, b, and c, respectively. One can observe that MXene and Ni chains are uniformly compounded together. Through theoretical analysis, the cooperation effect of MXene and Ni results in the composite with excellent EMW absorption properties. The obtained electromagnetic parameters, ε' , ε'' , μ' , μ'' are displayed in Fig. 32b. The real part ε' μ' representing energy storage, and the imaginary part ε'' μ'' representing energy consumption both have a significant increase. Among them, when the content of MXene is 30 wt%, the loss tangent $\tan\delta_\varepsilon + \tan\delta_\mu$ and attenuation constant α (Fig. 32a). Means that it can have a higher consumption performance. However, the wave absorbing performance (Fig. 32e) of the 10% is the best. When the thickness is 1.7 mm, and the frequency is 11.9 GHz, the minimum reflection loss is -49.9 dB (Fig. 32b). The range of 10 wt% closest to 1 is wider, meaning more EMW can enter into the composite and produce less reflection. So that even under a minor loss tangent $\tan\delta_\varepsilon + \tan\delta_\mu$ and attenuation constant α , higher absorbing performance can be achieved.

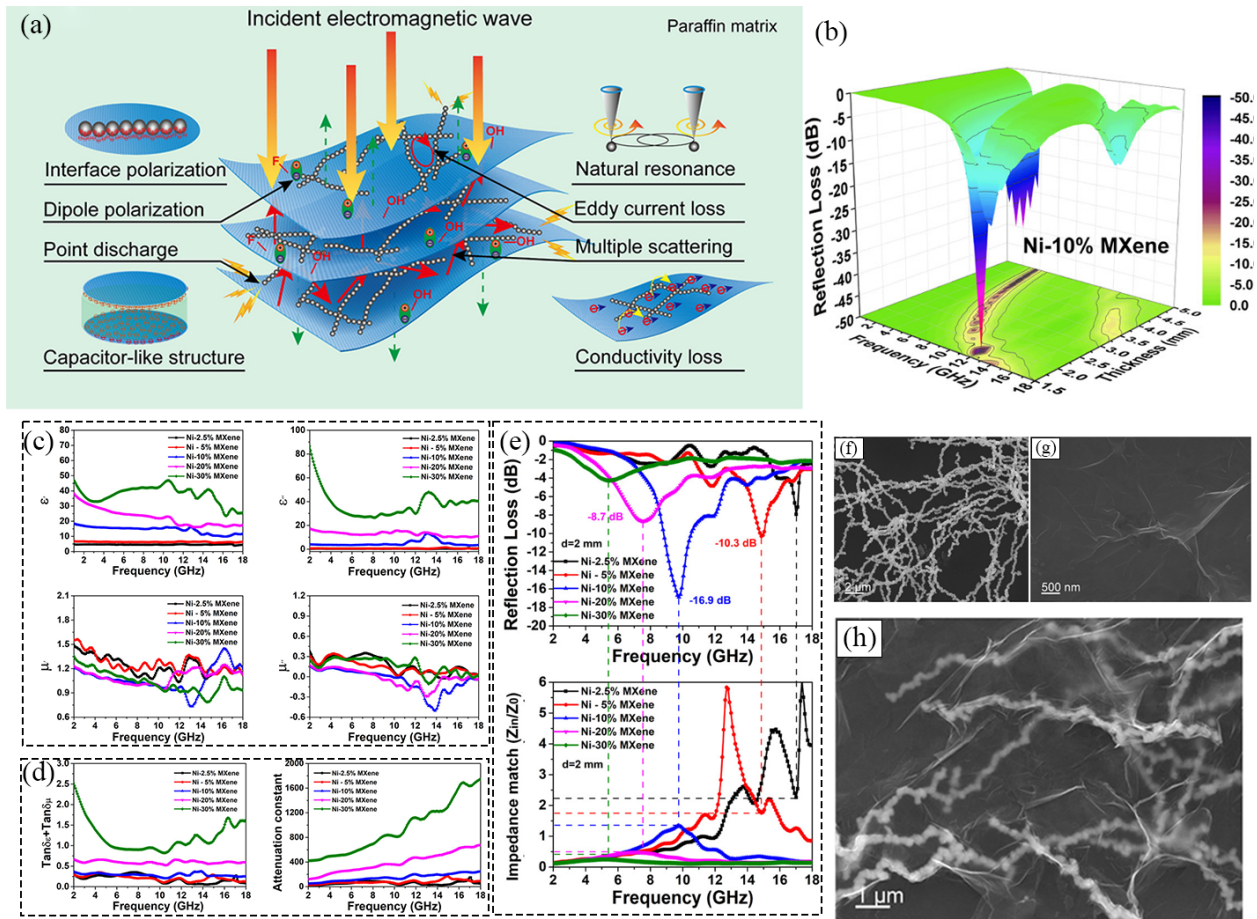


Fig. 32 Schematic diagram of EMA of MXene and Ni chains composite. Frequency dependence of (b) real and imaginary permittivity and (c) $\tan\delta_\epsilon + \tan\delta_\mu$ and attenuation constant of Ni-2.5% MXene, Ni-5% MXene, Ni-10% MXene, Ni-5% MXene, Ni-10% MXene, Ni-20% MXene and Ni-30% MXene. (d) Reflection loss of Ni-10% MXene with various thicknesses, and (e) the related 3D plots. The SEM images of (f) Ni chains and (g) MXene and (h) Ni@MXene [13]. Copyright 2019, American Chemical Society.

With ice templates, a stable three-dimensional aerogel structure can be obtained [185]. The three-dimensional aerogel is more conducive to the absorption of EMW by the material. Feng et al. [82] continued to compound rGO on the basis of Ni chain and MXene. They synthesized a 3D magnetic Ni nanochain/MXene/rGO aerogel using the directional freezing method and hydrazine

vapor reduction method. It can be seen from the Fig. 33e-i that the entire skeleton is composed of 35 μm structural units. The overall skeleton has an ultra-thin wall layer. And it has an ultra-low density of $6.45 \text{ mg}\cdot\text{cm}^{-3}$ as well as a lower filling volume. Under vacuum-assisted suction filtration, the aerogel is filled with polydimethylsiloxane (PDMS) precursor and undergoes a curing process to maintain a stable aerogel structure in the matrix. As the mass ratio of absorbing material to PDMS is 0.64 wt%, the $R_{L_{\min}}$ and the widest EAB reach up to -75.2 dB and 7.3 GHz at 2.15 mm thickness, respectively, comparing with EMA materials mixed with traditional paraffin or PVDF matrix.

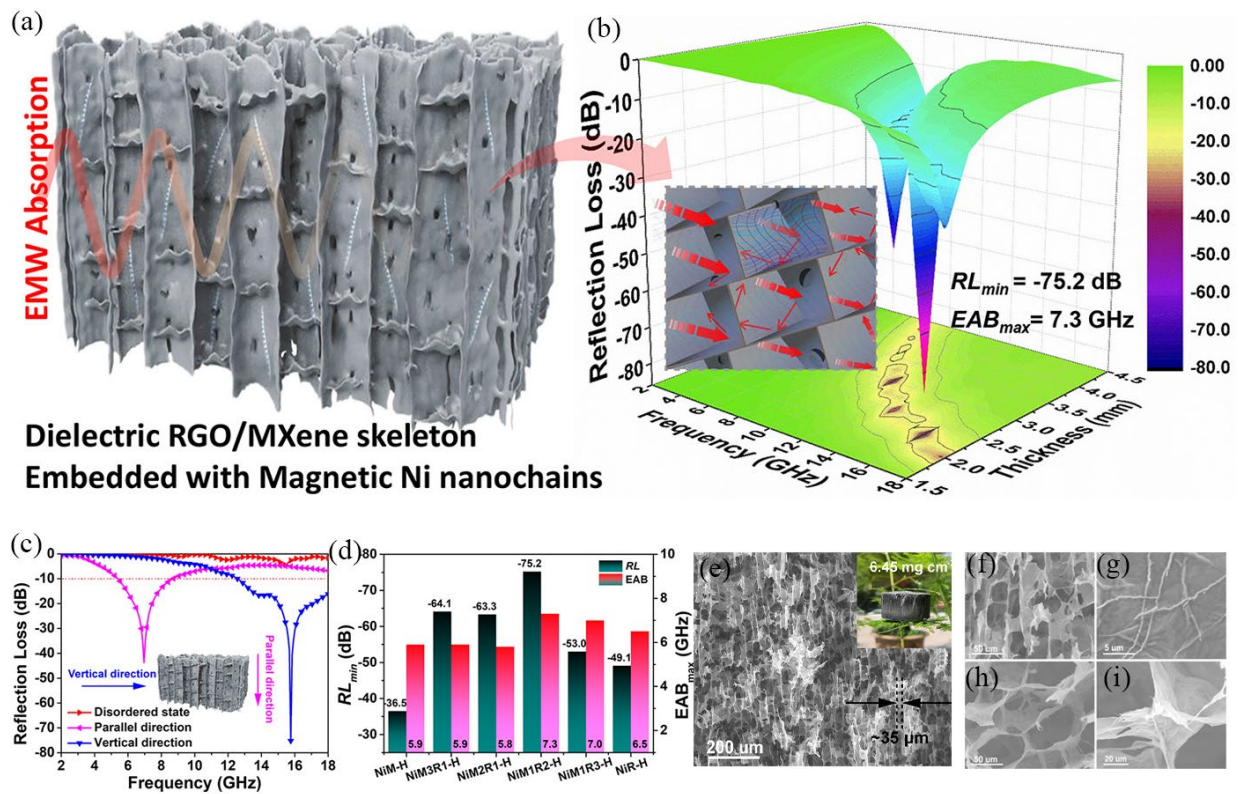


Fig. 33 Schematic diagram of (a) 3D magnetic Ni nanochain/MXene/rGO aerogel skeleton and (b) its best reflection loss. (c) A NiMR-H aerogel in the parallel direction, vertical direction and disordered state and (d)

statistics of R_{Lmin} and EAB_{max} for different NiMR-H aerogels. (e) SEM, photograph (inset of the NiMR-H aerogel. (f, g) Side-view and (h, i) top-view SEM images of NiMR-H aerogel. [82] Copyright 2021, American Chemical Society.

Aerogel has anisotropy in structure, and the direction of absorption is tested at the same time. As shown in Fig. 33c, under the same other conditions, the R_L value of the vertical and aperture directions is significantly lower than that of the parallel direction and disordered structure. The disordered structure does not have a complete conductive network and lossy structure. The incident EMW in parallel directions will pass through the hollow structure due to the absorbing material's minimal obstruction of EMW [186]. Only when EMW are incident in the vertical direction, the three-position structure of aerogel can be fully utilized. It shows that the spatial structure has a tremendous influence on the absorbing performance.

4.2 Electromagnetic absorption of CPs.

The pure CPs have good conductivity, and its conductivity can be controlled according to experimental conditions. Generally speaking, the conductivity of the absorbing material varies between 10^{-4} - 10^{-1} S/cm. According to the principle of absorbing, CPs can be used as absorbing material alone. According to the different microstructures, it can be roughly divided into four types: (1) zero-dimensional nanoparticles; (2) 1D nanowires, nanotubes, etc.; (3) 2D nanosheets; (4) 3D porous structure [187, 188].

For 0-dimensional nanoparticles, there are few studies on the absorbing properties of pure CPs, and the absorbing performance is only adjusted by changing the experimental parameters.

When the pure CPs are used as a wave absorbing material, its attenuation mechanism cannot achieve impedance matching, reducing the wave absorbing ability. For 1D materials, the conductive network can be strengthened by interweaving each other. In contrast, the 2D material strengthens the multi-reflection absorption on the basis of the conductive network.

Oyharçabal et al. [189] studied the absorbing properties of three different forms of PANI. The 0-dimensional spherical PANI (Fig. 34b) was synthesized by the traditional polymerization method [190]. Using an acid solution that quickly mixes APS and aniline monomers by adopting Huang's method, 1D PANI nanofibers (noted PANINF as shown in Fig. 34c) were synthesized [191]. Furthermore, in Fig. 34d, clay is used as a nano template [192] to synthesize sheet-like 2D PANI nanosheets. The maximum reflection loss of the sheet-shaped PANI composite is -37 dB, which is far more than the fibrous PANI and spherical PANI composites with -8 dB and -7 dB, respectively. PANICN has and higher dielectric loss and better impedance matching, which can explain this higher absorption value.

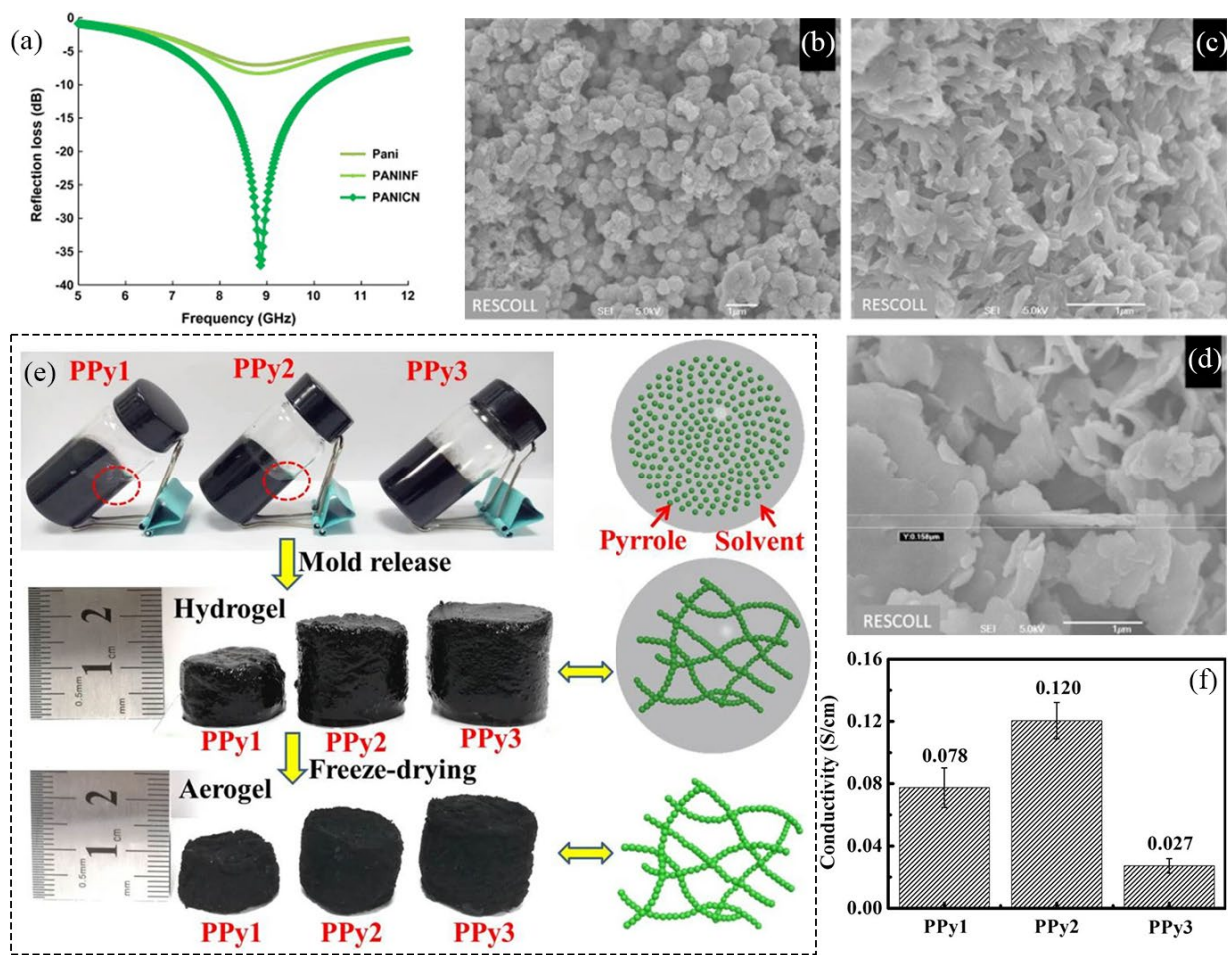


Fig. 34 (a) Microwave absorbing performances of composites containing 15 wt% PANI having various morphologies. And the thickness of the absorbing layer of PANI, PANINF and PANICN: 3.3 mm, 3.2 mm and 2.6 mm. SEM images of (b) globular PANI, (c) fibrillar PANI and (d) flake-like PANI [189]. Copyright 2012. Elsevier. (e) Digital photos of preparation process of PPy aerogels. (f) The different conductivity with PPy1, PPy2, and PPy3 [193]. Copyright 2019. Springer Science Business Media.

Yu et al. [193] to the FeCl_3 as oxidant, by simple chemical oxidation and freeze-dried aerogels, prepared PPy having elasticity. Fig. 34e shows the structure diagram, where PPy1, PPy2, and PPy3 separately represent FeCl_3/Py molar ratios of 1:1.5, 1:1 as well as 1.5:1. At a thickness of 2mm, PPy1 aerogel has the smallest R_L value of -55 dB at 14 GHz, exceeding ppy2's -29 dB at 13.7 GHz,

but the EAB of PPy2 aerogel is as high as 5.6 GHz (11.6-17.2 GHz). It may be that PPy1 has a moderate conductivity (0.078 S cm^{-1} shown in Fig. 34f), which can reduce the reflection of EMW while causing conductive loss. Meanwhile, PPy2 aerogel displays the merits of moderate mechanical strength, low density, thin matching thickness, wide absorption bandwidth, etc. Its excellent EMW absorption performance is related to 3D PPy frame, excellent impedance matching performance, quarter-wave interference, and dielectric loss. PPy aerogel with excellent EMW absorption performance and mechanical properties highlight its application potential in EMW absorption field.

In order to improve the dielectric loss of a single CPs, introducing a more robust interfacial polarization core-shell structure is a better way to achieve it. Tian et al. [194] selected PPy microspheres as the cores to synthesize PPy@PANI composites with a uniform core-shell structure, as shown in Fig. 35e-f. In comparison with inorganic materials, PPy microspheres as cores have a much stronger affinity for adsorbing aniline molecules. This is far more than inorganic substances that require bridging to recombine. At the same time, it has an absolute advantage in quality. In the situation of the mass ratio of PPy to PANI of 1.2, the maximum absorption value is at 8.8 GHz, and it can reach -51.3 dB at 3 mm thickness, as shown in Fig. 35c. PPy@PANI composite materials can achieve different EMW absorption properties through the adjustment of the absorbing layer thickness and the thickness of the PANI shell. Fig. 35 (b) shows the influence of the thickness of the control shell from 30 to 120 nm on the absorption. The absorption performance is best when the shell is 85nm. The PANI shell and the PPy core achieve higher interface polarization at this

thickness, resulting in better impedance matching.

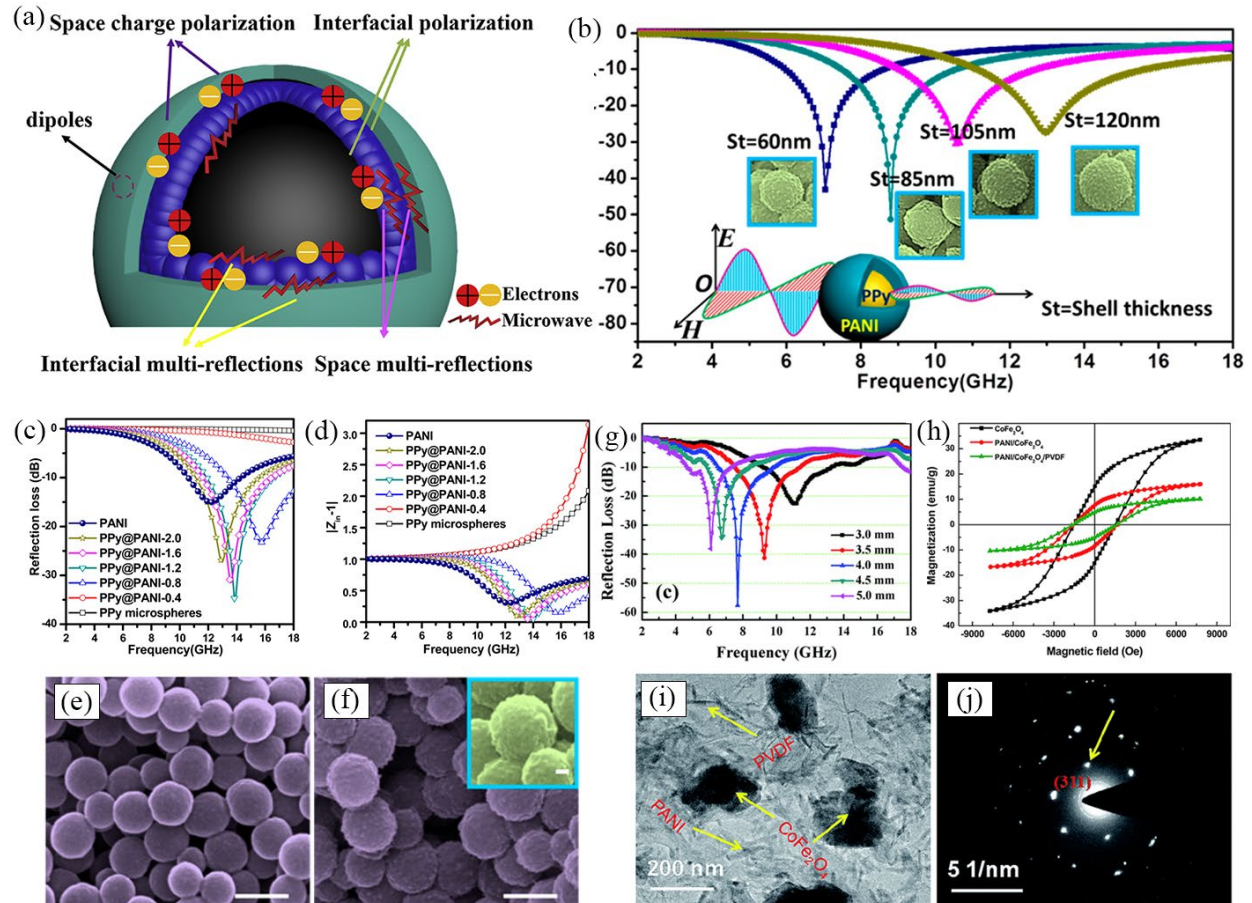


Fig. 35 (a) Electromagnetic loss diagram of core-shell structure PPy@PANI. (b) The impact of shell thickness on EMA. (c) Reflection loss curves of PPy microspheres, PPy@PANI composites, and pristine PANI at 2 mm thickness in 2-18 GHz. (d) Modulus of $Z_{in}-1$ of composites at 2 mm thickness in 2-18 GHz. SEM images of (e) PPy microspheres and (f) PPy@PANI composites [194]. Copyright 2015. American Chemical Society. (g) Reflection loss of PANI/CoFe₂O₄/PVDF composite with different thicknesses. (h) Magnetization curves of CoFe₂O₄ powder, PANI/CoFe₂O₄ composite and PANI/CoFe₂O₄/PVDF composite. (i) TEM and (j) SAED patterns of PANI/CoFe₂O₄/PVDF composite [195]. Copyright 2016. RSC.

As mentioned earlier, the absorption strength of purely electric polymers is limited. It mainly

relies on the multi-reflection of the structure so that as many EMW as possible are consumed through dielectric loss. As a result, the absorption band is narrow, and the absorption effect is poor. In fact, the binary composite material of magnetic material and CPs not only has good conductivity and magnetism. It also changes the attenuation of EMW from the original single dielectric loss to a combination of dielectric and magnetic losses. This is similar to the study of MXene absorbing materials. At present, such binary material has also been widely reported.

When PANI is used as an absorbing material alone, its attenuation mechanism cannot realize the impedance matching, seriously limiting its absorbability. Yang et al. [195] synthesized PANI/CoFe₂O₄/PVDF composite by coating CoFe₂O₄ with PANI in order to make up for the shortcomings of pure PANI's absorbing performance. The reflection loss can be up to -57.7 dB at 7.6 GHz in the case of 4 mm thickness, and the EAB can be up to 3.4 GHz with the R_L below -10 dB.

Wang et al. [196] studied the influence of polymers on the regulation of dielectric attenuation by core/shell nanostructures. A 2D core-shell structure composite material was synthesized using conducting polymer PANI and insulating polymer PS as the shell and Ni chain as the core. It can be seen from electron microscope images of Fig. 36g-i, that both Ni chains are successfully coated by PANI and PS. The composite material Ni/PANI NCs has the best absorption performance, as shown in Fig. 36a-c. At 8.18 GHz and 2.71 mm thickness, the minimum reflection loss can be -51.16 dB. In the meantime, the same answer can be obtained from impedance matching. The impedance matching diagrams of the three are shown in Fig. 36j-l. The impedance matching of

Fig. 36k is closest to 1, which tends to be thinner and has a broader frequency. Compared with the Ni nano-chain modified by 4-aminobenzoic acid (PABA), it is coated with an acid-doped PANI shell coating. The interface polarization is enhanced through the core/shell interface charge accumulation and electronic transition, and the dielectric attenuation is greatly enhanced. However, the non-polar PS shell layer is only covered with Ni nano-chains. Due to the directional transfer of charge in the Ni chain only acts like a wire, which weakens the interface polarization. The interface dipolar polarization induced by the polymer shell plays a vital role in dielectric adjustment and good impedance matching.

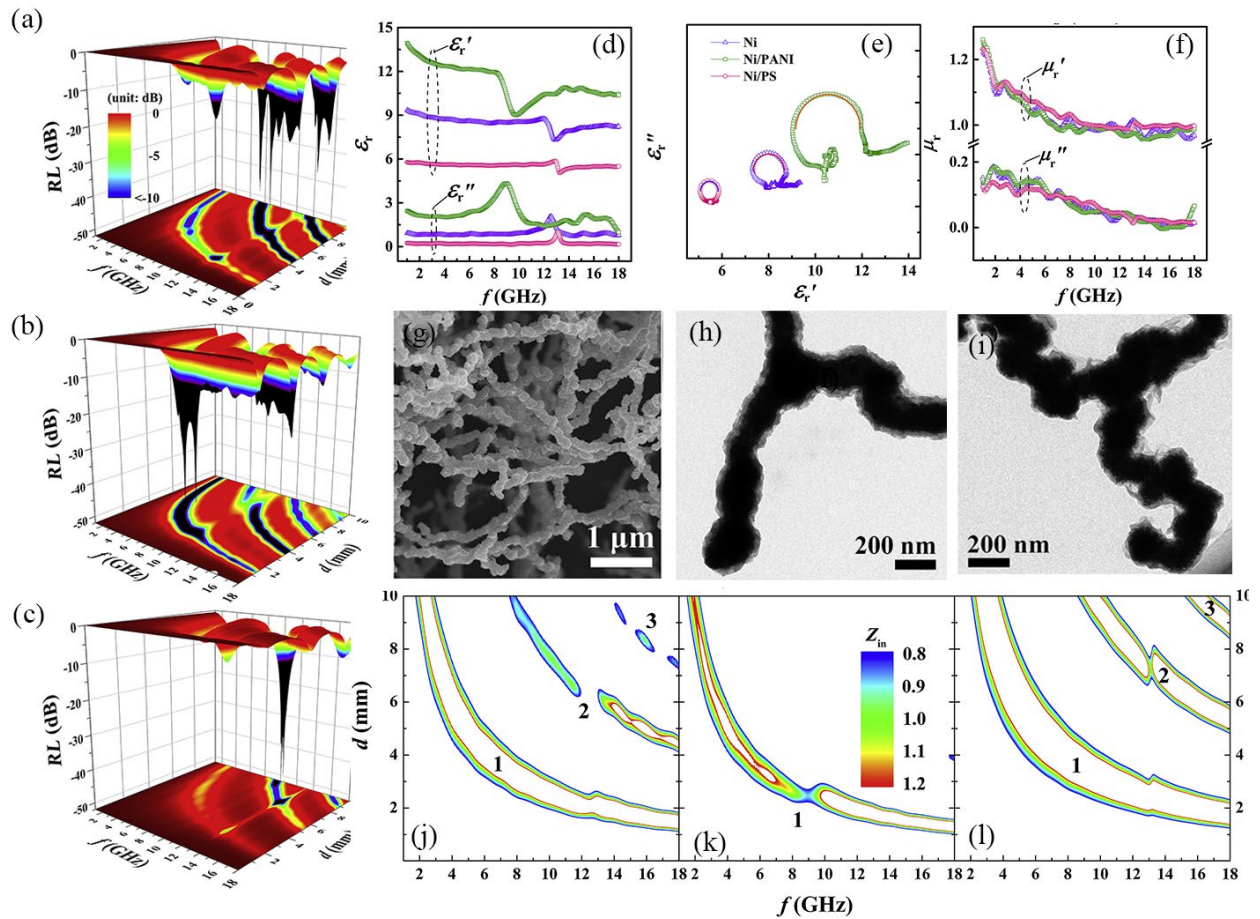


Fig. 36 RL of the paraffin-bonded samples of (a) Ni, (b) Ni/PANI NCs, and (c) Ni/PS NCs. Frequency dependence

of (d) complex relative permittivity ϵ_r , (f) complex relative permeability μ_r of the samples of Ni, Ni/PANI and Ni/PS NCs; (e) Cole-Cole plots of the samples. (g) SEM image of typical Ni NCs; TEM images of (h) Ni/PANI and (i) Ni/PS core/shell structured NCs, respectively. 2D-contour maps of f and d dependent Z_{in} for the (j) Ni, (k) Ni/PANI, and (l) Ni/PS NCs paraffin-bonded samples [196]. Copyright 2019. Elsevier.

4.3 Electromagnetic absorption of MXene and CPs

Both MXene and CPs have good electrical conductivity, and the interwoven conductive network has more defects and brings more ohmic losses. Abundant polar groups, such as -F, -O on the surface of MXene and -O, -N, -OH on the surface of CPs, are prone to dipole polarization. Furthermore, an uneven distribution of charges is formed at the contact interface because of the different electrical conductivity, resulting in a vital interface loss. This series has strengthened the loss of EMW in terms of the dielectric. The composite material of the two is quite promising as a research and development absorbing material. However, there are still relatively few studies in this area.

Huang et al. [197] studied the polymerization of aniline monomer between the surface and the inner layer of $Ti_3C_2T_x$. Due to the alternately arranged sandwich structure of $Ti_3C_2T_x$ MXene and PANI, there is a synergy between $Ti_3C_2T_x$ and PANI. By strengthening the interface polarization, dipole polarization, etc., the dielectric properties are improved so that the composite material has unique EMW absorption properties. At a thickness of 1.8mm at 13.80 GHz, the best reflection loss is -56.30 dB. With increasing PANI content, both the ϵ' and ϵ'' of $Ti_3C_2T_x$ /PANI increase, showing a dispersion phenomenon similar to the original PANI. Therefore, the aniline

content is the main factor that determines the dielectric loss.

Liu et al. [59] modified the $\text{Ti}_3\text{C}_2\text{T}_x$ MXenes sheet with conductive PPy microspheres. While preserving the original layer structure, a new core-shell structure is also obtained. Fig. 37d-e are SEM images of MXene with PPy modification. The core-shell structure of MXene and CP has prominent interface polarization, obvious confinement effect and synergistic effect. There is a band gap between $\text{Ti}_3\text{C}_2\text{T}_x$ MXene lamellae, and the lamellae contain abundant surface-active groups such as -OH and -F. These features provide conditions for PPy to cover between $\text{Ti}_3\text{C}_2\text{T}_x$ MXene layers. The filling amount of the composite material in the paraffin is only 10%, and the $R_{L\min}$ can reach -49.5dB at 3.6 mm and 7.6 GHz. Through adjustment, the maximum EAB can reach 6.63 GHz. These indicate that a proper ratio of MXene and PPy can increase the heterostructure, bring stronger interface polarization and stronger wave absorbing ability.

Chain-shaped CPs have a more complete conductive network than particles. Tong et al. [198] used HF to etch Ti_3AlC_2 . The multi-layer heterostructure modified with PPy chains was successfully grown and synthesized in the $\text{Ti}_3\text{C}_2\text{T}_x$ MXenes sheet by the method of in-situ chemical oxidative polymerization. The structure and loss schematic diagram and SEM image of chain-like PPy in the MXene sheet are shown in Fig. 37f, h. The $\text{Ti}_3\text{C}_2\text{T}_x$ /PPy composite has a content of 25 wt% in the paraffin matrix. As shown in the 3D Fig. 37g, The $R_{L\min}$ and the maximum EAB can reach -49.2 dB and 4.9 GHz at 3.2 mm thickness. At the same time, its best absorbing thickness (Fig. 37i) satisfies the 1/4 wavelength theory. Compared with growing PPy particles between MXene sheets, although there is no obvious increase in the best absorption performance, there is

a real reduction in the thickness of the absorbing layer.

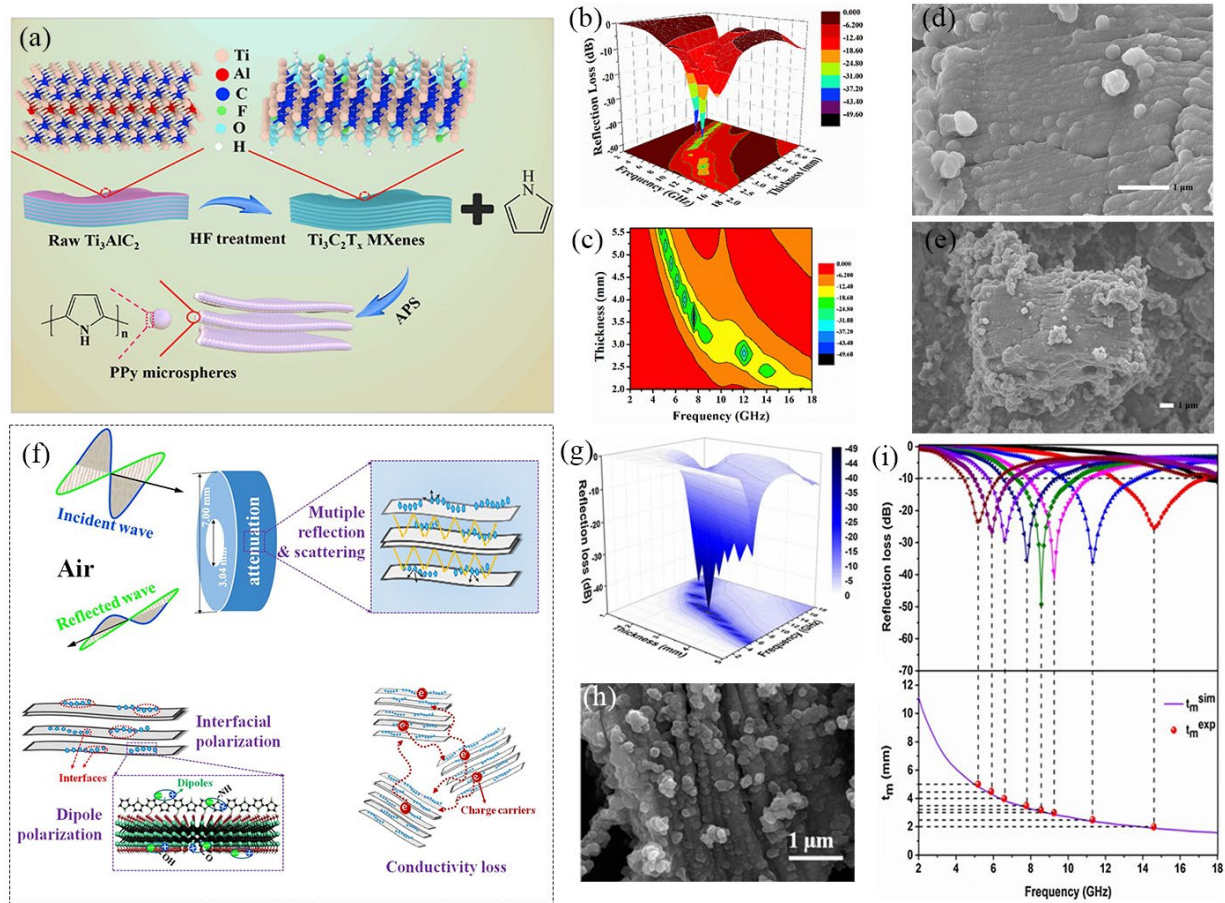


Fig. 37 (a) Demonstration of fabrication process, (b) 3D images and (c) 2D contours of calculated R_L values and (d,e) SEM images for $Ti_3C_2T_x@PPy$ composites [59]. Copyright 2019, Elsevier. (f) Schematic illustration of EMA mechanisms of the $Ti_3C_2T_x/PPy$ composite. (g) 3D representation of R_L values versus frequency and thickness and (h) SEM image of the $Ti_3C_2T_x/PPy$ composite. (i) R_L curves and dependence of matching thickness (t_m) on matching frequency (f_m) of $Ti_3C_2T_x/PPy$ with a 25 wt% filler loading. SEM images of $Ti_3C_2T_x/PPy$ [198]. Copyright 2017, Elsevier.

In order to achieve the double loss of the EMW absorber, proper impedance matching and synergistic effect. The heterostructure of the ternary composite material of magnetic material, CP

and MXene was designed. This ternary composite material brings stronger electromagnetic losses. Wu et al. [199] used HCl and LiF to etch $\text{Ti}_3\text{C}_2\text{T}_x$ (Fig. 38a) and reacted at a high temperature of 180°C for 24h by a one-step hydrothermal method to precipitate TiO_2 (Fig. 38b-c) on the surface of MXene. In turn, the aniline monomer is polymerized in situ on the MXene sheet. The $\text{Ti}_3\text{C}_2\text{T}_x/\text{TiO}_2/\text{PANI}$ multilayer composite material (Fig. 38e) was successfully synthesized. TiO_2 particles are grown on the periphery of $\text{Ti}_3\text{C}_2\text{T}_x$ via hydrothermal reaction. As the $\text{Ti}_3\text{C}_2\text{T}_x/\text{TiO}_2$ sample is coated with PANI, its surface becomes rough. However, there are still gaps between the layers, enhancing the interface polarization and dramatically improving EMW absorption performance.

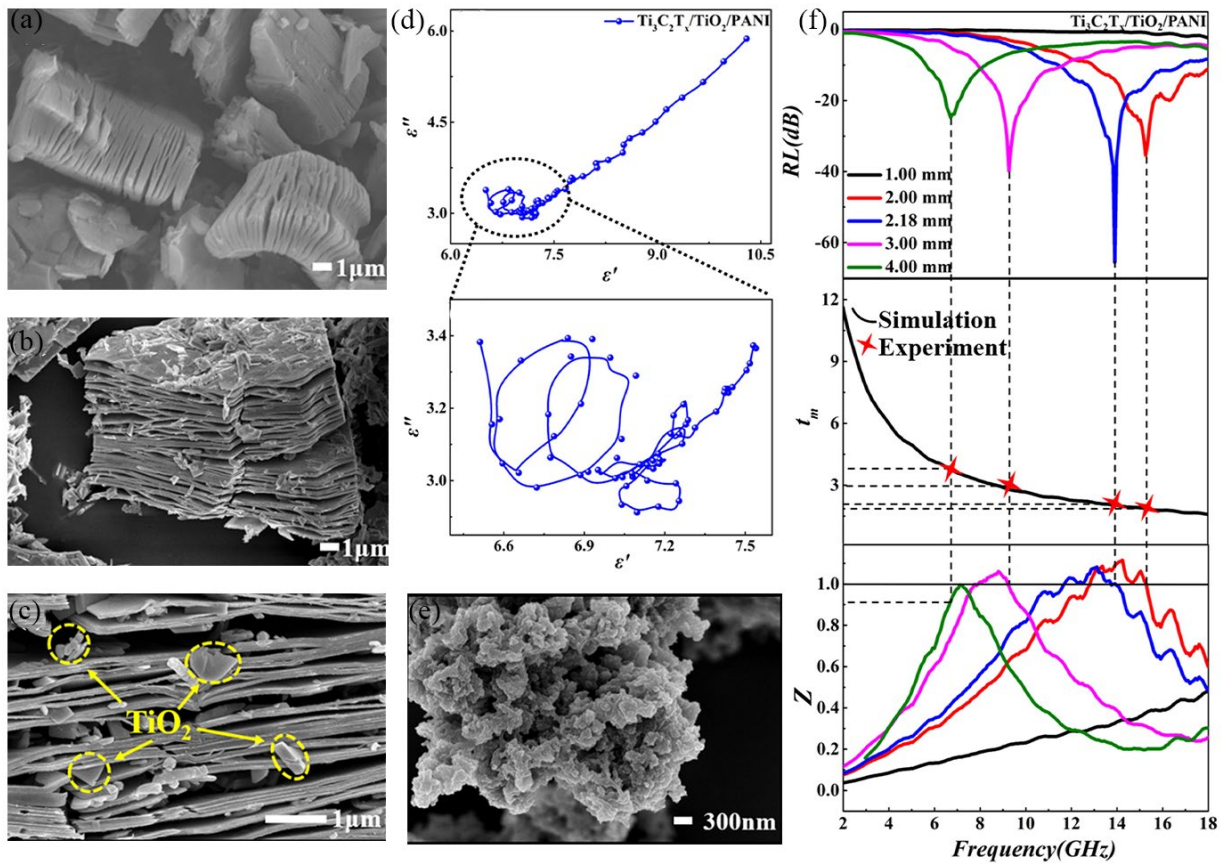


Fig. 38 SEM images of (a) $\text{Ti}_3\text{C}_2\text{T}_x$, (b, c) $\text{Ti}_3\text{C}_2\text{T}_x/\text{TiO}_2$ and (e) $\text{Ti}_3\text{C}_2\text{T}_x/\text{TiO}_2/\text{PANI}$. (d) Typical Cole-Cole models

and (f) the R_L curves, the absorber thickness and impedance matching curves of $Ti_3C_2T_x/TiO_2/PANI$ sample [199]. Copyright 2020, Elsevier.

Wang et al. [200] designed a sandwich structure $Ti_3C_2/Fe_3O_4/PANI$ ternary composite material. Fig. 39d-f are FESEM images of Ti_3C_2 , Ti_3C_2/Fe_3O_4 and $Ti_3C_2/Fe_3O_4/PANI$ respectively. The smooth Ti_3C_2 surfaces are covered by PANI and Fe_3O_4 , showing a thicker and rougher surface. At 15.3 GHz, the maximum R_L $Ti_3C_2/Fe_3O_4/PANI$ composite is -40.3 dB. EAB can reach 5.2 GHz at 1.9 mm, higher than that of Fe_3O_4 and Ti_3C_2/Fe_3O_4 . In addition, EAB can reach 12 GHz (6 ~ 18 GHz) by the adjustment of the absorbing thickness.

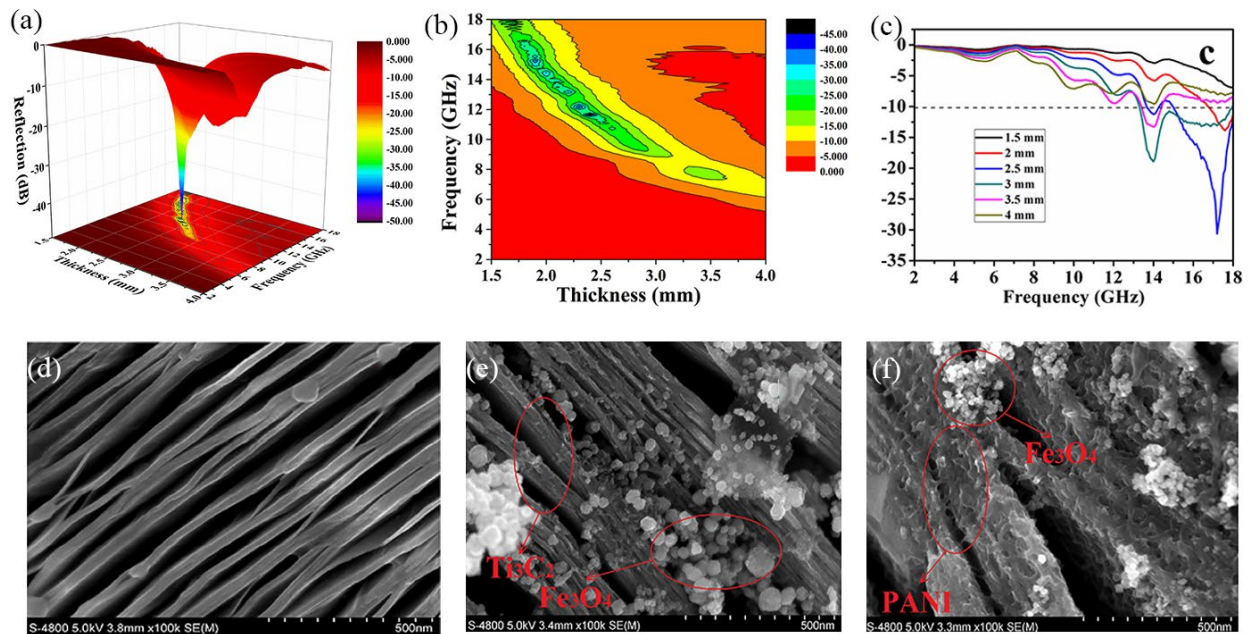


Fig. 39 (a) 3D presentation, (b) contour map and (c) reflection loss curves of $Ti_3C_2/Fe_3O_4/PANI$. FESEM images of (d) Ti_3C_2 , (e) Ti_3C_2/Fe_3O_4 and (f) $Ti_3C_2/Fe_3O_4/PANI$ [200]. Copyright 2019. Elsevier.

Table 1 The EMW absorption performances of MXene, CPs and their composites in recent years.

	Sample	Matrix	Loading (%)	R _L min (dB)	Thickness (mm)	Corresponding frequency (GHz)	EAB (GHz)	Corresponding Thickness (mm)	Ref
	Ti ₃ C ₂ T _x	paraffin	50	-48.4	1.7	11.6	2.8	1.8	[129]
	Ti ₃ C ₂ T _x	paraffin	50	-40	3	7.8	6.8	2	[81]
	Nb ₂ CT _x	paraffin	70	-52.2	2.9	3.93	-	-	[44]
	MXene/Ni	PVDF	10	-52.6	3	8.4	6.1	2	[181]
	MXene/Ni	paraffin	-	-50.5	3.5	5.5	5.28	3.5	[182]
	MXene/Ni Chain	paraffin	10	-49.9	1.75	11.9	-	-	[13]
	MXene@Fe ₃ O ₄	paraffin	40	-63.3	1.8	5.2	5.2	1.8	[201]
	MXene/Fe ₃ O ₄	paraffin	60	-48.7	1.9	9.9	3.9	1.7	[6]
	Ti ₃ C ₂ T _x /NiCo ₂ O ₄	paraffin	50	-50.96	2.18	12.24	0.88	2.18	[202]
	MXene/CoFe ₂ O ₄	epoxy and polyamide resin	40	-30.9	1.5	11.9	8.5	1.5	[203]
MXene	MXene/Co chains	paraffin	50	-46.48	1.02	16.75	-	-	[184]
	MXene/ZnO	paraffin	25	-26.3	4.0	17.4	1.4	4	[204]
	TiO ₂ /Ti ₃ C ₂ T _x /Fe ₃ O ₄	paraffin	70	-57.3	1.9	10.1	2.4	1.0	[180]
	Ti ₃ C ₂ T _x /CNTs	paraffin	35	-52.9	2.65	7.15	4.46	1.55	[205]
	CoNi@Ti ₃ C ₂ T _x	paraffin	40	-58.18	1.55	13.2	5.68	1.55	[206]
	RGO/MXene/Fe ₃ O ₄	paraffin	40	-51.2	2.9	11.1	6.5	2.0	[207]
	Ti ₃ C ₂ T _x /Ni-spheres	paraffin	50	-47.06	1.5	12.4	3.6	1.5	[15]
	Fe ₃ O ₄ @Ti ₃ C ₂ T _x	paraffin	40	-57.2	4.2	15.7	4.46	1.55	[208]
	CF/MXene	paraffin	-	-45	4.5	8.8	5	4.5	[209]
	TiC/SiBCN	-	-	-45.44	2.3	10.93	4.05	2.3	[210]
	rGO/Nb ₂ CT _x /Fe ₃ O ₄	paraffin	50	-59.17	2.5	11.8	6.8	2.5	[211]
	CoFe@Ti ₃ C ₂ T _x	paraffin	60	-36.29	2.2	8.56	2.64	2.2	[212]

	flake-like PANI	epoxy	15	-37	2.6	8.8	-	-	[189]
	PPy aerogel	paraffin	10	-55	2	14	5.6	2	[213]
	PPy@PANI	paraffin	50	-51.3	3	8.8	4.7	2	[194]
	PANI/Ni	paraffin	40	-51.16	2.71	8.18	4.5	3	[196]
	PPy nanofibers/Fe ₃ O ₄	paraffin	30	-41.6	2.5	10	8	-	[214]
	PANI/CoFe ₂ O ₄	PVDF	-	-57.7	4	7.6	3.4	4	[195]
	MnO ₂ -PANI	-	50	-52.06	3	8.48	4.56	3	[69]
	CF@PANI	paraffin	10	-46.86	2.7	~9.0	-	-	[215]
	C/PANI	paraffin	80	-50.96	3.09	8.88	4	3.09	[216]
CPS	Zn _x Fe _{3-x} O ₄ /PANI	paraffin	50	-59.44	2.31	11.04	4.65	1.72	[70]
	CoFe ₂ O ₄ /C/PANI	paraffin	25	-51.81	2.57	12.4	8.88	2.50	[217]
	Fe ₃ O ₄ @SiO ₂ @PANI	paraffin	50	-44.9	1.5	4	4	1.5	[218]
	NiFe ₂ O ₄ /PC/PANI	-	20	-59.3	2	10.5	5.6	1.5	[219]
	ZnFe ₂ O ₄ @PANI-rGO	-	20	-49.99	2.1	17.28	4.32	2.1	[220]
	cellulose/PANI	paraffin	20	-49.24	3.6	-	6.0	2.5	[221]
	Fe ₃ O ₄ @SiO ₂ @PPy	paraffin	15	-40.9	5.0	6	6.88	5	[222]
	Fe ₃ O ₄ @PPy	paraffin	-	-40.53	2.5	6.32	5.12	2.5	[223]
	FeCo@SiO ₂ @PPy	paraffin	60	65.17	2.1	16.48	6.8	2.5	[224]
	MOF (Fe)/PANI	paraffin	70	-41.4	2	11.6	5.5	2	[225]
	Ti ₃ C ₂ T _x /PANI	paraffin	50	-56.3	1.8	13.8	-	-	[197]
	Ti ₃ C ₂ T _x @PPy	paraffin	10	-49.5	3.6	7.6	6.63	2.7	[59]
	Ti ₃ C ₂ T _x /PPy	paraffin	25	-49.2	3.2	8.5	4.9	2	[198]
MXene/CPS	Ti ₃ C ₂ T _x /TiO ₂ /PANI	paraffin	25	-65.61	2.18	13.92	5.92	2.10	[199]
	Ti ₃ C ₂ T _x /CNZFO/PANI	-	-	-37.1	2.2	10.2	4.1	2.2	[226]
	Ti ₃ C ₂ /Fe ₃ O ₄ /PANI	paraffin	30	-40.3	1.9	15.3	5.2	1.9	[200]

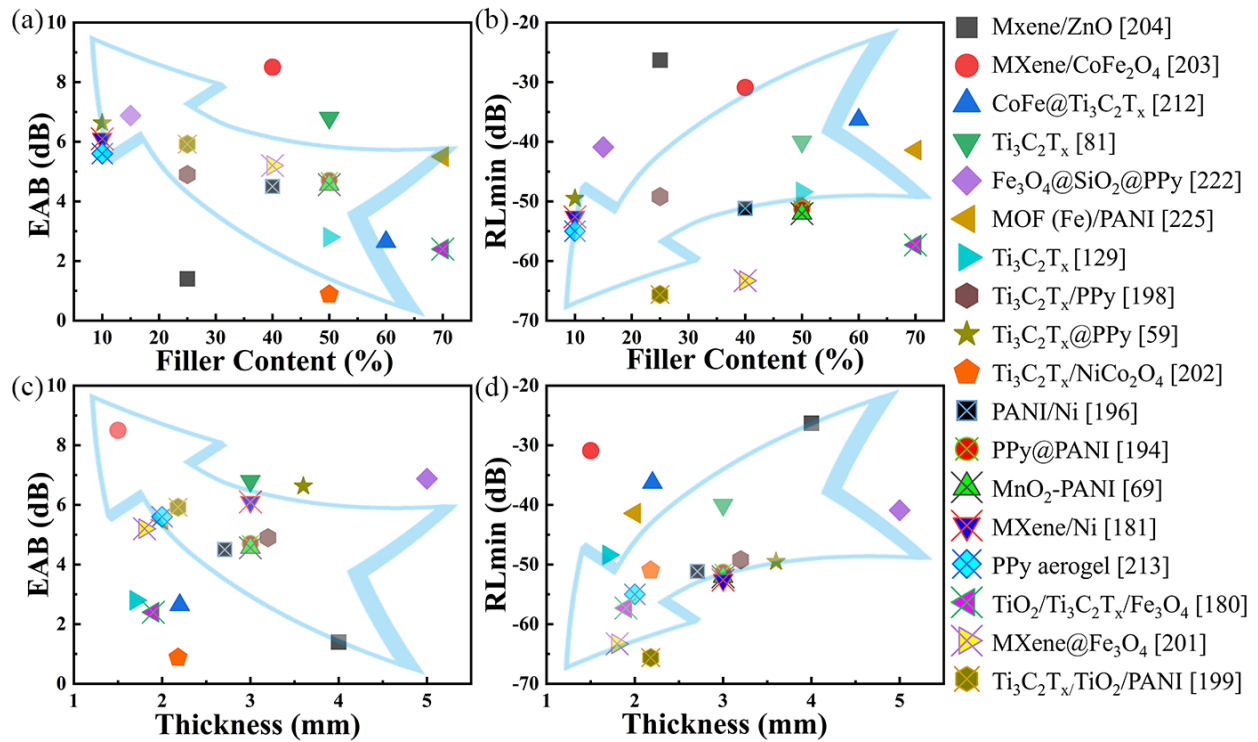


Fig. 40 The R_{Lmin} and EAB about frequency and thickness of common MXene and CPs and their composites in recent years.

In summary, the Table 1 shows the parameters related to the EMA of MXene and CPs and their composites in recent years, including the EAB and R_{Lmin} values at special frequencies and thicknesses. It is evident that the pure MXene and CPs have ideal wave absorbing performance, such as Ti₃C₂T_x (-48.4 dB) [129], Nb₂CT_x (-52.2 dB) [44] and PPy aerogel (-55 dB) [213]. However, those materials have the problem of thick thickness or narrow EAB. In practical applications, the EAB, absorption thickness and frequency, are usually optimized by compounding magnetic materials. For example, the R_{Lmin} of Fe₃O₄@SiO₂@PANI can be up to -44.9 dB at the thickness of 1.5 mm [218], and the EAB of CoFe₂O₄/C/PANI is 8.88 GHz at 2.5 mm [217]. Meanwhile the R_{Lmin} of MXene/Co chains can be up to -46.48 dB at the thickness of 1.02 mm

[184]. It is surprising that the combination of MXene and CPs can further improve the electromagnetic loss capability. The R_{Lmin} of $Ti_3C_2T_x/PANI$ can be up to -56.3 dB even at 1.8 mm thickness, and the optimal R_{Lmin} of $Ti_3C_2T_x/TiO_2/PANI$ is -65.61 dB at 2.18 mm. In order to compare the various properties of wave absorption more visually, the following Fig. 40 performance assessment diagram is given with the data from Table 1. The position of the four arrows in the figure at the same time is an ideal absorbing material. It is also a goal that needs to be struggling at present. Unfortunately, the materials that have been reported have not been able to meet this requirement. However, there are relatively few studies on composite materials based on MXene and CPs at present, and the number of reports is very few. Both have natural and unique advantages as absorbing materials, and more attention should be paid to this direction. The inherent structure of MXene makes its stability in the air relatively poor. It requires researchers to continuously construct structures and surface modifications to achieve stability, lightweight, and broadband performance. The actual application of MXene is still a long way to go.

5. Conclusion

This article reviews the recent research progress of MXene and CPs as absorbing materials. The basic concepts of wave absorbing theory are introduced. The etching method of MXene, the synthesis method of CPs, and the composite process of the two are introduced. The current methods for preparing MXene include HF etching, LiF + HCl etching, electrochemical etching and hydrothermal alkali etching. There is no doubt that the fluorine-containing etching method is currently the most widely used, but there are more significant safety risks. The synthesis method

of CPs, whether electrochemical or chemical, is essentially synthesized by oxidation. When they are compounded with MXene, the self-assembly in-situ polymerization method is simple to operate and has a strong binding force of materials. It is currently more widely used.

MXene has excellent conductivity, and there are certain defects in the conductive network, which can bring about the ohmic loss of EMW through the migration and transition of electrons. Multipolar groups on the surface form dipoles, which enhance the dielectric relaxation phenomenon in the form of dipole polarization. The multi-layer structure of MXene naturally forms a multi-reflection structure that absorbs waves, and more EMW are reflected back and forth between the MXene layers. CPs also have adjustable conductivity, are easy to process, and easily introduce more polar groups into long polymer chains through chemical modification. It has the unique natural advantages of dipole polarization, conduction loss, and lightweight required by absorbing materials.

The combination of MXene and CPs enhances the interface polarization. The synergy of the two in dielectric loss broadens the absorption frequency band and strengthens the absorption strength. By compounding different magnetic materials, the thickness of the absorbing layer can be adjusted. Design a reasonable 3D structure, such as the core-shell structure strengthened interface polarization, multi-layer, sandwich structure, 3D aerogel structure, and other EMW caused by multiple reflections. It can achieve good impedance matching and electromagnetic absorption in a specific GHz frequency band. Coupled with the advantages of a lightweight, especially in the military, this makes MXene, and CPs have great application potential in the field

of EMW absorption in the future.

6. Outlook

The development of lightweight, stable, efficient, and broadband absorbing materials is a hot research topic. At present, whether it is MXene or CPs absorbing material, although it is light in weight, it has a good performance in aspects such as strong EMW absorption in a specific frequency band. However, the bandwidth of the absorbing frequency band is relatively narrow for a single material, and the absorption strength can be further improved, which is far from the ideal absorbing effect. Researchers also need to actively explore its composite materials and play a synergistic effect to strive for excellent EMW absorbing properties.

Secondly, many theoretically predicted properties of excellent MXene and CPs absorbing materials need experimental verification. On the basis of theoretical research on absorbing performance, lightweight, and high frequency, we should also pay attention to practical applications in life, equipment, and the military.

In addition, the understanding of the exact mechanism of electromagnetic absorption is still immature [227, 228]. There is an urgent need for a series of in-depth studies on the dielectric relaxation loss and electromagnetic loss of materials. For the future development direction of absorbing materials, the design of absorbing materials should be as follows:

The first is based on the principle that EMW propagate energy through electric and magnetic fields, starting from the perspective of blocking the propagation medium. Increase the research on new types of magnetic and dielectric composite materials to achieve higher EMW magnetic loss

and dielectric loss.

The second is based on a large amount of literature data, theoretical calculation, and analysis. Theoretically, total absorption can be achieved when the impedance matching of the magnetic and the dielectric losses is equal to 1. From the perspective of impedance matching, when the selected materials are combined, adjust the content ratio of each component to make the impedance matching as close to 1 as possible.

Third, to achieve effective absorption of the absorbing material, it is necessary to make EMW enter the interior of the absorbing material as much as possible. At the same time, according to the theory of transmission lines, as the thickness of the absorbing material is an odd multiple of the $1/4$ wavelength of the EMW, the EMW will reflect the least. It is necessary to explore the thickness of the appropriate wave-transmitting layer and wave-absorbing layer.

Fourth, a layer of absorbing material alone cannot achieve good absorbing performance. It is necessary to design reasonable absorber structures, such as honeycomb structure, multilayer absorber structure, corrugated sandwich structure, etc., to achieve better absorber performance.

Fifth, in the information age, the development of smart materials has provided a new design idea for absorbing materials. According to the EMW of different frequency bands received, the wave absorber structure can be adjusted instantaneously to realize effective absorption of multiple frequency bands and wide bandwidth.

Finally, it should be a factor that must be considered, and attention should be paid to material safety, including the friendliness of the environment and the human body. At present, there is still

much room for innovation and growth in composite materials based on MXene and CPs, and even the road to maturity is long and difficult. Although there are still many challenges before practical application, we believe that with the continuous efforts of scientific researchers, lightweight, stable, efficient, broadband, and intelligent, absorbing materials will soon be used.

Acknowledgement

We gratefully appreciate the support of the Natural Science Foundation of Shandong (ZR2021ME019, ZR2019BB063). The author gratitude the environmental and function material team, supported by the Project of Shandong Province Higher Educational Young Innovative Talent Introduction and Cultivation. The authors extend their appreciation to the Deputyship for Research& Innovation, Ministry of Education in Saudi Arabia for funding this research work through the project number “X_2020__IF “

Conflict of Interest

The authors declare that they have no conflict of interest.

Reference

1. Liu J, Zhao Z, Zhang L (2020) Toward the application of electromagnetic wave absorption by two-dimension materials. *J Mater Sci: Mater Electron* 32:25562–25576.
2. Hou T, Wang B, Jia Z, Wu H, Lan D, Huang Z, Feng A, Ma M, Wu G (2019) A review of metal oxide-related microwave absorbing materials from the dimension and morphology perspective. *J Mater Sci: Mater Electron* 30(12):10961-10984.
3. Chen H, Ma W, Huang Z, Zhang Y, Huang Y, Chen Y (2019) Graphene - Based Materials toward Microwave and Terahertz Absorbing Stealth Technologies. *Adv Opt Mater* 7(8):1801318.
4. Zhao B, Deng J, Zhang R, Liang L, Fan B, Bai Z, Shao G, Park CB (2018) Recent Advances on the Electromagnetic

- Wave Absorption Properties of Ni Based Materials. *Engineered Science* 3:5-40.
5. Liu H, Li L, Cui G, Wang X, Zhang Z, Lv X (2020) Heterostructure Composites of CoS Nanoparticles Decorated on $Ti_3C_2T_x$ Nanosheets and Their Enhanced Electromagnetic Wave Absorption Performance. *Nanomaterials* (Basel) 10(9):1666.
 6. Liu P, Chen S, Yao M, Yao Z, Ng VMH, Zhou J, Lei Y, Yang Z, Kong LB (2020) Double-layer absorbers based on hierarchical MXene composites for microwave absorption through optimal combination. *J Mater Res* 35(11):1481-1491.
 7. Wang R, Li S, Hu P, Chen S, Wang JJEM, Manufacturing (2021) Densification Behavior and Microstructure Evolution of Mo Monocrystals by Microwave Sintering. *ES Materials & Manufacturing* 13:97-105.
 8. Singh SK, Akhtar MJ, Kar KK (2018) Hierarchical Carbon Nanotube-Coated Carbon Fiber: Ultra Lightweight, Thin, and Highly Efficient Microwave Absorber. *ACS Appl Mater Interfaces* 10(29):24816-24828.
 9. Deruelle F (2020) The different sources of electromagnetic fields: Dangers are not limited to physical health. *Electromagn Biol Med* 39(2):166-175.
 10. Roosli M (2008) Radiofrequency electromagnetic field exposure and non-specific symptoms of ill health: a systematic review. *Environ Res* 107(2):277-287.
 11. Liang J, Chen J, Shen H, Hu K, Zhao B, Kong J (2021) Hollow Porous Bowl-like Nitrogen-Doped Cobalt/Carbon Nanocomposites with Enhanced Electromagnetic Wave Absorption. *Chem Mater* 33(5):1789-1798.
 12. Luo F, Liu D, Cao T, Cheng H, Kuang J, Deng Y, Xie W (2021) Study on broadband microwave absorbing performance of gradient porous structure. *Adv Compos Hybrid Mater* 4(3):591-601.
 13. Liang L, Han G, Li Y, Zhao B, Zhou B, Feng Y, Ma J, Wang Y, Zhang R, Liu C (2019) Promising $Ti_3C_2T_x$

- MXene/Ni Chain Hybrid with Excellent Electromagnetic Wave Absorption and Shielding Capacity. *ACS Appl Mater Interfaces* 11(28):25399-25409.
14. Liao Q, He M, Zhou Y, Nie S, Wang Y, Wang B, Yang X, Bu X, Wang R (2018) Rational Construction of $Ti_3C_2T_x/Co$ -MOF-Derived Laminated Co/TiO_2-C Hybrids for Enhanced Electromagnetic Wave Absorption. *Langmuir* 34(51):15854-15863.
15. Li N, Xie X, Lu H, Fan B, Wang X, Zhao B, Zhang R, Yang R (2019) Novel two-dimensional $Ti_3C_2T_x/Ni$ -spheres hybrids with enhanced microwave absorption properties. *Ceram Int* 45(17):22880-22888.
16. Liu P, Ng VMH, Yao Z, Zhou J, Kong LB (2018) Ultrasmall Fe_3O_4 nanoparticles on MXenes with high microwave absorption performance. *Mater Lett* 229:286-289.
17. Zheng M, Wei Y, Ren J, Dai B, Luo W, Ma M, Li T, Ma Y (2021) 2-aminopyridine functionalized magnetic core-shell $Fe_3O_4@polypyrrole$ composite for removal of Mn (VII) from aqueous solution by double-layer adsorption. *Sep Purif Technol* 277:119455.
18. Zhang Z, Wang S, Lv Y, Chen X, Wu Z, Zou Y (2019) MnO_2 nanostructures deposited on graphene foams for broadband and lightweight electromagnetic absorption. *J Alloys Compd* 810:151744.
19. Ma Y, Xie X, Yang W, Yu Z, Sun X, Zhang Y, Yang X, Kimura H, Hou C, Guo Z, Du W (2021) Recent advances in transition metal oxides with different dimensions as electrodes for high-performance supercapacitors. *Adv Compos Hybrid Mater* 4(4):906-924.
20. Zhang L, Song T, Shi L, Wen N, Wu Z, Sun C, Jiang D, Guo Z (2021) Recent progress for silver nanowires conducting film for flexible electronics. *J Nanostructure Chem* 11(3):323-341.
21. Bag PP, Singh GP, Singha S, Roymahapatra G (2020) Synthesis of Metal-Organic Frameworks (MOFs) and Their

- Applications to Biology, Catalysis and Electrochemical Charge Storage: A Mini Review. *Engineered Science* 13:1-10.
22. Luo X, Yang G, Schubert DW (2021) Electrically conductive polymer composite containing hybrid graphene nanoplatelets and carbon nanotubes: synergistic effect and tunable conductivity anisotropy. *Adv Compos Hybrid Mater* 5:250-262.
23. Liang C, Du Y, Wang Y, Ma A, Huang S, Ma Z (2021) Intumescent fire-retardant coatings for ancient wooden architectures with ideal electromagnetic interference shielding. *Adv Compos Hybrid Mater* 4(4):979-988.
24. Zhao Y, Liu K, Hou H, Chen L-Q (2022) Role of interfacial energy anisotropy in dendrite orientation in Al-Zn alloys: A phase field study. *Mater Des* 216:110555.
25. Manikandan M, Francis PN, Dhanuskodi S, Maheswari N, Muralidharan G (2018) High performance supercapacitor behavior of hydrothermally synthesized CdTe nanorods. *J Mater Sci: Mater Electron* 29(20):17397-17404.
26. Fan G, Jiang Y, Xin J, Zhang Z, Fu X, Xie P, Cheng C, Liu Y, Qu Y, Sun K, Fan R (2019) Facile Synthesis of Fe@Fe₃C/C Nanocomposites Derived from Bulrush for Excellent Electromagnetic Wave-Absorbing Properties. *ACS Sustainable Chem Eng* 7(23):18765-18774.
27. Xie P, Liu Y, Feng M, Niu M, Liu C, Wu N, Sui K, Patil RR, Pan D, Guo Z, Fan R (2021) Hierarchically porous Co/C nanocomposites for ultralight high-performance microwave absorption. *Adv Compos Hybrid Mater* 4(1):173-185.
28. Wu N, Du W, Hu Q, Jiang SVQJES (2020) Recent Development in Fabrication of Co Nanostructures and Their Carbon Nanocomposites for Electromagnetic Wave Absorption. *Engineered Science* 13:11-23.

29. Gao S, Zhao X, Fu Q, Zhang T, Zhu J, Hou F, Ni J, Zhu C, Li T, Wang Y, Murugadoss V, Mersal GAM, Ibrahim MM, El-Bahy ZM, Huang M, Guo Z (2022) Highly transmitted silver nanowires-SWCNTs conductive flexible film by nested density structure and aluminum-doped zinc oxide capping layer for flexible amorphous silicon solar cells. *Journal of Materials Science & Technology* 126:152-160.
30. Sultanov F, Daulbayev C, Bakbolat B, Daulbayev O (2020) Advances of 3D graphene and its composites in the field of microwave absorption. *Adv Colloid Interface Sci* 285:102281.
31. Zhao W, Yan Z, Qian L (2020) Graphitic Carbon Nitride: Preparation, Properties and Applications in Energy Storage. *Engineered Science* 10:24-34.
32. Zhao Z, Zhao R, Bai P, Du W, Guan R, Tie D, Naik N, Huang M, Guo Z (2022) AZ91 alloy nanocomposites reinforced with Mg-coated graphene: Phases distribution, interfacial microstructure, and property analysis. *J Alloys Compd* 902:163484.
33. Jing C, Zhang Y, Zheng J, Ge S, Lin J, Pan D, Naik N, Guo Z (2022) In-situ constructing visible light CdS/Cd-MOF photocatalyst with enhanced photodegradation of methylene blue. *Particuology* 69:111-122.
34. Fan Z, Wang D, Yuan Y, Wang Y, Cheng Z, Liu Y, Xie Z (2020) A lightweight and conductive MXene/graphene hybrid foam for superior electromagnetic interference shielding. *Chem Eng J* 381:122696.
35. Khazaei M, Arai M, Sasaki T, Chung C-Y, Venkataramanan NS, Estili M, Sakka Y, Kawazoe Y (2013) Novel Electronic and Magnetic Properties of Two-Dimensional Transition Metal Carbides and Nitrides. *Adv Funct Mater* 23(17):2185-2192.
36. Luo W, Wei Y, Zhuang Z, Lin Z, Li X, Hou C, Li T, Ma Y (2022) Fabrication of $Ti_3C_2T_x$ MXene/polyaniline composite films with adjustable thickness for high-performance flexible all-solid-state symmetric supercapacitors.

- Electrochim Acta 406:139871.
37. Naguib M, Kurtoglu M, Presser V, Lu J, Niu J, Heon M, Hultman L, Gogotsi Y, Barsoum MW (2011) Two-dimensional nanocrystals produced by exfoliation of Ti_3AlC_2 . *Adv Mater* 23(37):4248-4253.
 38. Wang J, Kang H, Ma H, Liu Y, Xie Z, Wang Y, Fan Z (2021) Super-Fast Fabrication of MXene Film through a Combination of Ion Induced Gelation and Vacuum-Assisted Filtration. *Engineered Science* 15:57-66.
 39. Wang Y, Liu Y, Wang C, Liu H, Zhang J, Lin J, Fan J, Ding T, Ryu JE, Guo Z (2020) Significantly Enhanced Ultrathin NiCo-based MOF Nanosheet Electrodes Hybridized with $Ti_3C_2T_x$ MXene for High Performance Asymmetric Supercapacitors. *Engineered Science* 9:50-59.
 40. Wei Y, Luo W, Li X, Lin Z, Hou C, Ma M, Ding J, Li T, Ma Y (2022) PANI-MnO₂ and $Ti_3C_2T_x$ (MXene) as electrodes for high-performance flexible asymmetric supercapacitors. *Electrochim Acta* 406:139874.
 41. Lipatov A, Lu H, Alhabeab M, Anasori B, Gruverman A, Gogotsi Y, Sinitiskii A (2018) Elastic properties of 2D $Ti_3C_2T_x$ MXene monolayers and bilayers. *Sci Adv* 4(6):eaat0491.
 42. Lai S, Jeon J, Jang SK, Xu J, Choi YJ, Park JH, Hwang E, Lee S (2015) Surface group modification and carrier transport properties of layered transition metal carbides (Ti_2CT_x , T: -OH, -F and -O). *Nanoscale* 7(46):19390-19396.
 43. Urbankowski P, Anasori B, Makaryan T, Er D, Kota S, Walsh PL, Zhao M, Shenoy VB, Barsoum MW, Gogotsi Y (2016) Synthesis of two-dimensional titanium nitride Ti_4N_3 (MXene). *Nanoscale* 8(22):11385-11391.
 44. Jin Z, Fang Y, Wang X, Xu G, Liu M, Wei S, Zhou C, Zhang Y, Xu Y (2019) Ultra-efficient electromagnetic wave absorption with ethanol-thermally treated two-dimensional Nb_2CT_x nanosheets. *J Colloid Interface Sci* 537:306-315.
 45. Yang H, Dai J, Liu X, Lin Y, Wang J, Wang L, Wang F *JMC, Physics* (2017) Layered PVB/ $Ba_3Co_2Fe_{24}O_{41}/Ti_3C_2$

- Mxene composite: enhanced electromagnetic wave absorption properties with high impedance match in a wide frequency range. *Mater Chem Phys* 200:179-186.
46. Yan S, Cao C, He J, He L, Qu Z (2019) Investigation on the electromagnetic and broadband microwave absorption properties of Ti_3C_2 MXene/flaky carbonyl iron composites. *J Mater Sci: Mater Electron* 30(7):6537-6543.
47. Guo Y, Wang D, Bai T, Liu H, Zheng Y, Liu C, Shen C (2021) Electrostatic self-assembled $\text{NiFe}_2\text{O}_4/\text{Ti}_3\text{C}_2\text{T}_x$ MXene nanocomposites for efficient electromagnetic wave absorption at ultralow loading level. *Adv Compos Hybrid Mater* 4(3):602-613.
48. Cheng H, Pan Y, Chen Q, Che R, Zheng G, Liu C, Shen C, Liu X (2021) Ultrathin flexible poly(vinylidene fluoride)/MXene/silver nanowire film with outstanding specific EMI shielding and high heat dissipation. *Adv Compos Hybrid Mater* 4(3):505-513.
49. Zhang Y, Liu X, Wu L, Dong W, Xia F, Chen L, Zhou N, Xia L, Hu Z-Y, Liu J, Mohamed HSH, Li Y, Zhao Y, Chen L, Su B-L (2020) A flexible, hierarchically porous PANI/ MnO_2 network with fast channels and an extraordinary chemical process for stable fast-charging lithium-sulfur batteries. *J Mater Chem A* 8(5):2741-2751.
50. Zhuang Z, Wang W, Wei Y, Li T, Ma M, Ma Y (2021) Preparation of polyaniline nanorods/manganese dioxide nanoflowers core/shell nanostructure and investigation of electrochemical performances. *Adv Compos Hybrid Mater* 4(4):938-945.
51. Yan J, Huang Y, Liu X, Zhao X, Li T, Zhao Y, Liu P (2021) Polypyrrole-Based Composite Materials for Electromagnetic Wave Absorption. *Polym Rev* 61:646-687.
52. Guo J, Li X, Chen Z, Zhu J, Mai X, Wei R, Sun K, Liu H, Chen Y, Naik N, Guo Z (2022) Magnetic NiFe_2O_4 /Polypyrrole nanocomposites with enhanced electromagnetic wave absorption. *Journal of Materials*

- Science & Technology 108:64-72.
53. Wang Y, Du Y, Xu P, Qiang R, Han X (2017) Recent Advances in Conjugated Polymer-Based Microwave Absorbing Materials. *Polymers (Basel)* 9(1):29.
54. Wei Y, Luo W, Zhuang Z, Dai B, Ding J, Li T, Ma M, Yin X, Ma Y (2021) Fabrication of ternary MXene/MnO₂/polyaniline nanostructure with good electrochemical performances. *Adv Compos Hybrid Mater* 4(4):1082-1091.
55. Ma Y, Hou C, Zhang H, Zhang Q, Liu H, Wu S, Guo Z (2019) Three-dimensional core-shell Fe₃O₄/Polyaniline coaxial heterogeneous nanonets: Preparation and high performance supercapacitor electrodes. *Electrochim Acta* 315:114-123.
56. Kumar P, Narayan Maiti U, Sikdar A, Kumar Das T, Kumar A, Sudarsan V (2019) Recent Advances in Polymer and Polymer Composites for Electromagnetic Interference Shielding: Review and Future Prospects. *Polym Rev* 59(4):687-738.
57. Kruželák J, Kvasničáková A, Hložeková K, Hudec I (2021) Progress in polymers and polymer composites used as efficient materials for EMI shielding. *Nanoscale Adv* 3(1):123-172.
58. Yu Z, Yan Z, Zhang F, Wang J, Shao Q, Murugadoss V, Alhadhrami A, Mersal GAM, Ibrahim MM, El-Bahy ZM, Li Y, Huang M, Guo Z (2022) Waterborne acrylic resin co-modified by itaconic acid and γ -methacryloxypropyl triisopropoxidesilane for improved mechanical properties, thermal stability, and corrosion resistance. *Prog Org Coat* 168:106875.
59. Liu T, Liu N, An Q, Xiao Z, Zhai S, Li Z (2019) Designed construction of Ti₃C₂T_x@PPY composites with enhanced microwave absorption performance. *J Alloys Compd* 802:445-457.

60. Qu B, Zhu C, Li C, Zhang X, Chen Y (2016) Coupling Hollow Fe₃O₄-Fe Nanoparticles with Graphene Sheets for High-Performance Electromagnetic Wave Absorbing Material. *ACS Appl Mater Interfaces* 8(6):3730-3735.
61. Lv L, Liu J, Liu H, Liu C, Lu Y, Sun K, Fan R, Wang N, Lu N, Guo Z, Wujcik EK (2018) An Overview of Electrically Conductive Polymer Nanocomposites toward Electromagnetic Interference Shielding. *Engineered Science* 2:26-42.
62. Gogotsi Y, Huang Q (2021) MXenes: Two-Dimensional Building Blocks for Future Materials and Devices. *ACS Nano* 15(4):5775-5780.
63. Jia X, Li Y, Shen B, Zheng W (2022) Evaluation, fabrication and dynamic performance regulation of green EMI-shielding materials with low reflectivity: A review. *Composites, Part B* 233:109652.
64. Du B, Zhang D, Qian J, Cai M, He C, Zhou P, Shui A (2021) Multifunctional carbon nanofiber-SiC nanowire aerogel films with superior microwave absorbing performance. *Adv Compos Hybrid Mater* 4(4):1281-1291.
65. Arief I, Bhattacharjee Y, Prakash O, Sahu M, Suwas S, Bose S (2019) Tunable CoNi microstructures in flexible multilayered polymer films can shield electromagnetic radiation. *Composites, Part B* 177:107283.
66. He LJEM, Manufacturing (2021) Improve Thermal Conductivity of Polymer Composites via Conductive Network. *Nat Nanotechnol* 13:1-2.
67. Chen J, Zhu Y, Guo Z, Nasibulin AGJES (2020) Recent Progress on Thermo-electrical Properties of Conductive Polymer Composites and Their Application in Temperature Sensors. *Engineered Science* 12:13-22.
68. Sun J, Zhang X, Du Q, Murugadoss V, Wu D, Guo ZJEM, Manufacturing (2021) The Contribution of Conductive Network Conversion in Thermal Conductivity Enhancement of Polymer Composite: A Theoretical and Experimental Study. *ES Materials & Manufacturing* 13:53-65.

69. Jia H, Xing H, Ji X, Gao S (2021) Self-template and in-situ polymerization strategy to lightweight hollow MnO_2 @polyaniline core-shell heterojunction with excellent microwave absorption properties. *Appl Surf Sci* 537:147857.
70. Shang Q, Feng H, Liu J, Lian Q, Feng Z, Chen N, Qiu J, Wu H (2021) Constructing and optimizing hollow $\text{Zn}_x\text{Fe}_{3-x}\text{O}_4$ @polyaniline composites as high-performance microwave absorbers. *J Colloid Interface Sci* 584:80-91.
71. Sushmita K, Madras G, Bose S (2020) Polymer Nanocomposites Containing Semiconductors as Advanced Materials for EMI Shielding. *ACS Omega* 5(10):4705-4718.
72. Wu J (2021) Multichannel Absorption Enhancement in Graphene Based on Metal-Photonic Crystal Hetero-Structure. *ES Energy & Environment* 13:25-30.
73. Tao Y, Yan B, Fan D, Zhang N, Ma S, Wang L, Wu Y, Wang M, Zhao J, Zhang H (2020) Structural changes of starch subjected to microwave heating: A review from the perspective of dielectric properties. *Trends Food Sci Technol* 99:593-607.
74. Zhang P, Zhang X, Li B, Xu L, Dang F, Li B-W (2021) Enhanced microwave absorption performance in an ultralight porous single-atom Co-N-C absorber. *Adv Compos Hybrid Mater* 4(4):1292-1301.
75. Liu Q, Cao Q, Bi H, Liang C, Yuan K, She W, Yang Y, Che R (2016) $\text{CoNi@SiO}_2\text{@TiO}_2$ and CoNi@Air@TiO_2 Microspheres with Strong Wideband Microwave Absorption. *Adv Mater* 28(3):486-490.
76. Cao M-S, Cai Y-Z, He P, Shu J-C, Cao W-Q, Yuan J (2019) 2D MXenes: Electromagnetic property for microwave absorption and electromagnetic interference shielding. *Chem Eng J* 359:1265-1302.
77. Cheng Y, Zhao H, Yang Z, Lv J, Cao J, Qi X, Ji G, Du Y (2018) An unusual route to grow carbon shell on Fe_3O_4 microspheres with enhanced microwave absorption. *J Alloys Compd* 762:463-472.

78. Yang Q, Shi Y, Fang Y, Dong Y, Ni Q, Zhu Y, Fu Y (2019) Construction of polyaniline aligned on magnetic functionalized biomass carbon giving excellent microwave absorption properties. *Compos Sci Technol* 174:176-183.
79. Wu N, Zhao B, Liu J, Li Y, Chen Y, Chen L, Wang M, Guo Z (2021) MOF-derived porous hollow Ni/C composites with optimized impedance matching as lightweight microwave absorption materials. *Adv Compos Hybrid Mater* 4(3):707-715.
80. Yang M, Wang Z, Ji R, Jin R, Liu J, Song X, Nan Z, Zhang M (2021) Tunable microwave absorbing properties based on facile microwave-induced in-situ formation of interfacial structures. *Appl Surf Sci* 545:149079.
81. Feng W, Luo H, Wang Y, Zeng S, Deng L, Zhou X, Zhang H, Peng S (2018) Ti_3C_2 MXene: a promising microwave absorbing material. *RSC Adv* 8(5):2398-2403.
82. Liang L, Li Q, Yan X, Feng Y, Wang Y, Zhang HB, Zhou X, Liu C, Shen C, Xie X (2021) Multifunctional Magnetic $Ti_3C_2T_x$ MXene/Graphene Aerogel with Superior Electromagnetic Wave Absorption Performance. *ACS Nano* 15(4):6622–6632.
83. Yang X, Fan B, Wang X, Tang X, Wang J, Tong G, Wang X, Tian W (2021) HCl induced structure evolution and dual-frequency broadband microwave absorption of PANI hierarchical microtubes. *J Environ Chem Eng* 9(4):105672.
84. Guo Z, Li A, Sun Z, Yan Z, Liu H, Qian L (2022) Negative permittivity behavior in microwave frequency from cellulose-derived carbon nanofibers. *Adv Compos Hybrid Mater* 5:50-57.
85. Green M, Chen X (2019) Recent progress of nanomaterials for microwave absorption. *J Materiomics* 5(4):503-541.

86. An Y, Feng S, Shao G, Yuan W, Sun K, Li X, Fan RJES (2020) Influence of the Annealing Process on Magnetic Performance of Iron based Soft Magnetic Composites. *Engineered Science* 11:85-91.
87. Zhang Y, Wang X, Cao M (2018) Confinedly implanted NiFe₂O₄-rGO: Cluster tailoring and highly tunable electromagnetic properties for selective-frequency microwave absorption. *Nano Res* 11(3):1426-1436.
88. Wu H, Zhang Y, Yin R, Zhao W, Li X, Qian L (2017) Magnetic negative permittivity with dielectric resonance in random Fe₃O₄@graphene-phenolic resin composites. *Adv Compos Hybrid Mater* 1(1):168-176.
89. Deokate RJEM, Manufacturing (2021) Chemically Deposited NiCo₂O₄ Thin Films for Electrochemical Study. *ES Materials & Manufacturing* 11:16-19.
90. Guo J, Chen Z, Abdul W, Kong J, Khan MA, Young DP, Zhu J, Guo Z (2021) Tunable positive magnetoresistance of magnetic polyaniline nanocomposites. *Adv Compos Hybrid Mater* 4(3):534-542.
91. Guo J, Li X, Liu H, Young DP, Song G, Song K, Zhu J, Kong J, Guo Z (2021) Tunable magnetoresistance of core-shell structured polyaniline nanocomposites with 0-, 1-, and 2-dimensional nanocarbons. *Adv Compos Hybrid Mater* 4(1):51-64.
92. Wang X-X, Ma T, Shu J-C, Cao M-S (2018) Confinedly tailoring Fe₃O₄ clusters-NG to tune electromagnetic parameters and microwave absorption with broadened bandwidth. *Chem Eng J* 332:321-330.
93. Wang H, Meng F, Li J, Li T, Chen Z, Luo H, Zhou Z (2018) Carbonized Design of Hierarchical Porous Carbon/Fe₃O₄@Fe Derived from Loofah Sponge to Achieve Tunable High-Performance Microwave Absorption. *ACS Sustainable Chem Eng* 6(9):11801-11810.
94. Yang H, Zhang X, Xiong Z, Shen Z, Liu C, Xie Y (2021) Cu₂O@nanoporous carbon composites derived from Cu-based MOFs with ultrabroad-bandwidth electromagnetic wave absorbing performance. *Ceram Int* 47(2):2155-2164.

95. Lu X, Zhu D, Li X, Li M, Chen Q, Qing Y (2021) Gelatin-derived N-doped hybrid carbon nanospheres with an adjustable porous structure for enhanced electromagnetic wave absorption. *Adv Compos Hybrid Mater* 4(4):946-956.
96. Guo J, Chen Z, Xu X, Li X, Liu H, Xi S, Abdul W, Wu Q, Zhang P, Xu BB, Zhu J, Guo Z (2022) Enhanced electromagnetic wave absorption of engineered epoxy nanocomposites with the assistance of polyaniline fillers. *Adv Compos Hybrid Mater*. <https://doi.org/10.1007/s42114-022-00417-2>.
97. Pan D, Yang G, Abo-Dief HM, Dong J, Su F, Liu C, Li Y, Bin Xu B, Murugadoss V, Naik N, El-Bahy SM, El-Bahy ZM, Huang M, Guo Z (2022) Vertically Aligned Silicon Carbide Nanowires/Boron Nitride Cellulose Aerogel Networks Enhanced Thermal Conductivity and Electromagnetic Absorbing of Epoxy Composites. *Nanomicro Lett* 14(1):118.
98. Wang W, Deng X, Liu D, Luo F, Cheng H, Cao T, Li Y, Deng Y, Xie W (2022) Broadband radar-absorbing performance of square-hole structure. *Adv Compos Hybrid Mater* 5:525-535.
99. Guo C, Zhang W, Wang R, Qi S (2019) Enhanced electromagnetic wave absorption by optimized impedance matching: covalently bonded polyaniline nanorods over graphene nanoplates. *J Mater Sci: Mater Electron* 30(21):19426-19436.
100. Hu P, Dong S, Yuan F, Li X, Hong C (2022) Hollow carbon microspheres modified with NiCo₂S₄ nanosheets as a high-performance microwave absorber. *Adv Compos Hybrid Mater* 5:469-480.
101. Zhang Z, Zhao Y, Li Z, Zhang L, Liu Z, Long Z, Li Y, Liu Y, Fan R, Sun K, Zhang Z (2021) Synthesis of carbon/SiO₂ core-sheath nanofibers with Co-Fe nanoparticles embedded in via electrospinning for high-performance microwave absorption. *Adv Compos Hybrid Mater* 5(1):513-524.

102. Yang N, Luo ZX, Chen SC, Wu G, Wang YZ (2020) Fe₃O₄ Nanoparticle/N-Doped Carbon Hierarchically Hollow Microspheres for Broadband and High-Performance Microwave Absorption at an Ultralow Filler Loading. ACS Appl Mater Interfaces 12(16):18952-18963.
103. Qiu Y, Lin Y, Yang H, Wang L, Wang M, Wen B (2020) Hollow Ni/C microspheres derived from Ni-metal organic framework for electromagnetic wave absorption. Chem Eng J 383:123207.
104. Li C, Zhang Y, Ji S, Jiang X, Zhang Z, Yu L (2017) Microwave absorption properties of γ -Fe₂O₃/(SiO₂)_x-SO₃H/polypyrrole core/shell/shell microspheres. J Mater Sci 53(7):5270-5286.
105. Yang M, Yuan Y, Li Y, Sun X, Wang S, Liang L, Ning Y, Li J, Yin W, Li Y (2020) Anisotropic Electromagnetic Absorption of Aligned Ti₃C₂T_x MXene/Gelatin Nanocomposite Aerogels. ACS Appl Mater Interfaces 12(29):33128-33138.
106. Deng B, Xiang Z, Xiong J, Liu Z, Yu L, Lu W (2020) Sandwich-Like Fe&TiO₂@C Nanocomposites Derived from MXene/Fe-MOFs Hybrids for Electromagnetic Absorption. Nano-Micro Lett 12(1):55.
107. Cao M, Han C, Wang X, Zhang M, Zhang Y, Shu J, Yang H, Fang X, Yuan J (2018) Graphene nanohybrids: excellent electromagnetic properties for the absorbing and shielding of electromagnetic waves. J Mater Chem C 6(17):4586-4602.
108. Liang X, Quan B, Chen J, Tang D, Zhang B, Ji G (2017) Strong electric wave response derived from the hybrid of lotus roots-like composites with tunable permittivity. Sci Rep 7(1):9462.
109. Lipatov A, Alhabeb M, Lukatskaya MR, Boson A, Gogotsi Y, Sinitskii A (2016) Effect of Synthesis on Quality, Electronic Properties and Environmental Stability of Individual Monolayer Ti₃C₂ MXene Flakes. Adv Electron Mater 2(12):1600255.

110. Gao Q, Pan Y, Zheng G, Liu C, Shen C, Liu X (2021) Flexible multilayered MXene/thermoplastic polyurethane films with excellent electromagnetic interference shielding, thermal conductivity, and management performances. *Adv Compos Hybrid Mater* 4(2):274-285.
111. Li X, Yin X, Liang S, Li M, Cheng L, Zhang L (2019) 2D carbide MXene Ti_2CT_x as a novel high-performance electromagnetic interference shielding material. *Carbon* 146:210-217.
112. Tang Q, Zhou Z, Shen P (2012) Are MXenes promising anode materials for Li ion batteries? Computational studies on electronic properties and Li storage capability of Ti_3C_2 and $Ti_3C_2X_2$ ($X = F, OH$) monolayer. *J Am Chem Soc* 134(40):16909-16916.
113. Yan J, Huang Y, Chen C, Liu X, Liu H (2019) The 3D CoNi alloy particles embedded in N-doped porous carbon foams for high-performance microwave absorbers. *Carbon* 152:545-555.
114. Xu J, Hao Y, Bi K, Zhang R, Huang S, Zhou J (2019) Microwave Orbital Angular Momentum Beam Generation Based on Circularly Polarized Metasurface Antenna Array. *Engineered Science* 6:30-35.
115. Eskandari F, Shabani P, Yousefi R (2020) Simultaneous protonation/deprotonation mechanism in polyaniline-based devices as complementary resistive switches. *Org Electron* 79:105628.
116. Lin T, Yu H, Wang L, Fahad S, Khan A, Naveed K-u-R, Haq F, Nazir A, Amin BU (2021) A review of recent advances in the preparation of polyaniline-based composites and their electromagnetic absorption properties. *J Mater Sci* 56(9):5449-5478.
117. Skabara PJ, Serebryakov IM, Perepichka IFJJotCS, Perkin Transactions 2 (1999) Electron acceptors of the fluorene series. Part 8. 1 Electrochemical and intramolecular charge transfer studies of thiophene functionalised fluorenes. *Journal of the Chemical Society Perkin Transactions (3)*:505-514.

118. Gerard M, Chaubey A, Malhotra BJB, bioelectronics (2002) Application of conducting polymers to biosensors. *Biosens Bioelectron* 17(5):345-359.
119. Salim O, Mahmoud KA, Pant KK, Joshi RK (2019) Introduction to MXenes: synthesis and characteristics. *Mater Today Chem* 14:100191.
120. Wei Y, Zheng M, Luo W, Dai B, Ren J, Ma M, Li T, Ma Y (2022) All pseudocapacitive MXene-MnO₂ flexible asymmetric supercapacitor. *J Energy Storage* 45:103715.
121. Alhabeb M, Maleski K, Anasori B, Lelyukh P, Clark L, Sin S, Gogotsi Y (2017) Guidelines for Synthesis and Processing of Two-Dimensional Titanium Carbide (Ti₃C₂T_x MXene). *Chem Mater* 29(18):7633-7644.
122. Maleski K, Mochalin VN, Gogotsi Y (2017) Dispersions of Two-Dimensional Titanium Carbide MXene in Organic Solvents. *Chem Mater* 29(4):1632-1640.
123. Mashtalir O, Naguib M, Mochalin VN, Dall'Agnese Y, Heon M, Barsoum MW, Gogotsi Y (2013) Intercalation and delamination of layered carbides and carbonitrides. *Nat Commun* 4:1716.
124. Wu Y, Nie P, Wang J, Dou H, Zhang X (2017) Few-Layer MXenes Delaminated via High-Energy Mechanical Milling for Enhanced Sodium-Ion Batteries Performance. *ACS Appl Mater Interfaces* 9(45):39610-39617.
125. Mashtalir O, Lukatskaya MR, Zhao MQ, Barsoum MW, Gogotsi Y (2015) Amine-Assisted Delamination of Nb₂C MXene for Li-Ion Energy Storage Devices. *Adv Mater* 27(23):3501-3506.
126. Naguib M, Mashtalir O, Carle J, Presser V, Lu J, Hultman L, Gogotsi Y, Barsoum MW (2012) Two-Dimensional Transition Metal Carbides. *ACS Nano* 6(2):1322.
127. Ghidui M, Lukatskaya MR, Zhao MQ, Gogotsi Y, Barsoum MW (2014) Conductive two-dimensional titanium carbide 'clay' with high volumetric capacitance. *Nature* 516(7529):78-81.

128. He P, Wang XX, Cai YZ, Shu JC, Zhao QL, Yuan J, Cao MS (2019) Tailoring $Ti_3C_2T_x$ nanosheets to tune local conductive network as an environmentally friendly material for highly efficient electromagnetic interference shielding. *Nanoscale* 11(13):6080-6088.
129. Han M, Yin X, Wu H, Hou Z, Song C, Li X, Zhang L, Cheng L (2016) Ti_3C_2 MXenes with Modified Surface for High-Performance Electromagnetic Absorption and Shielding in the X-Band. *ACS Appl Mater Interfaces* 8(32):21011-21019.
130. Li H, Li X, Liang J, Chen YJAEM (2019) Hydrous RuO_2 - decorated MXene coordinating with silver nanowire inks enabling fully printed micro - supercapacitors with extraordinary volumetric performance. *Adv Energy Mater* 9(15):1803987.
131. Wu X, Han B, Zhang H-B, Xie X, Tu T, Zhang Y, Dai Y, Yang R, Yu Z-Z (2020) Compressible, durable and conductive polydimethylsiloxane-coated MXene foams for high-performance electromagnetic interference shielding. *Chem Eng J* 381:122622.
132. Wu X, Wang Z, Yu M, Xiu L, Qiu J (2017) Stabilizing the MXenes by Carbon Nanoplatelet for Developing Hierarchical Nanohybrids with Efficient Lithium Storage and Hydrogen Evolution Capability. *Adv Mater* 29(24):1607017.
133. Kirkpatrick J, Enion D, Burd DJB (1995) Hydrofluoric acid burns: a review. *Burns* 21(7):483-493.
134. Lukatskaya MR, Bak S-M, Yu X, Yang X-Q, Barsoum MW, Gogotsi Y (2015) Probing the Mechanism of High Capacitance in 2D Titanium Carbide Using In Situ X-Ray Absorption Spectroscopy. *Adv Energy Mater* 5(15):1500589.
135. Li T, Yao L, Liu Q, Gu J, Luo R, Li J, Yan X, Wang W, Liu P, Chen B, Zhang W, Abbas W, Naz R, Zhang D

- (2018) Fluorine-Free Synthesis of High-Purity $Ti_3C_2T_x$ (T=OH, O) via Alkali Treatment. *Angew Chem Int Ed Engl* 57(21):6115-6119.
136. Naguib M, Mochalin VN, Barsoum MW, Gogotsi Y (2014) 25th anniversary article: MXenes: a new family of two-dimensional materials. *Adv Mater* 26(7):992-1005.
137. Sun W, Shah SA, Chen Y, Tan Z, Gao H, Habib T, Radovic M, Green MJ (2017) Electrochemical etching of Ti_2AlC to Ti_2CT_x (MXene) in low-concentration hydrochloric acid solution. *J Mater Chem A* 5(41):21663-21668.
138. Yang S, Zhang P, Wang F, Ricciardulli AG, Lohe MR, Blom PWM, Feng X (2018) Fluoride-Free Synthesis of Two-Dimensional Titanium Carbide (MXene) Using A Binary Aqueous System. *Angew Chem Int Ed Engl* 57(47):15491-15495.
139. Li M, Lu J, Luo K, Li Y, Chang K, Chen K, Zhou J, Rosen J, Hultman L, Eklund P, Persson POA, Du S, Chai Z, Huang Z, Huang Q (2019) Element Replacement Approach by Reaction with Lewis Acidic Molten Salts to Synthesize Nanolaminated MAX Phases and MXenes. *J Am Chem Soc* 141(11):4730-4737.
140. Shirakawa H, Louis EJ, MacDiarmid AG, Chiang CK, Heeger AJ *J Chem Soc, Chemical Communications* (1977) Synthesis of electrically conducting organic polymers: halogen derivatives of polyacetylene, $(CH)_x$. *J Chem Soc, Chem Commun* (16):578-580.
141. Gospodinova N, Terlemezyan L *J Polym Sci Part A: Polym Chem* (1998) Conducting polymers prepared by oxidative polymerization: polyaniline. *Prog Polym Sci* 23(8):1443-1484.
142. Ma Y, Hou C, Zhang H, Qiao M, Chen Y, Zhang H, Zhang Q, Guo Z (2017) Morphology-dependent electrochemical supercapacitors in multi-dimensional polyaniline nanostructures. *J Mater Chem A* 5(27):14041-14052.

143. Ma Y, Zhuang Z, Ma M, Yang Y, Li W, Lin J, Dong M, Wu S, Ding T, Guo Z (2019) Solid polyaniline dendrites consisting of high aspect ratio branches self-assembled using sodium lauryl sulfonate as soft templates: Synthesis and electrochemical performance. *Polymer* 182:121808.
144. Yang Y, Zhang Y, Wei Z (2013) Supramolecular helices: chirality transfer from conjugated molecules to structures. *Adv Mater* 25(42):6039-6049.
145. Wu X, Fu C, Zhang ZM (2020) Chiral Absorbers Based on Polarization Conversion and Excitation of Magnetic Polaritons. *ES Energy & Environment* 8:5-14.
146. Han WJ, Lee JH, Choi HJ (2020) Poly(diphenylamine)/polyaniline core/shell composite nanospheres synthesized using a reactive surfactant and their electrorheology. *Polymer* 188:122161.
147. Zeng F, Qin Z, Liang B, Li T, Liu N, Zhu M (2015) Polyaniline nanostructures tuning with oxidants in interfacial polymerization system. *Prog Nat Sci: Mater Int* 25(5):512-519.
148. Hamlaoui FZ, Naar N (2022) Improvement of the structural and electrical properties of PMMA/PANI-MA blends synthesized by interfacial in situ polymerization in a continuous organic phase. *Polym Bull* 79:37-63.
149. de Barros RA, de Azevedo WM, de Aguiar FM (2003) Photo-induced polymerization of polyaniline. *Mater Charact* 50(2-3):131-134.
150. Kobayashi N, Teshima K, Hirohashi R (1998) Conducting polymer image formation with photoinduced electron transfer reaction. *J Mater Chem* 8(3):497-506.
151. Zhang S, Zhu K, Lv G, Wang G, Yu D, Shao J (2015) UV-Catalytic Preparation of Polypyrrole Nanoparticles Induced by H₂O₂. *The Journal of Physical Chemistry C* 119(32):18707-18718.
152. Guniat L, Caroff P, Fontcuberta IMA (2019) Vapor Phase Growth of Semiconductor Nanowires: Key

- Developments and Open Questions. Chem Rev 119(15):8958-8971.
153. Zhao P, Wang N, Yao M, Ren H, Hu W (2020) Hydrothermal electrodeposition incorporated with CVD-polymerisation to tune PPy@MnO₂ interlinked core-shell nanowires on carbon fabric for flexible solid-state asymmetric supercapacitors. Chem Eng J 380:122488.
154. Wang N, Zhao P, Liang K, Yao M, Yang Y, Hu W (2017) CVD-grown polypyrrole nanofilms on highly mesoporous structure MnO₂ for high performance asymmetric supercapacitors. Chem Eng J 307:105-112.
155. Castro - Carranza A, Nolasco JC, Bley S, Rückmann M, Meierhofer F, Mädler L, Voss T, Gutowski J (2016) Effects of FeCl₃ as oxidizing agent on the conduction mechanisms in polypyrrole (PPy)/pc - ZnO hybrid heterojunctions grown by oxidative chemical vapor deposition. J Polym Sci, Part B: Polym Phys 54(15):1537-1544.
156. Trujillo NJ, Barr MC, Im SG, Gleason KK (2010) Oxidative chemical vapor deposition (oCVD) of patterned and functional grafted conducting polymer nanostructures. J Mater Chem 20(19):3968.
157. Elayappan V, Murugadoss V, Fei Z, Dyson PJ, Angaiah S (2020) Influence of Polypyrrole Incorporated Electrospun Poly(vinylidene fluoride-co-hexafluoropropylene) Nanofibrous Composite Membrane Electrolyte on the Photovoltaic Performance of Dye Sensitized Solar Cell. Engineered Science 10(3):78-84.
158. Elkais AR, Gvozdenović MM, Jugović BZ, Stevanović JS, Nikolić ND, Grgur BN (2011) Electrochemical synthesis and characterization of polyaniline thin film and polyaniline powder. Prog Org Coat 71(1):32-35.
159. Liu X, Wu Z, Yin Y (2017) Hierarchical NiCo₂S₄ @PANI core/shell nanowires grown on carbon fiber with enhanced electrochemical performance for hybrid supercapacitors. Chem Eng J 323:330-339.
160. Wang L, Feng X, Ren L, Piao Q, Zhong J, Wang Y, Li H, Chen Y, Wang B (2015) Flexible Solid-State Supercapacitor Based on a Metal-Organic Framework Interwoven by Electrochemically-Deposited PANI. J Am

- Chem Soc 137(15):4920-4923.
161. Ahmadi SH, Manbohi A (2014) Different morphologies of polypyrrole produced by flow-through and batch electropolymerizations: application in electrochemically controlled in-tube solid phase microextraction. RSC Adv 4(110):64393-64401.
162. Chandler GK, Pletcher D (1986) The electrodeposition of metals onto polypyrrole films from aqueous solution. J Appl Electrochem 16(1):62-68.
163. Debiemme-Chouvy C, Fakhry A, Pillier F (2018) Electrosynthesis of polypyrrole nano/micro structures using an electrogenerated oriented polypyrrole nanowire array as framework. Electrochim Acta 268:66-72.
164. Zhou J, Kang Q, Xu S, Li X, Liu C, Ni L, Chen N, Lu C, Wang X, Peng L, Guo X, Ding W, Hou W (2022) Ultrahigh rate capability of 1D/2D polyaniline/titanium carbide (MXene) nanohybrid for advanced asymmetric supercapacitors. Nano Res 15:285-295.
165. Zhang CJ, Pinilla S, McEvoy N, Cullen CP, Anasori B, Long E, Park S-H, Seral-Ascaso A, Shmeliov A, Krishnan D, Morant C, Liu X, Duesberg GS, Gogotsi Y, Nicolosi V (2017) Oxidation Stability of Colloidal Two-Dimensional Titanium Carbides (MXenes). Chem Mater 29(11):4848-4856.
166. Liu LX, Chen W, Zhang HB, Wang QW, Guan F, Yu ZZ (2019) Flexible and Multifunctional Silk Textiles with Biomimetic Leaf - Like MXene/Silver Nanowire Nanostructures for Electromagnetic Interference Shielding, Humidity Monitoring, and Self - Derived Hydrophobicity. Adv Funct Mater 29(44):1905197.
167. Yin G, Wang Y, Wang W, Yu D (2020) Multilayer structured PANI/MXene/CF fabric for electromagnetic interference shielding constructed by layer-by-layer strategy. Colloids Surf, A 601:125047.
168. Yin G, Wang Y, Wang W, Qu Z, Yu D (2021) A Flexible Electromagnetic Interference Shielding Fabric Prepared

- by Construction of PANI/MXene Conductive Network via Layer - by - Layer Assembly. *Adv Mater Interfaces* 8(6):2001893.
169. Xu H, Zheng D, Liu F, Li W, Lin J (2020) Synthesis of an MXene/polyaniline composite with excellent electrochemical properties. *J Mater Chem A* 8(12):5853-5858.
170. Wu W, Wang C, Zhao C, Wei D, Zhu J, Xu Y (2020) Facile strategy of hollow polyaniline nanotubes supported on Ti_3C_2 -MXene nanosheets for High-performance symmetric supercapacitors. *J Colloid Interface Sci* 580:601-613.
171. Boota M, Paranthaman MP, Naskar AK, Gogotsi Y, Li Y, Akato KJC (2015) Waste tire derived carbon-polymer composite paper as pseudocapacitive electrode with long cycle life. *ChemSusChem* 8(21):3576-3581.
172. Boota M, Anasori B, Voigt C, Zhao MQ, Barsoum MW, Gogotsi Y (2016) Pseudocapacitive Electrodes Produced by Oxidant-Free Polymerization of Pyrrole between the Layers of 2D Titanium Carbide (MXene). *Adv Mater* 28(7):1517-1522.
173. Hawkins SJ, Ratcliffe NM (2000) A study of the effects of acid on the polymerisation of pyrrole, on the oxidative polymerisation of pyrrole and on polypyrrole. *J Mater Chem* 10(9):2057-2062.
174. Chen C, Boota M, Xie X, Zhao M, Anasori B, Ren CE, Miao L, Jiang J, Gogotsi Y (2017) Charge transfer induced polymerization of EDOT confined between 2D titanium carbide layers. *J Mater Chem A* 5(11):5260-5265.
175. Wu W, Niu D, Zhu J, Gao Y, Wei D, Liu X, Wang F, Wang L, Yang L (2019) Organ-like Ti_3C_2 Mxenes/polyaniline composites by chemical grafting as high-performance supercapacitors. *J Electroanal Chem* 847:113203.
176. Zhu M, Huang Y, Deng Q, Zhou J, Pei Z, Xue Q, Huang Y, Wang Z, Li H, Huang Q, Zhi C (2016) Highly Flexible, Freestanding Supercapacitor Electrode with Enhanced Performance Obtained by Hybridizing Polypyrrole Chains

- with MXene. *Adv Energy Mater* 6(21):1600969.
177. Jian X, He M, Chen L, Zhang M-m, Li R, Gao L-j, Fu F, Liang Z-h (2019) Three-dimensional carambola-like MXene/polypyrrole composite produced by one-step co-electrodeposition method for electrochemical energy storage. *Electrochim Acta* 318:820-827.
178. Qing Y, Zhou W, Luo F, Zhu D (2016) Titanium carbide (MXene) nanosheets as promising microwave absorbers. *Ceram Int* 42(14):16412-16416.
179. He P, Cao M-S, Cai Y-Z, Shu J-C, Cao W-Q, Yuan J (2020) Self-assembling flexible 2D carbide MXene film with tunable integrated electron migration and group relaxation toward energy storage and green EMI shielding. *Carbon* 157:80-89.
180. Liu P, Yao Z, Ng VMH, Zhou J, Kong LB, Yue K (2018) Facile synthesis of ultrasmall Fe₃O₄ nanoparticles on MXenes for high microwave absorption performance. *Composites, Part A* 115:371-382.
181. Liang L, Yang R, Han G, Feng Y, Zhao B, Zhang R, Wang Y, Liu C (2020) Enhanced Electromagnetic Wave-Absorbing Performance of Magnetic Nanoparticles-Anchored 2D Ti₃C₂T_x MXene. *ACS Appl Mater Interfaces* 12(2):2644-2654.
182. Li X, You W, Wang L, Liu J, Wu Z, Pei K, Li Y, Che R (2019) Self-Assembly-Magnetized MXene Avoid Dual-Agglomeration with Enhanced Interfaces for Strong Microwave Absorption through a Tunable Electromagnetic Property. *ACS Appl Mater Interfaces* 11(47):44536-44544.
183. Zhao Y, Liu L, Han J, Wu W, Tong G (2017) Effective modulation of electromagnetic characteristics by composition and size in expanded graphite/Fe₃O₄ nanoring composites with high Snoek's limit. *J Alloys Compd* 728:100-111.

184. Pan F, Yu L, Xiang Z, Liu Z, Deng B, Cui E, Shi Z, Li X, Lu W (2021) Improved synergistic effect for achieving ultrathin microwave absorber of 1D Co nanochains/2D carbide MXene nanocomposite. *Carbon* 172:506-515.
185. Peng Z, Jiang Q, Peng P, Li F-F (2020) NH₃-activated Fullerene Derivative Hierarchical Microstructures to Porous Fe₃O₄/N-C for Oxygen Reduction Reaction and Zn-air Battery. *Engineered Science* 14(2):27-38.
186. Qi G, Liu Y, Chen L, Xie P, Pan D, Shi Z, Quan B, Zhong Y, Liu C, Fan R, Guo Z (2021) Lightweight Fe₃C@Fe/C nanocomposites derived from wasted cornstalks with high-efficiency microwave absorption and ultrathin thickness. *Adv Compos Hybrid Mater* 4(4):1226-1238.
187. Wang C, Wu X, Wang F, Zhang X (2021) Optimization Design of a Multilayer Structure for Broadband and Direction-Selective Emissivity. *ES Energy & Environment* 11:84-92.
188. Qiu Y, Xu M, Li Q, Huang R, Wang J (2021) A high-Temperature Near-Perfect Solar Selective Absorber Combining Tungsten Nanohole and Nanoshuriken Arrays. *ES Energy & Environment* 13:77-90.
189. Oyharçabal M, Olinga T, Foulc M-P, Lacomme S, Gontier E, Vigneras V (2013) Influence of the morphology of polyaniline on the microwave absorption properties of epoxy polyaniline composites. *Compos Sci Technol* 74:107-112.
190. Haba Y, Segal E, Narkis M, Titelman G, Siegmann AJSm (1999) Polymerization of aniline in the presence of DBSA in an aqueous dispersion. *Synth Met* 106(1):59-66.
191. Huang J, Kaner RB (2004) Nanofiber Formation in the Chemical Polymerization of Aniline: A Mechanistic Study. *Angew Chem* 116(43):5941-5945.
192. Oyharçabal M, Olinga T, Foulc M-P, Vigneras VJSM (2012) Polyaniline/clay as nanostructured conductive filler for electrically conductive epoxy composites. Influence of filler morphology, chemical nature of reagents, and

- curing conditions on composite conductivity. *Synth Met* 162(7-8):555-562.
193. Yu L, Yu L, Dong Y, Zhu Y, Fu Y, Ni Q (2019) Compressible polypyrrole aerogel as a lightweight and wideband electromagnetic microwave absorber. *J Mater Sci: Mater Electron* 30(6):5598-5608.
194. Tian C, Du Y, Xu P, Qiang R, Wang Y, Ding D, Xue J, Ma J, Zhao H, Han X (2015) Constructing Uniform Core-Shell PPy@PANI Composites with Tunable Shell Thickness toward Enhancement in Microwave Absorption. *ACS Appl Mater Interfaces* 7(36):20090-20099.
195. Yang H, Han N, Lin Y, Zhang G, Wang L (2016) Enhanced microwave absorbing properties of PANI/CoFe₂O₄/PVDF composite. *RSC Adv* 6(102):100585-100589.
196. Li Y, Wang J, Li H, Zhang B, Cui Y, Cai J, Wang Y, Zhang Y, Bao Z, Zhang Y, Wu Y (2020) Effect of conductive PANI vs. insulative PS shell coated Ni nanochains on electromagnetic wave absorption. *J Alloys Compd* 821:153531.
197. Wei H, Dong J, Fang X, Zheng W, Sun Y, Qian Y, Jiang Z, Huang Y (2019) Ti₃C₂T_x MXene/polyaniline (PANI) sandwich intercalation structure composites constructed for microwave absorption. *Compos Sci Technol* 169:52-59.
198. Tong Y, He M, Zhou Y, Zhong X, Fan L, Huang T, Liao Q, Wang Y (2018) Hybridizing polypyrrole chains with laminated and two-dimensional Ti₃C₂T_x toward high-performance electromagnetic wave absorption. *Appl Surf Sci* 434:283-293.
199. Gao X, Wang B, Wang K, Xu S, Liu S, Liu X, Jia Z, Wu G (2021) Design of Ti₃C₂T_x/TiO₂/PANI multi-layer composites for excellent electromagnetic wave absorption performance. *J Colloid Interface Sci* 583:510-521.
200. Wang Y, Gao X, Zhang L, Wu X, Wang Q, Luo C, Wu G (2019) Synthesis of Ti₃C₂/Fe₃O₄/PANI hierarchical

- architecture composite as an efficient wide-band electromagnetic absorber. *Appl Surf Sci* 480:830-838.
201. Jin L, Wang J, Wu F, Yin Y, Zhang B (2021) MXene@Fe₃O₄ microspheres/fibers composite microwave absorbing materials: Optimum composition and performance evaluation. *Carbon* 182:770-780.
202. Hou T, Wang B, Ma M, Feng A, Huang Z, Zhang Y, Jia Z, Tan G, Cao H, Wu G (2020) Preparation of two-dimensional titanium carbide (Ti₃C₂T_x) and NiCo₂O₄ composites to achieve excellent microwave absorption properties. *Composites, Part B* 180:107577.
203. He J, Liu S, Deng L, Shan D, Cao C, Luo H, Yan S (2020) Tunable electromagnetic and enhanced microwave absorption properties in CoFe₂O₄ decorated Ti₃C₂ MXene composites. *Appl Surf Sci* 504:144210.
204. Qian Y, Wei H, Dong J, Du Y, Fang X, Zheng W, Sun Y, Jiang Z (2017) Fabrication of urchin-like ZnO-MXene nanocomposites for high-performance electromagnetic absorption. *Ceramics International* 43(14):10757-10762.
205. Li X, Yin X, Han M, Song C, Xu H, Hou Z, Zhang L, Cheng L (2017) Ti₃C₂MXenes modified with in situ grown carbon nanotubes for enhanced electromagnetic wave absorption properties. *J Mater Chem C* 5(16):4068-4074.
206. Peng Y, Deng L, Luo H, Huang S (2020) Tailoring microwave electromagnetic responses in Ti₃C₂T_x MXene with CoNi-alloy nanoparticles decoration via mild hydrothermal method. *Results Phys* 19:103516.
207. Cui Y, Yang K, Wang J, Shah T, Zhang Q, Zhang B (2021) Preparation of pleated RGO/MXene/Fe₃O₄ microsphere and its absorption properties for electromagnetic wave. *Carbon* 172:1-14.
208. Zhang X, Wang H, Hu R, Huang C, Zhong W, Pan L, Feng Y, Qiu T, Zhang C, Yang J (2019) Novel solvothermal preparation and enhanced microwave absorption properties of Ti₃C₂T_x MXene modified by in situ coated Fe₃O₄ nanoparticles. *Appl Surf Sci* 484:383-391.
209. Wang Y, Yang J, Chen Z, Hu Y (2019) A new flexible and ultralight carbon foam/Ti₃C₂T_x MXene hybrid for high-

- performance electromagnetic wave absorption. *RSC Adv* 9(70):41038-41049.
210. Ding J, Chen F, Chen J, Liang J, Kong J (2020) MXene - derived TiC/SiBCN ceramics with excellent electromagnetic absorption and high - temperature resistance. *J Am Ceram Soc* 104(4):1772-1784.
211. Cui C, Guo R, Ren E, Xiao H, Zhou M, Lai X, Qin Q, Jiang S, Qin W (2021) MXene-based rGO/Nb₂CT_x/Fe₃O₄ composite for high absorption of electromagnetic wave. *Chem Eng J* 405:126626.
212. Zhou C, Wang X, Luo H, Deng L, Wang S, Wei S, Zheng Y, Jia Q, Liu J (2019) Interfacial design of sandwich-like CoFe@Ti₃C₂T_x composites as high efficient microwave absorption materials. *Appl Surf Sci* 494:540-550.
213. Yu L, Yu L, Dong Y, Zhu Y, Fu Y, Ni Q (2019) Compressible polypyrrole aerogel as a lightweight and wideband electromagnetic microwave absorber. *Journal of Materials Science: Materials in Electronics* 301(6):5598-5608.
214. Zhan Y, Zhao R, Xiang X, He S, Zhao S, Xue W (2019) Hierarchical core/shell bamboo-like polypyrrole nanofibers/Fe₃O₄ hybrids with superior microwave absorption performance. *Compos Interfaces* 26(12):1087-1100.
215. Zhang M, Ling H, Ding S, Xie Y, Cheng T, Zhao L, Wang T, Bian H, Lin H, Li Z, Meng A (2021) Synthesis of CF@PANI hybrid nanocomposites decorated with Fe₃O₄ nanoparticles towards excellent lightweight microwave absorber. *Carbon* 174:248-259.
216. Wen M, Zhao Y, Li Z, Lai S, Zeng Q, Liu C, Liu Y (2021) Preparation of lignin-based carbon/polyaniline composites for advanced microwave absorber. *Diamond Relat Mater* 111:108219.
217. Hou T, Jia Z, Feng A, Zhou Z, Liu X, Lv H, Wu G (2021) Hierarchical composite of biomass derived magnetic carbon framework and phytic acid doped polyaniline with prominent electromagnetic wave absorption capacity. *Journal of Materials Science & Technology* 68:61-69.
218. Ding J, Cheng L (2021) Core-shell Fe₃O₄@SiO₂@PANI composite: Preparation, characterization, and

- applications in microwave absorption. *J Alloys Compd* 881:160574.
219. Di X, Wang Y, Lu Z, Cheng R, Wu X (2021) Design of biomass-derived magnetic carbon/polyaniline with hierarchical network for superior microwave absorption. *J Mater Sci: Mater Electron* 32(14):18790-18807.
220. Zhao X, Huang Y, Yan J, Liu X, Ding L, Zong M, Liu P, Li T (2021) Excellent electromagnetic wave absorption properties of the ternary composite ZnFe₂O₄@PANI-rGO optimized by introducing covalent bonds. *Compos Sci Technol* 210:108801.
221. Zhang Z, Wang G, Gu W, Zhao Y, Tang S, Ji G (2022) A breathable and flexible fiber cloth based on cellulose/polyaniline cellular membrane for microwave shielding and absorbing applications. *J Colloid Interface Sci* 605:193-203.
222. Liu T, Liu N, Zhai S, Gao S, Xiao Z, An Q, Yang D (2019) Tailor-made core/shell/shell-like Fe₃O₄@SiO₂@PPy composites with prominent microwave absorption performance. *J Alloys Compd* 779:831-843.
223. Li J, Ji H, Xu Y, Zhang J, Yan Y (2020) Three-dimensional graphene supported Fe₃O₄ coated by polypyrrole toward enhanced stability and microwave absorbing properties. *J Mater Res Technol* 9(1):762-772.
224. Li S, Huang Y, Zhang N, Zong M, Liu P (2019) Synthesis of polypyrrole decorated FeCo@SiO₂ as a high-performance electromagnetic absorption material. *J Alloys Compd* 774:532-539.
225. Wang Y, Zhang W, Wu X, Luo C, Wang Q, Li J, Hu L (2017) Conducting polymer coated metal-organic framework nanoparticles: Facile synthesis and enhanced electromagnetic absorption properties. *Synth Met* 228:18-24.
226. Lei Y, Yao Z, Li S, Zhou J, Haidry AA, Liu P (2020) Broadband high-performance electromagnetic wave absorption of Co-doped NiZn ferrite/polyaniline on MXenes. *Ceram Int* 46(8):10006-10015.

227. Sang G, Xu P, Yan T, Murugadoss V, Naik N, Ding Y, Guo Z (2021) Interface Engineered Microcellular Magnetic Conductive Polyurethane Nanocomposite Foams for Electromagnetic Interference Shielding. *Nanomicro Lett* 13(1):153.
228. Wang Y, Wang P, Du Z, Liu C, Shen C, Wang Y (2022) Electromagnetic interference shielding enhancement of poly(lactic acid)-based carbonaceous nanocomposites by poly(ethylene oxide)-assisted segregated structure: a comparative study of carbon nanotubes and graphene nanoplatelets. *Adv Compos Hybrid Mater* 5:209-219.